



**UiT** The Arctic University of Norway

Faculty of Science and Technology  
Department of Geosciences

# **Gas migration and sealing modelling in the Haapet Dome area, Norwegian Barents Sea – analysis of seismic anomalies and water column data**

**John-Einar Karlsen Moen**

*Master thesis in petroleum geology, GEO-3900  
May 2020*





NORWEGIAN PETROLEUM  
DIRECTORATE



In cooperation with the Norwegian Petroleum Directorate

*John-Einar Karlsen Moen*

## Abstract

Seismic interpretation, water column data, and well information have enabled a thorough review of shallow amplitude anomalies and subsurface faulting, in conjunction with possible migration pathways in the Haapet Dome area. The processed water column data from the MAREANO-program was presented and evaluated in accordance with potential gas leakage from the seafloor. Water column imaging illustrates that hydroacoustic signatures, which are representative of gas bubble leakage, are probably of non-existence in the Haapet Dome area. A correlation with subsurface stratigraphy illustrates that the possible gas accumulations are situated in the Stø and Nordmela formations, and the Early Cretaceous unit. Given that no apparent evidence of gas leakage is occurring suggests that a sealing lithology is constraining the assumed gas accumulations.

Several models were introduced to discuss and evaluate the possible gas accumulations according to entrapment capability and the possibility of minor gas release. The analysed water column data did not indicate observable gas leakage, where acoustic distortion made detection of potential gas bubbles difficult. The Upper Regional Unconformity (URU) with overlying glacial sediments was assumed to act as a potential trapping mechanism for underlying zones of potential shallow gas accumulations. A gas hydrate stability model was established, which showed that gas hydrates could develop in the study area, dependent on the gas composition. Consequently, local zones of potential gas hydrates could act as hydrocarbon barriers. A possible Permian source rock was suggested to have generated and expelled gas, which is probably represented by its present-day shallow accumulations.

The models presented suggest that no source rocks are generating and expelling hydrocarbons at present-day in the study area. The assumed shallow gas accumulations are thereby represented by a possible older working petroleum system. A shut-down petroleum system, with no or very little influx of hydrocarbons to the study area, combined with shallow sealing lithologies, might be one reason for lack of observed gas seepage in the water column.

# Acknowledgements

Da var plutselig to fantastiske år som masterstudent over. Det har vært en svært innholdsrik opplevelse, men også en krevende prosess.

Først og fremst vil jeg takke Oljedirektoratet for den flotte muligheten til å tolke en særdeles spennende og innovativ oppgave i et relativt lite utforsket område.

Tusen takk til min hovedveileder, Underdirektør for leting Stig-Morten Knutsen, og bi-veiledere, Geolog Rune Mattingsdal og Postdoktor Pavel Serov for oppfølging, godt engasjement og støttende ord. Jeg setter stor pris på bidragene deres! Videre vil jeg takke for oppholdet på Oljedirektoratet, og de lærerike diskusjonene og innspillene fra alle som jobber på kontoret i Harstad. Takk for støtten!

Ønsker å takke alle mine medstudenter gjennom disse årene. En spesiell takk går til Joakim, Ådne, Jørgen, Vebjørn, Kristian, Sigurd, Ørjan og Steinar. Studietiden hadde ikke vært den samme uten dere!

Til slutt fortjener den flotte familien min en stor takk for motiverende ord gjennom hele studieprosessen!

John-Einar Karlsen Moen

Tromsø, Mai 2020



# Table of Contents

1	Introduction .....	1
1.1	Aim and objective.....	1
1.2	Study area: Haapet Dome .....	2
1.3	Petroleum exploration within the Haapet Dome area.....	3
2	Geological background and structural setting of the Barents Sea.....	4
2.1	Eastern province .....	4
2.2	Western province .....	5
2.3	Geological setting of the Haapet Dome area .....	8
2.3.1	Carboniferous to Permian.....	8
2.3.2	Triassic .....	8
2.3.3	Jurassic and Cretaceous period .....	9
2.3.4	Cenozoic Era .....	9
3	Theoretical framework .....	12
3.1	Seismic reflection theory .....	12
3.1.1	Seismic resolution .....	13
3.2	Fault configuration .....	17
3.2.1	Dip-Slip faults .....	17
3.3	The petroleum system.....	18
3.3.1	Source rock.....	20
3.3.2	Reservoir rock and fluid migration .....	21
3.3.3	Traps.....	23
3.4	Direct hydrocarbon indicators .....	27
3.4.1	Seismic response of amplitude anomalies.....	27
3.5	Gas hydrates .....	29
3.6	Water column imaging .....	30
3.7	Pockmarks .....	33
4	Data and methodology .....	33
4.1	Datasets.....	33
4.2	Well data.....	35
4.3	Phase and polarity.....	35
4.4	Seismic resolution.....	36
4.5	Methodology.....	39
4.5.1	Software's.....	39
4.5.2	Seismic attributes .....	39

4.5.3	Gas hydrate stability modelling.....	40
4.5.4	WCD acquisition.....	42
4.5.5	Concepts of WCI.....	42
5	Results.....	44
5.1	Stratigraphic overview.....	44
5.2	Interpreted horizons and isochore maps.....	47
5.3	Faults.....	51
5.4	Shallow amplitude anomalies and leakage zones.....	58
5.4.1	Area 1.....	63
5.4.2	Area 2.....	65
5.4.3	Area 3.....	67
5.4.4	Area 4.....	69
5.5	Potential gas flares and shallow amplitude anomalies.....	71
5.5.1	Location 1.....	71
5.5.2	Location 2.....	75
6	Discussion.....	80
6.1	Subsurface drainage systems.....	80
6.1.1	Migration modelling.....	81
6.1.2	Potential gas seepage.....	84
6.2	Glacigenic sediments acting as seal.....	87
6.3	Stable gas hydrates acting as seal.....	88
6.4	Geological model.....	91
7	Conclusion.....	99
8	Future work.....	100
9	References.....	101
10	Appendices.....	110
10.1	Appendix 1 – Equations.....	110
10.2	Appendix 2 – Processed water column data.....	111
10.3	Appendix 3 – WCI above shallow amplitude anomalies.....	112

# 1 Introduction

## 1.1 Aim and objective

The study area comprises the Haapet Dome, which is located in the most eastern parts of the Bjarmeland Platform. The area encloses the larger region of the southeastern parts of the Norwegian Barents Sea, termed the Barents Sea South East (BSSE). The BSSE is considered an area of constrained geological understanding, compared to its counterpart, the southwestern Barents Sea (Hassaan et al., 2019).

For an extended period of nearly 40 years, insufficient geological knowledge of the disputed area between Norway and Russia had been the case, until the year 2010. An agreement for the borders separating the greater Barents Sea were settled, where detailed seismic acquisition could finally commence. During the following years after signing the treaty in 2011, NPD (Norwegian Petroleum Directorate) acquired about 18 000 of 2D seismic data across the BSSE, where the region was opened for petroleum activity in 2013. Submission of several new structural elements, including the Haapet Dome geological structure, took place during January 2015 (Mattingsdal et al., 2015).

The main aim and objective of this study are to localise and map out shallow seismic anomalies within the stratigraphy of the Late Triassic to the Top Quaternary surface. The shallow seismic anomalies will be evaluated in conjunction with subsurface structures and faulting, and with potential gas flares from the seafloor. Subsequently, the results will be used and compared to a suggested migration model for the study area.

## 1.2 Study area: Haapet Dome

The study area encompasses the northeastern parts of the Barents Sea South East (BSSE), within the Bjarmeland Platform. The survey area is situated between 74°15'N to 73°50'N and 35°10'E to 36°30'E (figure 1.1) and covers approximately an area of 5593 km<sup>2</sup> (NPD, 2019c). The region emphasises a complex and variable geological setting with various episodes of extensional rifting, subsidence, uplift and compressional regimes (Hassaan et al., 2019) throughout its development.

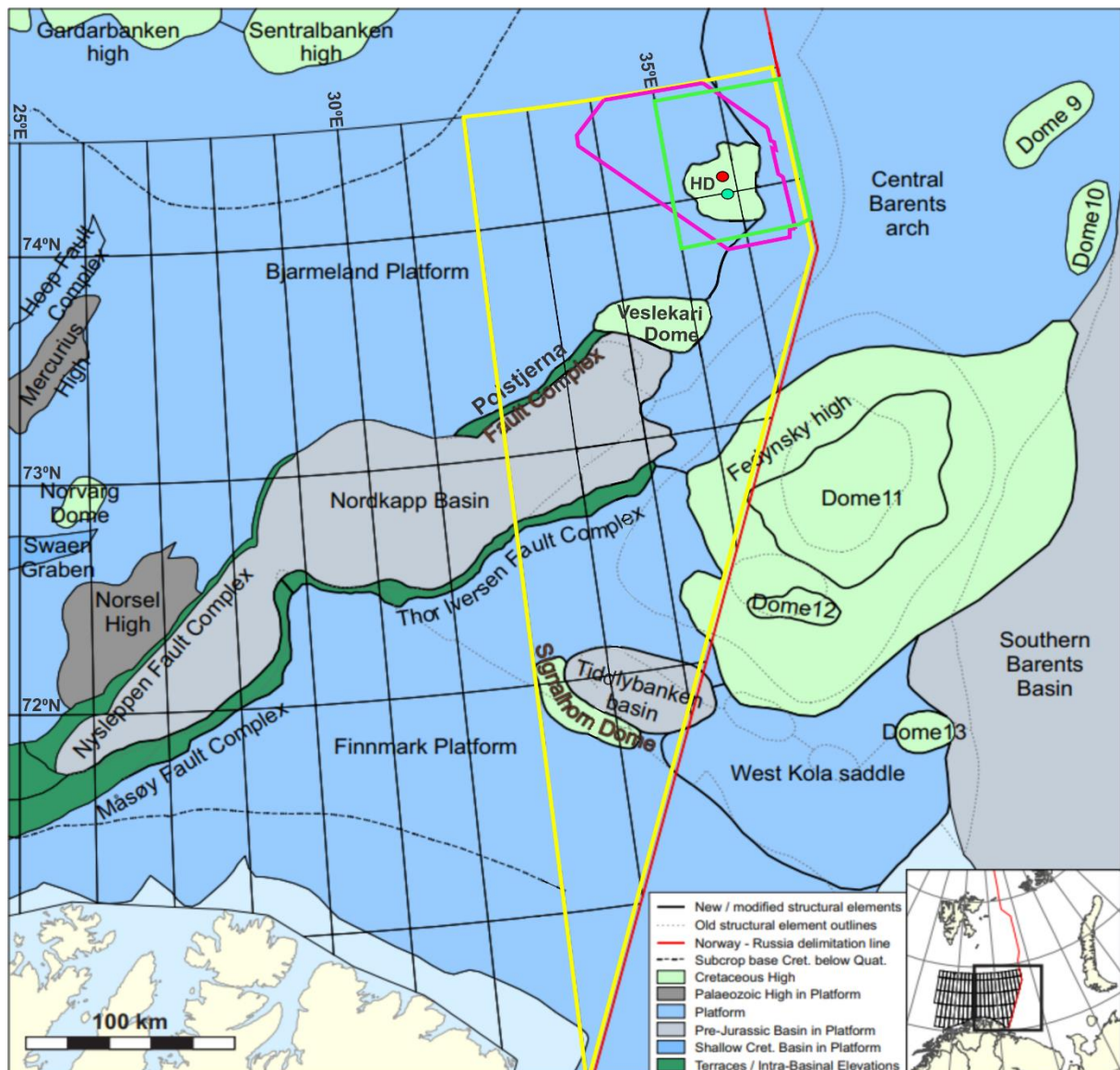


Figure 1.1: Structural framework of the southern Barents Sea. The study area encompasses the Haapet Dome area, situated north of the Veslekari Dome within the pink polygon. The green rectangle represents the gathered water column datasets, whereas the yellow line represents the area of BSSE. Notice that the red and green circles indicate the position of well 7435/12-1 and 7335/3-1, respectively. HD = Haapet Dome. From NPD (2017c), modified after Mattingsdal et al. (2015).

### 1.3 Petroleum exploration within the Haapet Dome area

The Barents Sea is the largest sea area on the Norwegian Continental Shelf, which covers about 313 000 km<sup>2</sup> (NP, 2019). The region is estimated to contain about 2530 million Sm<sup>3</sup> oil equivalents of undiscovered resources across the Barents Sea south, northeast and southeast (NPD, 2019b).

The geological knowledge regarding the study area is moderately good, despite lying within a region of confined geological understanding. Two exploration wells have been drilled within the study area: well 7435/12-1 and 7335/3-1. Well 7435/12-1 proved 6 – 12 billion Sm<sup>3</sup> of recoverable gas (NPD, 2017d).

Well 7435/12-1 was a minor discovery that proved gas in a shallow reservoir of Early Jurassic age (Stø and Nordmela formations) within the Haapet Dome (NPD, 2017a). The sandstone is estimated to be of 28 metres with good to very good reservoir quality. Secondary targets were to prove petroleum in the Snadd- and the Kobbe formations. The Snadd Formation was dry but encountered moderately good reservoir rock, whereas the Kobbe Formation contained poor reservoir quality with small amounts of gas (NPD, 2017a).

Well 7335/3-1 (Korpfjell-deep) was drilled 8 km southeast of well 7435/12-1. The main target was to prove petroleum in Early Triassic reservoir rocks (Havert and Klappmyss formations), where intervals with tight sandstones were located. The second target was to prove petroleum in the Middle to Late Triassic unit (Snadd and Kobbe formations). Additional tight sandstones were encountered, including a thin layer of sandstones, which indicated dry gas. Overall, the well was defined as dry (NPD, 2019a).

## **2 Geological background and structural setting of the Barents Sea**

The greater Barents Sea (figure 2.1) extends from the Norwegian-Greenland Sea in the west to the Novaya Zemlya main islands in the east, and from the mainland of Norway and Russia to the Franz Josef Land and Svalbard in the north. (Larsen et al., 2002). It is globally defined as one of the most extensive epi-continental shelves with a water column that rarely exceeds 500 m. A large monoclinical structure separates the greater Barents Sea into two distinct geological provinces: the Eastern and Western provinces (figure 2.1) (Smelror et al., 2009).

### **2.1 Eastern province**

The Eastern province includes an area of complex tectonic regimes related to the origin of Novaya Zemlya, the history of the Timan-Pechora Basin and the Uralian Orogeny. (Smelror et al., 2009). The Timanian tectonic event probably took place throughout the late Precambrian and ended in the early Palaeozoic (Gee & Pease, 2004).

In the course of early to middle Palaeozoic period, the Eastern Barents Sea was characterised as a passive continental margin with a conversion to a more active continental margin at the end of Late Devonian time. This gave rise to episodes of rifting and evolution of shallow carbonate platforms (Smelror et al., 2009).

Late Carboniferous to Late Triassic represented a time of significant change in tectonic setting, where in the beginning, the closure of the Uralian Ocean was roughly at its end. This led to a collision between Laurasia and the Western Siberia, which took place in the Early Carboniferous to Late Permian and initiated the origin of the Uralian Mountains. The concluding phase of the Uralian orogenesis and the closure of Novaya Zemlya marginal basin correlates to the end of the Early Triassic, where large amounts of sediments accumulated within the East Barents Sea Basin (Smelror et al., 2009).

Continuous uplift and compression would then be the major change during the Late Triassic, which led to the development of the Uralian Mountains. This was the controlling factor for the additional increase in rates of sedimentation across the Eastern Barents Sea and the Timan-Pechora areas. The early and middle stages of Jurassic are represented by continental and marine deposits, which are distributed across the Eastern Barents Basin. The Mesozoic period is considered a quiet period with relatively low tectonic activity and predominantly deposition of terrigenous and marine sediments. While the Eastern provinces were developed through a complex Palaeozoic tectonic history, with a later more stable tectonic condition, the Western provinces went through major compressional tectonic regimes that ended around 400 Ma, with several post-Caledonian rifting phases (Smelror et al., 2009).

## **2.2 Western province**

About 490 million years ago (Late Cambrian time), the two continents, Baltica and Avalonia, started moving towards Laurentia during the closure and subduction of the Iapetus Ocean. The tectonic movements through the Cambrian to Devonian time would result in the formation of the Caledonian Orogeny (McKerrow et al., 2000; Stone, 2012).

In Norway, the Caledonites evolved predominantly through a more complex two-stage tectonic regime, which involved the Finnmarkian stage (Late Cambrian to Early Ordovician) and the Scandian stage (Middle Silurian to Early Devonian) (Smelror et al., 2009).

After the development of the Caledonian Orogeny, significant uplift occurred, which led to large deposits of sand rich sediments through extensional erosion of the Caledonites. During Late Devonian, a change in the tectonic movement occurred. What initially was a subduction movement was converted into lateral movements between Fennoscandia and Greenland (Faleide et al., 2010).

Three rift stages have been dominant during the Post-Caledonian period: Late Devonian (?) to Carboniferous, Middle Jurassic to Early Cretaceous and Early Tertiary. The late Palaeozoic period characterises crustal extension across most of the Barents Sea. The extensional rifting enabled the evolution of various interconnected extensional basins, separated by fault structures and highs (Faleide et al., 2010). In consequence of later tectonics between Late Permian and Middle Triassic, triggering of salt movements within the Nordkapp basin were initiated, which would remain active during later stages of Triassic time (Smelror et al., 2009).

Epeirogenic movements would then generate elevation differences across most of the western provinces. Additional uplift and erosion would subsequently cause major tilting of highs across a north-south structural trend. The regional basins located in the eastern parts of the western provinces has roughly been stable after the late Palaeozoic period, which includes the Haapet Dome area (Faleide et al., 2010).

Middle Jurassic to Early Cretaceous represented the Atlantic rifting phase, where the plate divergence between Norway and Greenland occurred (Henriksen et al., 2011a). The crustal extension was one of the leading factors for the evolution of deep basins during this period, which includes the development of the Harstad, Tromsø, Bjørnøya and Sørvestnaget basins (Smelror et al., 2009). Each basin experienced major differences regarding rapid subsidence and break-up of fault segments, which resulted in structural highs and sub-basins (Faleide et al., 2010).

The transition from early Paleogene to middle Paleogene considers an essential episode where the continental break-up of the North Atlantic margins took place (Smelror et al., 2009). The opening of the Greenland Sea involved a complex splitting of microcontinents, which resulted in a complicated spreading phase. The break-up, related to the spreading phase of the Greenland Sea, initiated another extensional process west of Svalbard (Faleide et al., 2010).

The separation between the Barents Sea shelf and Greenland/North American shelf, continued through Oligocene and Miocene. The late Cenozoic is characterised by additional subsidence and burial of thick sedimentary packages in the west, caused by uplift and erosion of large parts of the Barents Sea shelf. (Faleide et al., 2010; Lasabuda, 2018).



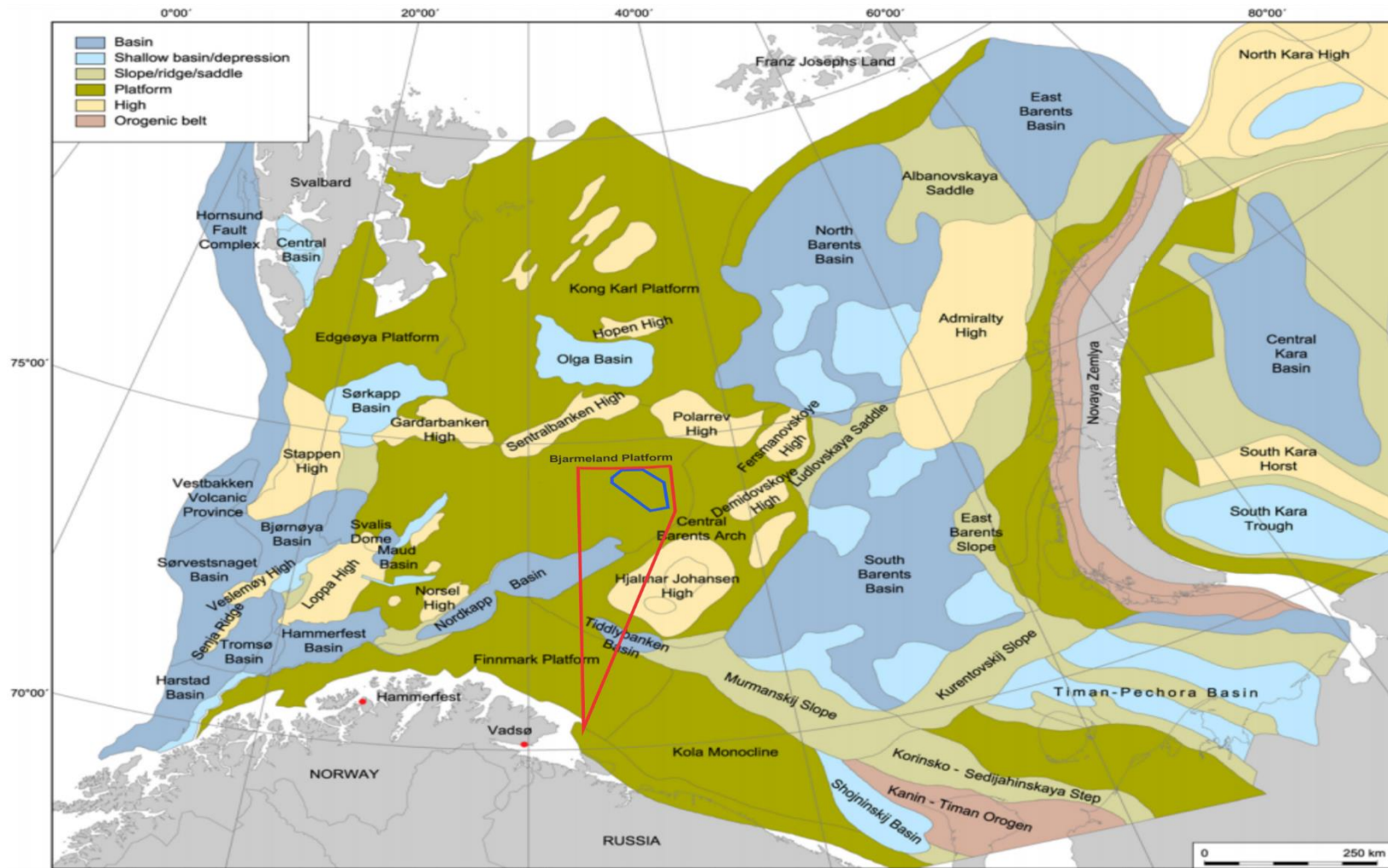


Figure 2.1: Structural elements of the greater Barents Sea. The red section covers the area of BSSE, whereas the blue polygon represents the study area. Note that this figure was developed before the Haapet Dome was formally mapped. Modified from Henriksen et al. (2011a).

## **2.3 Geological setting of the Haapet Dome area**

The Haapet Dome area is characterised by an irregular circular dome structure. The Haapet Dome has gone through several periods of tectonic events, involving potential salt withdrawal (subsidence of denser sediments with adjacent upwards movements of salt) (Mattingsdal et al., 2015), rapid differential loading of lower Triassic sediments (Dellmour et al., 2016) or associated with tectonic inversion (Hassaan et al., 2019).

### **2.3.1 Carboniferous to Permian**

From Late Carboniferous to Permian age, a substantial build-up of reefs overlies clastic sediments from the Gipsdalen-group (figure 2.2), which are accumulated in a deeper basin with a sequence of evaporitic deposits located in-between. (Dellmour et al., 2016). During Late Carboniferous, the climate changed in the direction of more arid environmental condition. Deposition of halite during this period would play a vital role in further development. Eventually, a thin layer of evaporites accumulated above, alongside an adjacent reef build-up of Early Permian time (Dellmour et al., 2016). The Permian age would mark the establishment of the Bjarmeland Platform (Larssen et al., 2002). Late Permian represented a succession of marine black shale that could hold potential for oil and gas generation (Henriksen et al., 2011a).

### **2.3.2 Triassic**

Large amounts of shales and sandstones were deposited during this timeframe (figure 2.2) (Faleide et al., 2010), which originated from the southeast, sourced by the Uralides (Hassaan et al., 2019). The Bjarmeland Platform would have had a moderately low impact of tectonic movements in the course of this timespan (Henriksen et al., 2011a)

Hence, the rapid sedimentary loading was suggested by Dellmour et al. (2016) to be the triggering mechanism of halokinetic process (salt movement) within the Haapet Dome. The sedimentary progradation from the east probably caused movements of salt under the influence of gravity (Dellmour et al., 2016). In combination with differential loading of sediments, the Novaya Zemlya fold-and-thrust belt initiated. This tectonic event was an important factor for further influences on the geological development of the Haapet Dome (Hassaan et al., 2019).

### **2.3.3 Jurassic and Cretaceous period**

The Early Jurassic is characterised by a generally stable tectonic period. The Early Jurassic marks a period with the formation of comprehensive deltaic and alluvial systems (Henriksen et al., 2011a), involving large intervals of sandstone deposits (Faleide et al., 2010). This interval is represented by the Stø, Nordmela and Tubåen formations in figure 2.2.

During the period, the central Barents arch (separating the eastern and western provinces of the greater Barents Sea) developed a positive high structure, which might have acted as a drainage pathway to the surrounding areas, including the Haapet Dome. (Henriksen et al., 2011a)

Deep basins and exposed platforms, due to differential in subsidence and uplift, led to anoxic marine conditions in the Late Jurassic. This would give rise to a highly organic rich shale deposit, represented by the Hekkingen Formation (Henriksen et al., 2011a), overlain by a unit of shales (figure 2.2) (Henriksen et al., 2011a).

According to Mattingsdal et al. (2015), thinning of the lower Cretaceous sequence at the Haapet Dome suggests that the initial phase of doming commenced in the Early Cretaceous and probably during even earlier stages. Salt withdrawal or regional tectonic events seem to have been the triggering mechanisms behind the continuous dome development (Mattingsdal et al., 2015). The Bjarmeland Platform would remain moderately stable throughout the Mesozoic (Henriksen et al., 2011a).

### **2.3.4 Cenozoic Era**

The early Cenozoic Era is characterised by a possible continuous doming of the Haapet Dome area (Mattingsdal et al., 2015). Uplift and erosion further pursued at the Bjarmeland Platform, while the basins to the west continued receiving a large amount of sediments in combination with subsidence (Smelror et al., 2009). By correlating with the western parts of the Norwegian Barents Sea, fluvial and coastal processes were the main factors for the erosion of sediments during early to middle Cenozoic (pre-glacial) (Lasabuda, 2018).

The transition between Neogene to Quaternary times characterised extensive glaciation across the western Barents Sea, where glacial erosion and transportation of sediments from the continental shelf (eastern parts) to the margins (western parts), further pursued. A net erosion between 1300 and 2500 meters of sediments has been removed across the Bjarmeland Platform (Lasabuda, 2018).

The Upper Regional Unconformity (URU) marks the boundary between a thin sub-horizontal glacial sedimentary unit with underlying steeply dipping layers of pre-glacial sediments. The hiatus is represented by potentially several erosional phases, including erosion from various glaciation periods (Larsen et al., 2003; Ottesen et al., 2009; Vorren et al., 2011). The glaciated sedimentary unit is represented by the Naust Formation, which primarily consists of an interbedded matrix of sand, claystone and siltstone. (NPD, 2017b).

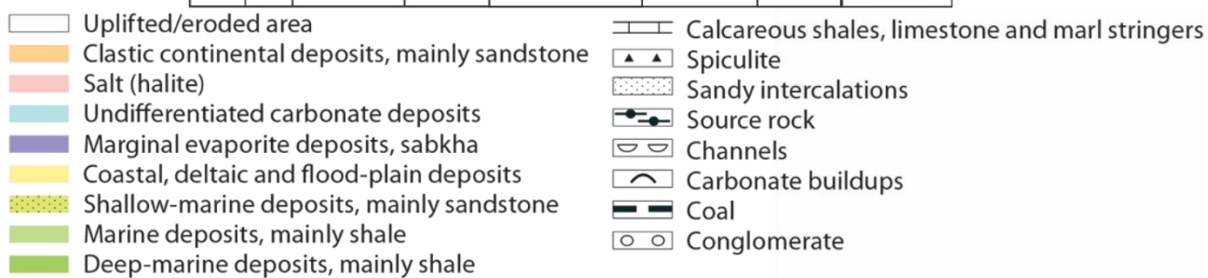
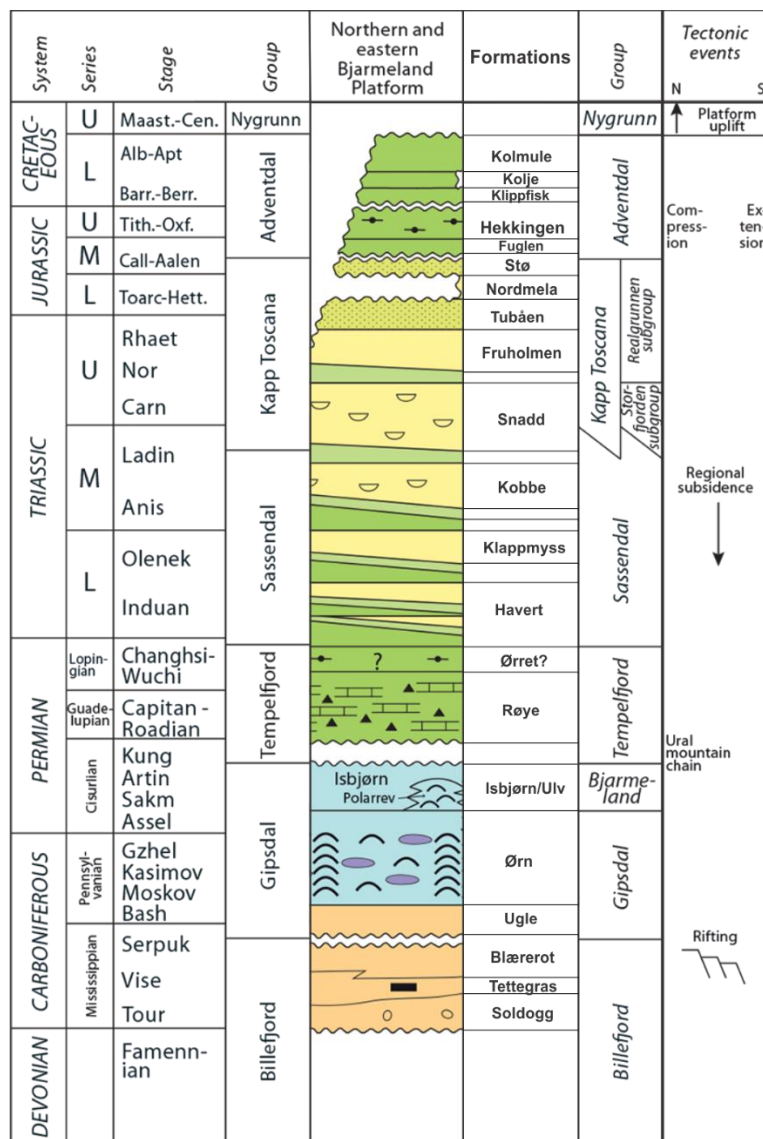


Figure 2.2: Chronostratigraphic and lithostratigraphic diagram for the northern and eastern parts, including the study area and the Haapet Dome of the Bjarmeland Platform. Modified after NPD (2017c).

### 3 Theoretical framework

#### 3.1 Seismic reflection theory

The seismic reflection method comprises acoustic waves that propagate through the subsurface. Each geological structure and unit correspond to different geological compositions, where the energy of waves is reflected according to their acoustic impedance contrasts (figure 3.1) (Micallef, 2011). The acoustic impedance across a boundary is the product of density ( $\rho$ ) and the velocity of the sound wave ( $V$ ) derived from equation 4.1 (appendix 10.1).

Different rock types have distinct geophysical properties, where the acoustic impedance contrast indicates whether the energy travels through a soft towards harder rock or vice versa. (Kearey et al., 2002).

The reflection coefficient equation for a normal incident ray is obtained from appendix 10.1 (Equation 4.2). The reflection coefficient, as also shown in figure 3.1, can either be positive ( $Z_2 > Z_1$ ), meaning that softer rocks overlies harder rocks, or negative ( $Z_2 < Z_1$ ), meaning that harder rocks overlies softer rock properties (Kearey et al., 2002; Wiley & Sons, 2011).

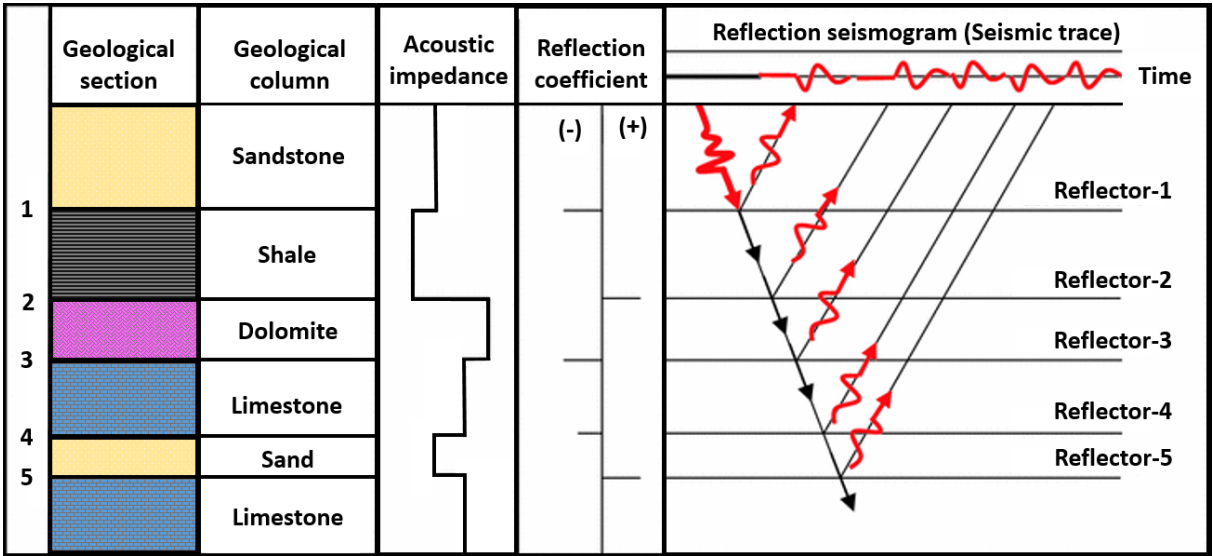


Figure 3.1: Outline of a convolutional model displaying the behavior of a seismic trace. Modified from Alsadi (2017).

### 3.1.1 Seismic resolution

Seismic resolution is the ability to differentiate between two separable features of a certain extent, or by detection of their smallest structural limits determined by the length of its pulse. The potential for a feature to be detected on seismic data additionally depends on how well the data has been processed and how the seismic acquisition method has been applied (Kearey et al., 2002). Thereby, seismic resolution measures how long and thick a structural feature or an object must be to be visible.

With increasing depth, the frequency will decrease while velocity and wavelength will increase. By gradually sedimentary compaction, propagation of sound waves will occur faster with increasing depth. On the contrary, deep travelling seismic waves initiate as higher frequented seismic signals, where they progressively are absorbed, resulting in lower dominant frequencies at deeper depths. In other words, with increasing depth, the seismic resolution quality will be poorer (figure 3.2) (Kearey et al., 2002; Rafaelsen et al., 2002).

For detection of the acoustic impedance contrasts, the resolution has both a vertical and horizontal aspect (Brown, 1992). Together, the aspects rely on the seismic wavelength ( $\lambda$ ), which is a product of frequency ( $f$ ) and velocity ( $v$ ), which can be estimated from Equation 4.3 (Appendix 10.1).

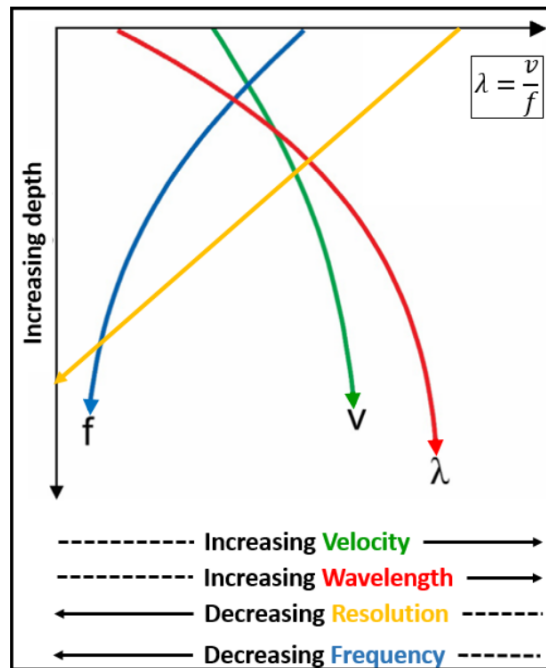


Figure 3.2: Displaying each type of factor that affects the seismic resolution according to increasing depth. Modified after Brown (1992).

## Vertical resolution

The ability to recognise and differentiate between two individually close-lying seismic events related to different depth levels is acknowledged as the measurements for vertical resolution, also known as the tuning-effect (Chopra et al., 2006; Roden et al., 2017). The limit of separability is a critical factor for understanding how thick a layer must be to be visible in a seismic dataset.

Measurements below the tuning effect will result in overlap and interfering of seismic pulses, meaning that no reflection will be visible on the seismic data. As a result, closely spaced seismic reflections may exhibit constructive interference and generate a single seismic reflection with a stronger amplitude contrast. Figure 3.3 illustrates where a wedge-shaped sandstone pinches out from the seismic section and progressively disappearing. The maximum interference for a reflected pulse occurs at one-quarter of the dominant wavelength ( $\lambda$ ) (Kearey et al., 2002; Roden et al., 2017), which can be derived from Equation (4.4) (Appendix 10.1).



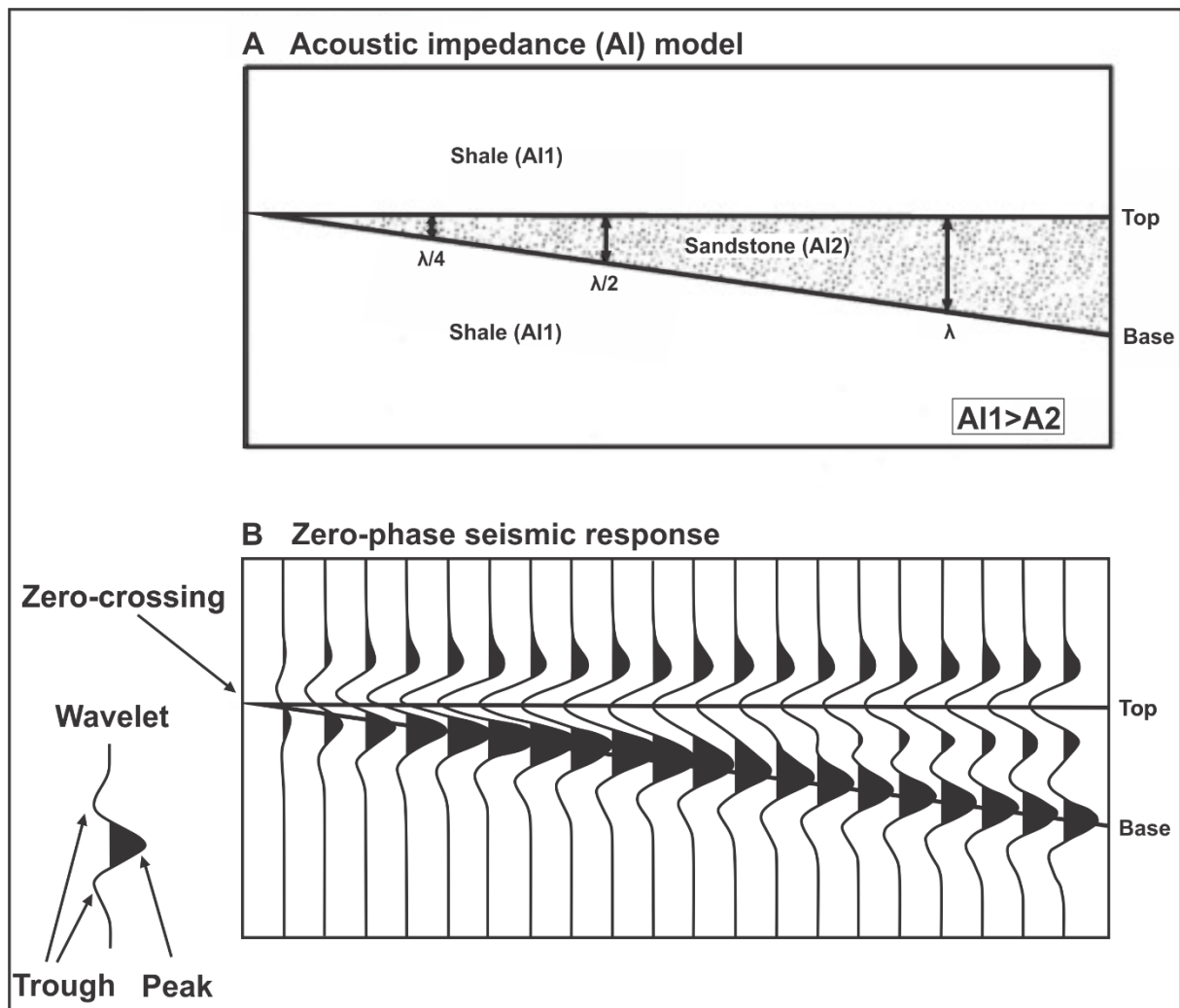


Figure 3.3: (A) Acoustic impedance (AI) model of a sedimentary wedge illustrating the AI-contrasts between layers of shales surrounding a sandstone. (B) A zero-phase, normal polarity pulse (SEG standards) that shows the limit of separability (maximum interference,  $\lambda/4$ ). Modified from Aminzadeh & Dasgupta (2013).

## Horizontal resolution

The theory emphasises the ability to resolve laterally displaced objects and distinguish them as separable seismic events (Chopra et al., 2006). The energy generated by a shot point reflects the propagation of soundwaves through a medium. These soundwaves travel with a three-dimensional spherically pathway where the reflected signals originate from a surface area defined as the Fresnel zone. The horizontal resolution is controlled by two factors: The intrinsic to the physical processes of a wave and the detector spacing during the gathering of seismic surveys (Brown, 1992; Kearey et al., 2002).

Features in the subsurface that have a lateral extent that exceeds the Fresnel zone will be visible. In contrast, objects with a lateral extent that is less than the Fresnel zone will cancel out in the seismic dataset (Aminzadeh & Dasgupta, 2013).

According to the Equations 4.5, regarding unmigrated horizontal resolution (derived from the Appendix 10.1), the radius of the Fresnel zone increases with depth (figure 3.4A), while velocity increases and the frequency is reduced. Consequently, the horizontal resolution decreases with increasing depth. Seismic migration is often applied to improve the lateral resolution. It comprises three primary functions, which are reposition of the reflection, focusing the energy spread over a Fresnel zone and finally processing of collapsing diffraction patterns (Brown, 1992).

One way to compensate for an increase in horizontal resolution is to decrease the radius of the Fresnel zone. For a situation where the radius is post-migrated (figure 3.4B), the horizontal resolution will be equivalent to one-quarter of a wavelength ( $\lambda/4$ ) (Brown, 1992).

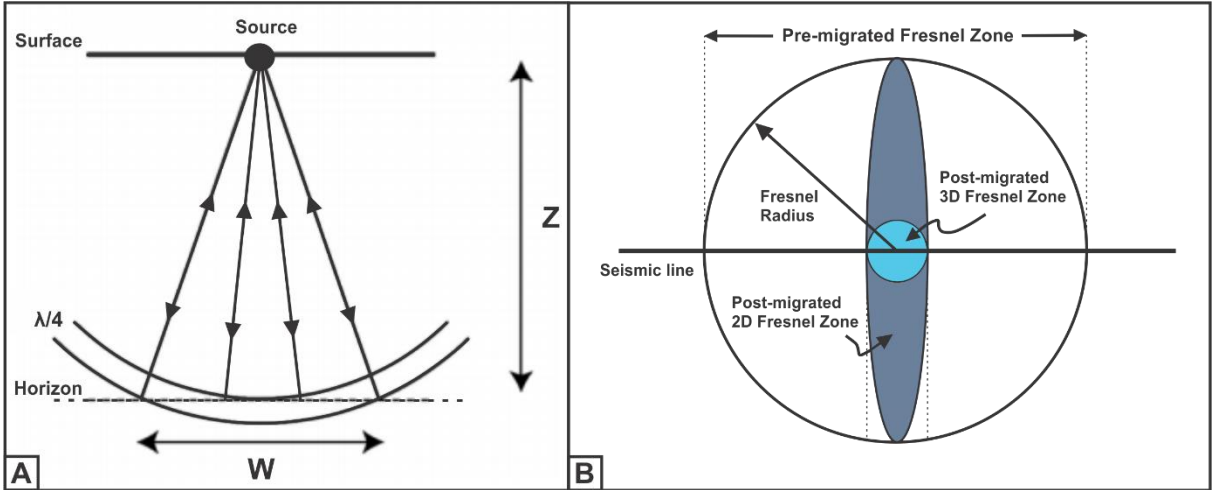


Figure 3.4: (A) Illustration of the Fresnel zone (W) considering the distance (Z) from source to reflector. Modified from Kearey et al. (2002) (B) Fresnel zone before and after migration of 2D and 3D seismic data. Modified from brown (1992).

## 3.2 Fault configuration

A fracture zone between two rock formations classifies the origin of an individual fault or a zone of multiple fault planes. Such brittle deformation (breaking of materials due to fracturing) may commonly occur during movements and displacements of rocks. The zone of fierce fracturing of rocks is defined as the fault core, which can vary between a few millimetres to more than several metres (Martel, 1990; Fossen & Bale, 2007). In other words, “faulting occurs when the maximum differential stress (e.g., maximum stress  $\sigma_1$  minus minimum stress  $\sigma_3$ ) exceeds the shear strength of an intact rock formation or the frictional strength of a pre-existing fault” (Rey, 2016, p. 19).

### 3.2.1 Dip-Slip faults

The fault development may be complex, due to the variability in its orientation, dependent on the fault angle and its direction of slip (Bryant, 2016).

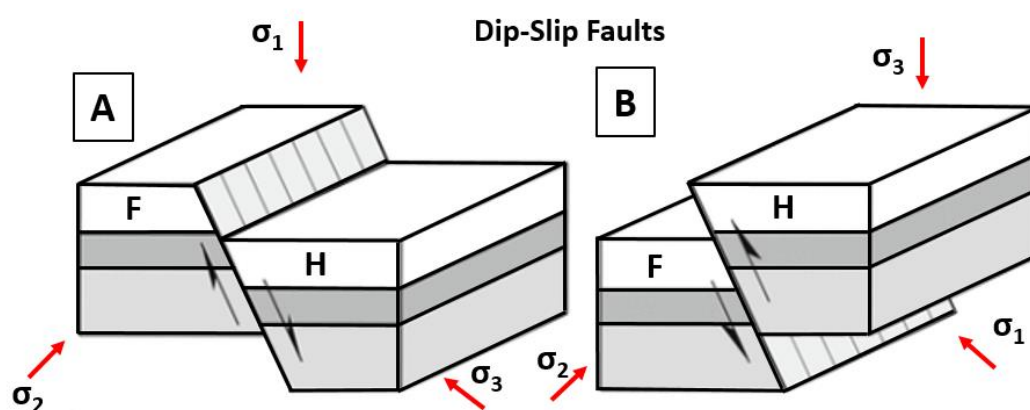


Figure 3.5: Diagram that shows the concept of (A) normal faulting and (B) reverse faulting. Black arrows indicate the direction of movement, whereas red arrows indicate the level of compressional movement. H: Hanging wall, F: Footwall. Striation displays the general direction of the fault plane. Modified from Bryant (2016).

Dip-slip faults are defined as crustal movements of blocks, where the axis with maximum compressional forces determines whether it is a normal or reverse fault. If the displacement of the hanging wall is located further down relative to the footwall, the crustal movement characterises normal faulting (figure 3.5A). The opposite displacement will then resemble reverse faulting (figure 3.5B) (Bryant, 2016).

Normal faults commonly originate from extensional tectonic settings, in particular oceanic spreading and continental rifting. These types of faults develop during maximum vertical compression ( $\sigma_1$ ) in the course of crustal extension, with a minimum horizontal compressional stress ( $\sigma_3$ ). They often occur as steeply dipping fault planes (50°-70° angle of dip). Although, the dip of several normal faults (listric faults or low-angle detachment faults) shows evidence of a decrease in angle with increasing depth (Bryant, 2016).

Compared to its counterpart, reverse dip-slip faults (figure 3.5B) forms during contraction of plate boundaries, for instance, subduction zones or collision of two continents. It comprises a maximum horizontal compressional stress ( $\sigma_1$ ) and a minimum vertical compressional force ( $\sigma_3$ ) (Bryant, 2016).

### **3.3 The petroleum system**

The concept behind a petroleum system (figure 3.6) is defined as “A pod of active source rock and all genetically related oil and gas accumulations.” (Magoon & Beaumont, 2003, p.5), considered that all the geological elements and processes are present for hydrocarbons to accumulate (Selley & Sonnenberg, 2015).

Such critical elements are the presence of source rock, reservoir rock, sealing rock and overburden sediments. For the required processes, the petroleum system is reliant on hydrocarbon generation, permeable migration pathways, accumulation area for hydrocarbons, preservation and entrapment of the petroleum deposits (Selley & Sonnenberg, 2015). The geological elements and processes must be timely preserved in such a manner that the conversion of organic matter to hydrocarbon accumulation may occur (Magoon & Dow, 1994).

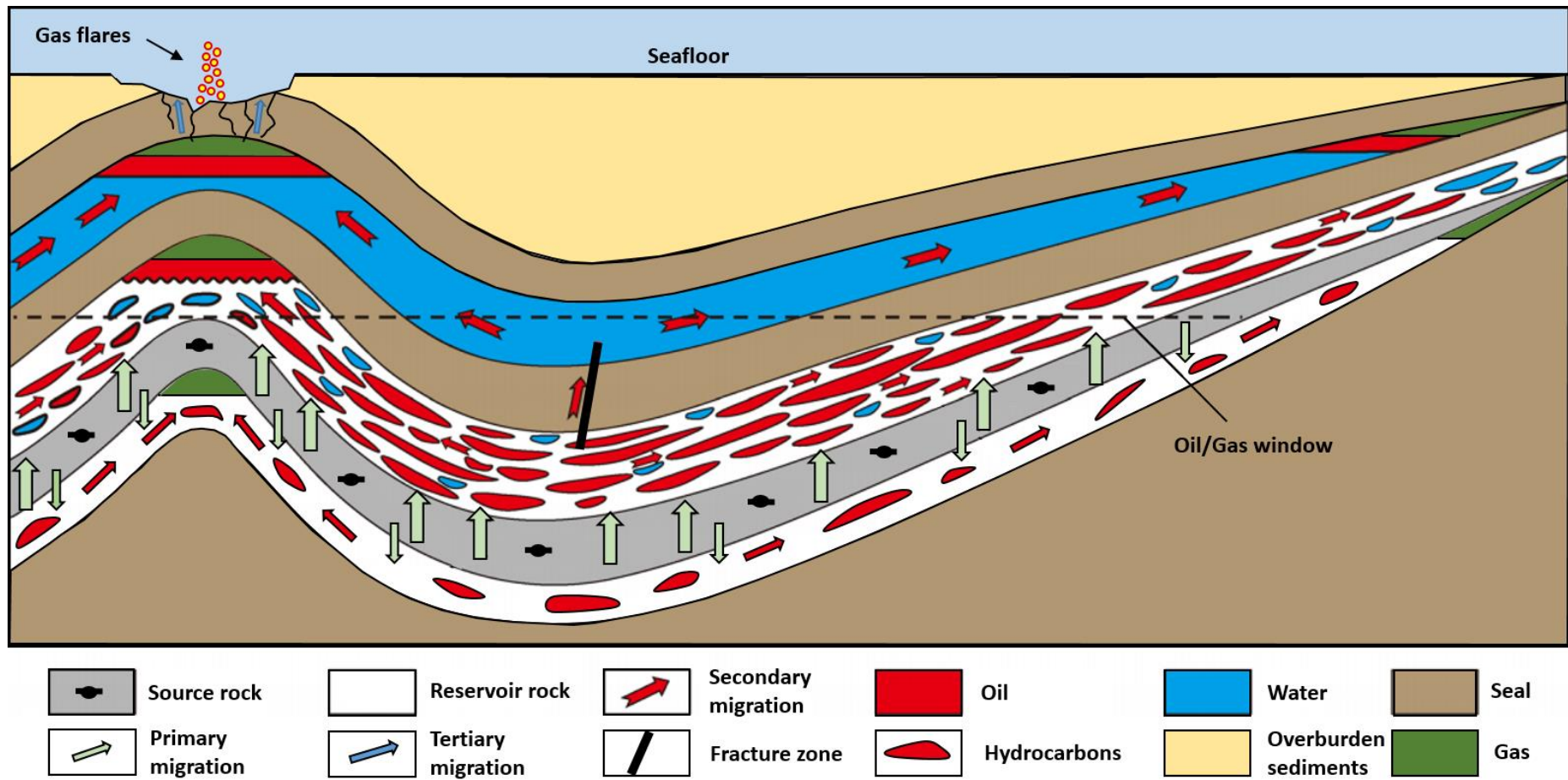


Figure 3.6: Illustrating a working petroleum system and its essential geological elements and processes involved for hydrocarbons to generate, migrate and potentially accumulate within a zone of entrapment. Modified after Zhao et al. (2018).

### 3.3.1 Source rock

A source rock involves a fine-grained sedimentary rock that encloses a substantial amount of preserved organic matter. If heated sufficiently, the source rock can generate and expel hydrocarbons and potentially develop an accumulation of petroleum (figure 3.6). Source rocks are typically shales or limestones, which can be categorised by the amount of oil generated. Thus, for source rocks that have yet to generate hydrocarbons implies an immature source rock. Source rocks that are generating hydrocarbons indicate a mature source rock. As importantly, the third stage defines a post-mature source rock, which formerly has generated all its hydrocarbons (Al-Areeq, 2018).

Identifying the type of organic shale depends on the chemistry of each kerogen. Kerogen is recognised as a naturally occurring organic matter that arises in source rocks generated as either oil or gas upon maturation (Selley & Sonnenberg, 2015).

When the exposure of significant temperature and pressure is applied, the evolution of the complex hydrocarbon, kerogen, commences. It occurs through three stages, which are the Diagenesis, Catagenesis and Metagenesis (figure 3.7). Diagenesis characterises the early evolutionary stage involving normal temperature and pressure of the shallow subsurface. Primarily, the diagenesis of the organic matter results in a reduction of oxygen molecules, while the carbon ratio remains unmodified (Henriksen et al., 2011a; Selley & Sonnenberg, 2015).

Catagenesis is the second stage, where the rate of pressure and temperature increases by burial and depth. During this stage, petroleum (mainly oil) is expelled from the kerogen. Metagenesis characterises the latest stage of evolution. It encompasses additional temperature and pressure verging on the rate of metamorphism. The remaining hydrocarbons are now being expelled, mainly methane. At this point, porosity and permeability are now irrelevant, due to the rocks being roughly impermeable and containing low percentages of porosity at this level. (Selley & Sonnenberg, 2015). Generation potential and the quality of the organic matter (kerogen) can be determined by using geochemical data, for instance, total organic carbon (TOC wt%), rock-eval pyrolysis, bitumen extraction or vitrinite reflectance (Al-Areeq, 2018).

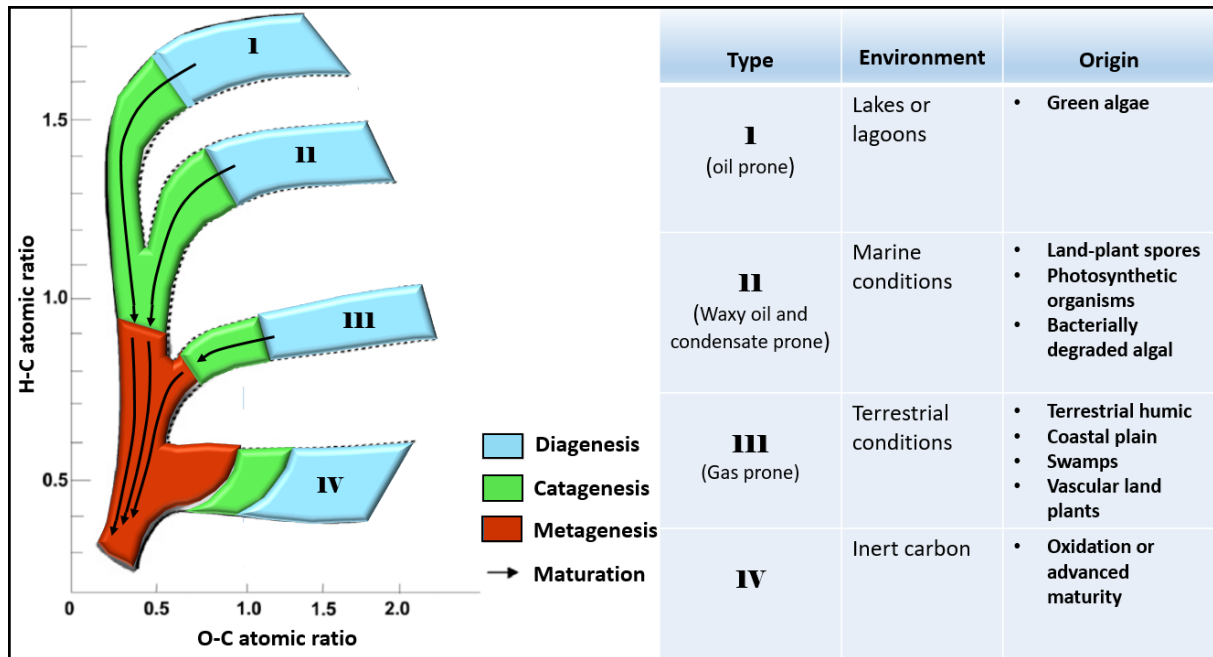


Figure 3.7: Van Krevelen diagram, combined with a schematic illustration of environmental deposition and origin, displays the evolution of various kerogen types, dependent on the rate of pressure and temperature applied. The evolutionary rate of each type of kerogen is illustrated in relation to Hydrogen/Carbon (H/C) and Oxygen/Carbon (O/C) ratio. During Catagenesis, oil generation will commence. If the H/C ratio is less than 0.5, the kerogen will start to produce methane. Modified from Walters (2007).

### 3.3.2 Reservoir rock and fluid migration

The main types of reservoirs are sedimentary rocks, such as carbonates or sandstones. Essentially, a reservoir is a body of rock that has an acceptable percentage of porosity and permeability (connection of pores) to store and transfer fluids (water, oil or gas). Some of the primary factors regarding reservoir quality depend on depositional properties (fabric characteristics and texture), diagenetic properties (compaction trends) and depth of burial. These factors need to be considered when evaluating the properties of fluid flow. (Terry & Rogers, 2014; Worden et al., 2018).

Hydrocarbons that accumulate in reservoir rocks originate from a source rock. When the source rock exceeds critical rates of burial, the stage of hydrocarbon expulsion will initiate (Pang et al., 2006). In consequence of expulsion, an increase in upwards pressure (buoyancy) develops, which may yield the hydrocarbons the ability to surpass the pore capillary pressure (pressure differences between two immiscible liquids, e.g. oil and water) if the forces of buoyancy are sufficient (Schowalter, 1979). In this case, movement and migration of hydrocarbons may proceed (figure 3.6).

Migration of hydrocarbons occurs through several stages. Primary migration represents the first stage of migration, where hydrocarbons emigrate from its less porous source rock to adjacent more porous carrier beds (reservoir rocks) or by following potential fracture zones (Selley & Sonnenberg, 2015). When substantial amounts of hydrocarbons are collected, secondary migration can arise (Schowalter, 1979).

Secondary migration emphasises the movement of generated hydrocarbons through permeable carrier beds after expulsion. Oil and gas will subsequently migrate until it encounters an entrapment zone, resulting in an area of petroleum accumulation. Since nearly all pore spaces in the subsurface are water-saturated, the presence of water is expected. Considering that water is denser than both oil and gas, plus oil is denser than gas, the top of the entrapped reservoir will contain sediments saturated with gas, with an underlying layer of oil-saturated sediments and a bottom layer of water-saturated sediments (Schowalter, 1979).

If trapped hydrocarbon accumulations are interrupted by folding, faults or by uplift, the hydrocarbons will re-migrate from its initial accumulation space. Potentially, the hydrocarbons may relocate to another zone of entrapment or even migrate towards the surface, resulting in seepage. This late-stage migrational event is termed tertiary migration (Kovacs & Zilahi-Sebess, 2018).

The general drainage pattern for hydrocarbons can be divided into vertical and horizontal migrational movements (figure 3.6). Given that permeable carrier beds encompass an upper less-permeable sealing rock, the hydrocarbons will naturally migrate laterally up-dip, unless the forces of buoyancy exceed the capillary pressure. In this case, vertical drainage may proceed, until the hydrocarbons encounter a new carrier bed with impermeable overburden rocks, resulting in further horizontal migration. In scenarios where a carrier bed is faulted or fractured, the hydrocarbons will utilise its vertical pathway to migrate towards areas of lower pressures (England et al., 1987).



### 3.3.3 Traps

For hydrocarbons to accumulate within a reservoir, an upper relative impermeable sealing rock is required to prevent the movement of oil or gas to migrate further. Such entrapment is referred to as a trap structure (Selley & Sonnenberg, 2015). Timing is an essential factor, where the formation of a sealing rock is necessary to develop before movements of hydrocarbons takes place (Magoon & Beaumont, 2003).

Oil and gas accumulate at the uppermost part of the trap, termed the culmination. If the trap is filled to its spill-point (lowermost part of a trapped reservoir), hydrocarbons will re-migrate until it encounters another trap. The vertical distance from the structural culmination, to the area of spill-point, is the closure of the trapping structure (Selley & Sonnenberg, 2015).

The trap configuration for hydrocarbon storage may comprise a dip closure, fault-bounded dip closure, combinational trap or a stratigraphic pinchout trap (Veeken, 2007). Some of the most common structural closures are folded anticlines and faults juxtaposed traps, which may act as impermeable seals. Anticlines may be described as four-way dip closures, whereas structural traps that are disrupted by faults can be described as possible fault-bounded closures (Allan, 1989; Fajana et al., 2019).

Several types of traps may develop, where some of them are mentioned below, which includes structural traps, stratigraphic traps, hydrodynamic traps and a combination. Structural traps forms during post-depositional tectonic processes, involving deformation of strata through faulting (figure 3.8) or folding (figure 3.9) (Selley & Sonnenberg, 2015).

Stratigraphic traps (figure 3.10) originates when the geometry of the lithological unit is modified, for instance, pinchout and unconformities. The different changes may occur during original deposition (e.g. reef build-ups, barrier bars and channels) or post-deposition (e.g. truncations and diagenetic changes). Hydrodynamic traps (figure 3.11) represents downward hydrodynamic movements of water within permeable bedding, which counteract and prevent upwards migration of oil and gas, provided that the hydrodynamic forces are greater than the forces of buoyancy. If a combination of two or more of the various types of traps occurs, a combination trap (figure 3.11) is developed. A most common combination is between structural and stratigraphical processes (Selley & Sonnenberg, 2015).

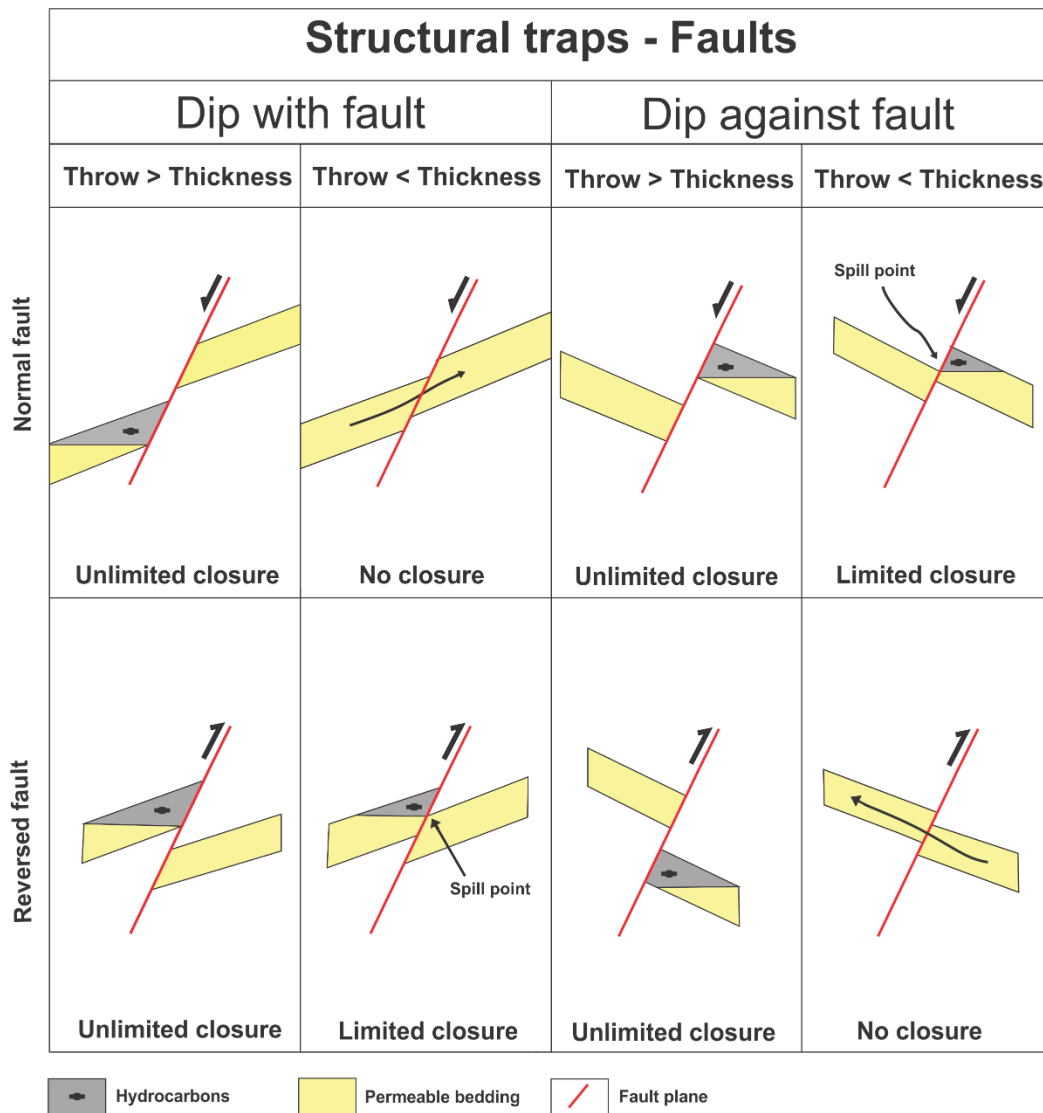


Figure 3.8: The theoretical configuration of petroleum traps in combination with faulting. The closure of each trap depends on the amount of throw compared to its thickness. Modified after Selley & Sonnenberg (2015).

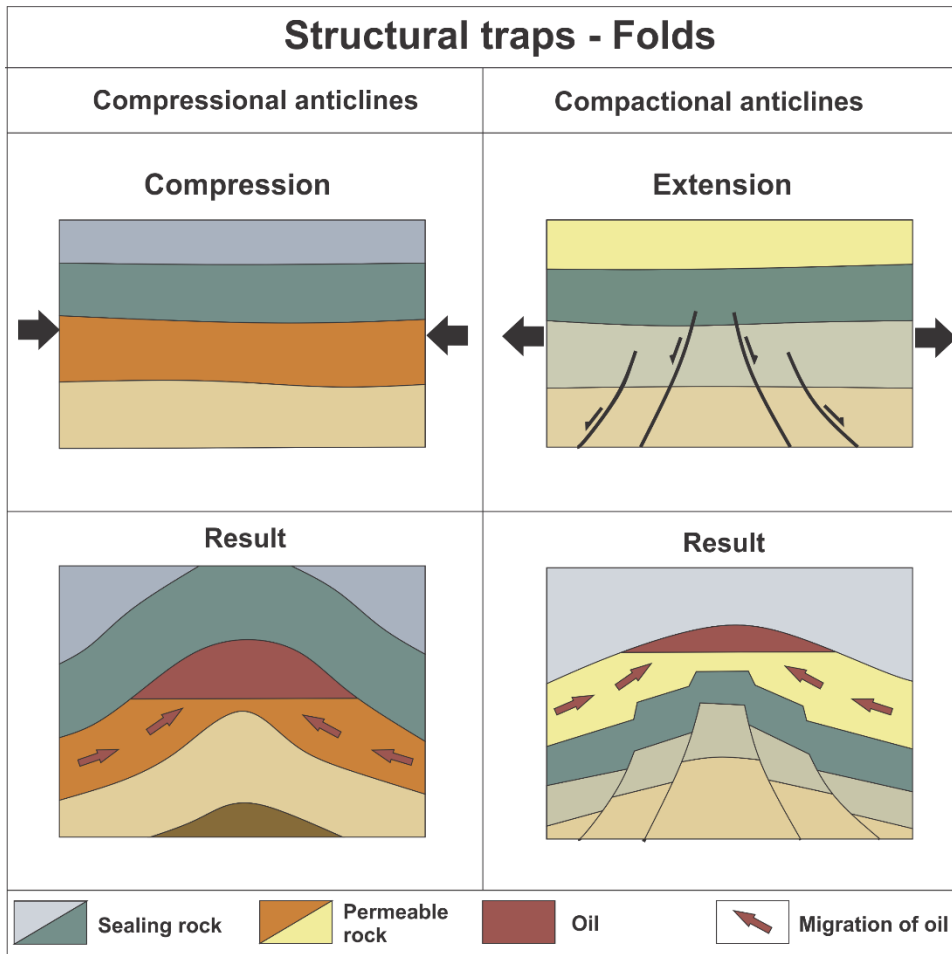


Figure 3.9: Cross-section displaying the development of anticlinal structures in accordance with compressional and extensional tectonic processes. Modified after Selley & Sonnenberg (2015).

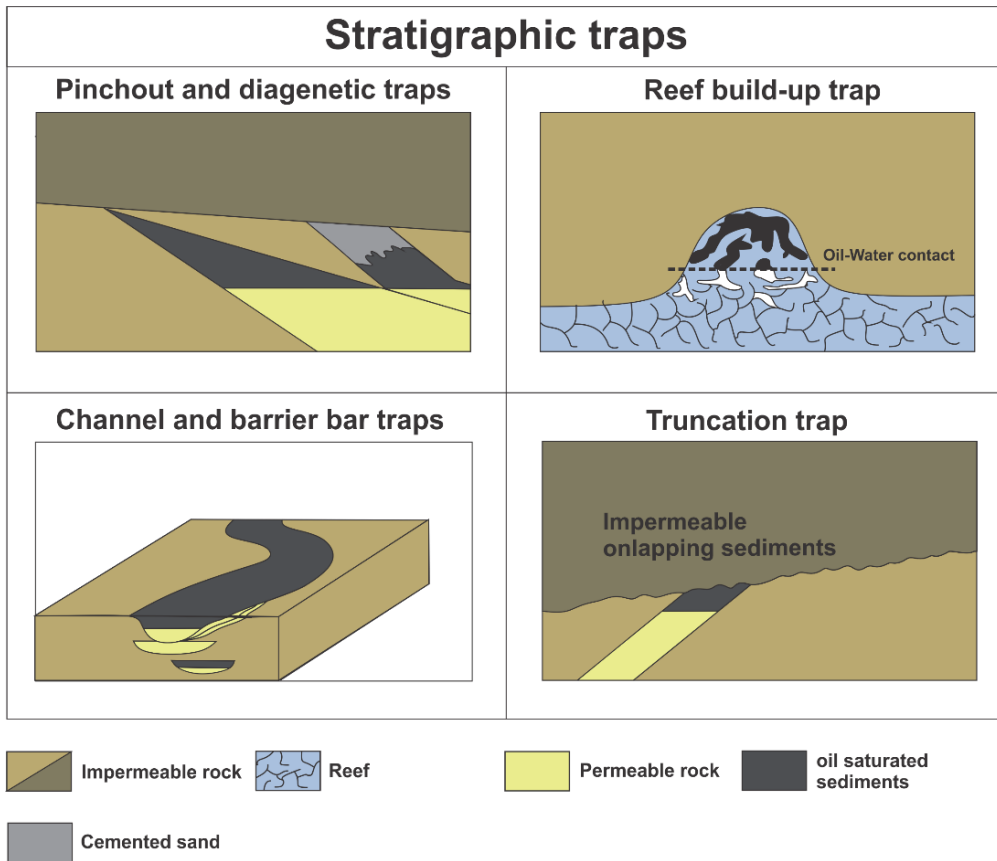


Figure 3.10: Cross-section of the various types of stratigraphic traps. Modified after Selley & Sonnenberg (2015).

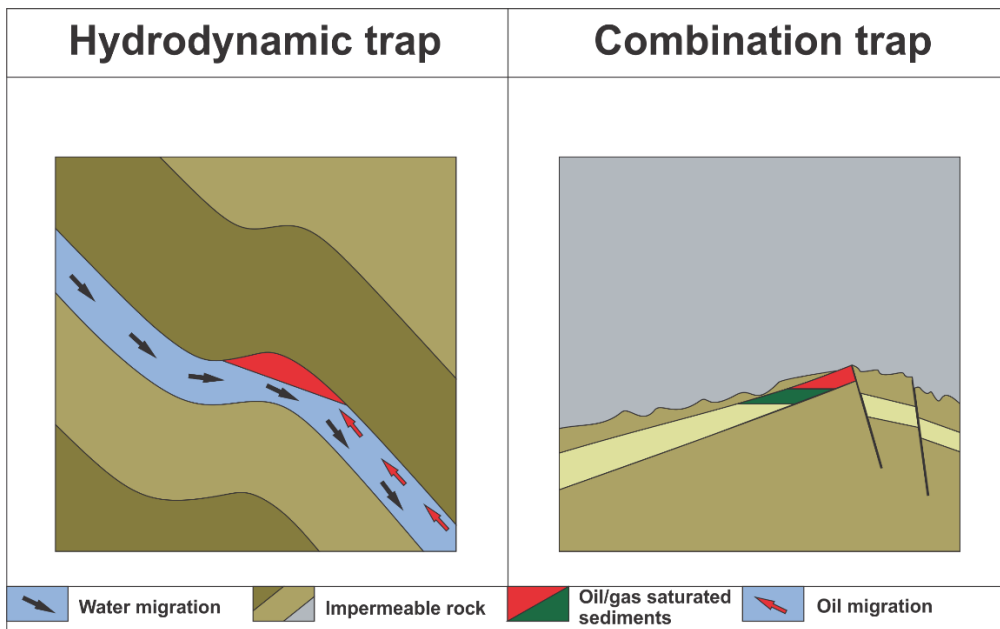


Figure 3.11: Cross-section displaying a pure hydrodynamic trap and a combination trap. Modified from Selley & Sonnenberg (2015).

## **3.4 Direct hydrocarbon indicators**

Direct hydrocarbon indicators have been used to detect hydrocarbon accumulations from acoustic datasets for over 30 years. Most commonly, the method uses the identification of prospects, enclosed by a potential structural or stratigraphic trap formation (Semb, 2009).

A direct hydrocarbon indicator (DHI) is defined as a high seismic reflection amplitude that implies the presence of hydrocarbons within a clastic reservoir. Despite, not all amplitude anomalies may be the occurrence of hydrocarbon accumulations. Seismic reflection amplitudes are results of impedance contrasts, meaning if a sedimentary rock experiences modification of its properties (e.g. compositional changes, change in matrix, fluid composition or porosity), the change in its elastic properties may affect the seismic response by displaying high amplitude reflections, which can be misjudged for hydrocarbon accumulations (Nanda, 2016).

Gas can act as highly compressible, compared to oil and water, when significant pressure is applied. The resulting factor will be lowering of bulk modulus (resistance to uniform compressional forces), making the compressibility of the gas additionally greater. Additionally, primary waves (P-waves) migrating through the subsurface will reflect high amplitude reflections as a response to the substantial reduction in p-wave velocity. Within a seismic section, such high amplitudes are results of reduction in acoustic impedance, which suggest the presence of gas (Nanda, 2016; Singh, 2019).

### **3.4.1 Seismic response of amplitude anomalies**

Various types of seismic amplitude anomalies are characteristic for hydrocarbon-saturated reservoirs. For scenarios that represent a gas-saturated sandy rock, trapped by a structural high, may appear as a discontinuous high seismic amplitude response within the seismic section, most often referred to as a bright spot (figure 5.16A) (Nanda, 2016).

Considering that gas has its velocity significantly reduced during acoustic wave propagation, the resulting factor will lead to a negative reflection coefficient and thereby a negative amplitude anomaly, compared to its adjacent area (Nanda, 2016). The abrupt change from an increase to a decrease (and vice versa) in acoustic impedance results in the reversal of polarity, termed polarity reversal (figure 5.16C – 5.19C), which may indicate the presence of hydrocarbons (Onajite, 2014). Bright spots are frequently associated with lateral lithological changes (Semb, 2009).

A bright spot may contain an upper section of gas accumulation, separated by a water- or oil-contact zone. This hydrodynamic zone represents the contact between two fluids, commonly known as a flat spot (figure 5.16A). In the case of gas-water-contact, the seismic response will generate a strong reflection due to the strong acoustic impedance contrasts between gas and water. Theoretically, fluid contacts may develop either a gas-water-contact (GWC), oil-water-contact (OWC) or gas-oil-contact (GOC). Flat spots are extraordinary for corresponding to fluid contacts, rather than lithological changes. This type of DHI is considered the most effective tool for hydrocarbon identification (Semb, 2009; Nanda, 2016).

Areas within a seismic dataset that indicates acoustic masking (dimmed zones) may suggest the occurrence of gas chimneys. This phenomenon may occur in areas where the sealing capacity is poorly developed, causing upward migration of gas in the form of leakage. The decrease in velocity through hydrocarbons will affect the lowermost intervals by increasing the two-way travel time. The resulting feature will be visualised as a push-down effect. However, push-down effects can also be results of seismic artefacts (Semb, 2009).

### 3.5 Gas hydrates

Gas hydrates are methane gas (or other hydrocarbon gases) that are trapped inside a crystalline-like structure of water molecules. Gas hydrates are highly susceptible to seasonal temperature variations (figure 3.12), meaning that a minor increase in ambient temperature may dissociate them. If the formation of shallow gas hydrates would occur, a combination of high pressure (water column depth) and low temperatures are required. Scenarios with these requirements may give rise to zones of stable gas hydrates. Subsequently, a bottom-simulating reflector (BSR) may develop, which is defined as an observational indicator of the base of stable gas hydrates that imitate the seafloor reflection. Its seismic reflection emits strong acoustic change in impedance with a reversed amplitude polarity relative to the seafloor reflector. The base of the stable gas hydrates may act as an overlying barrier for sediments containing free gas (Chand et al., 2012; Rajput & Naresh, 2016; Plaza-Faverola et al., 2017; Ferré et al., 2020).

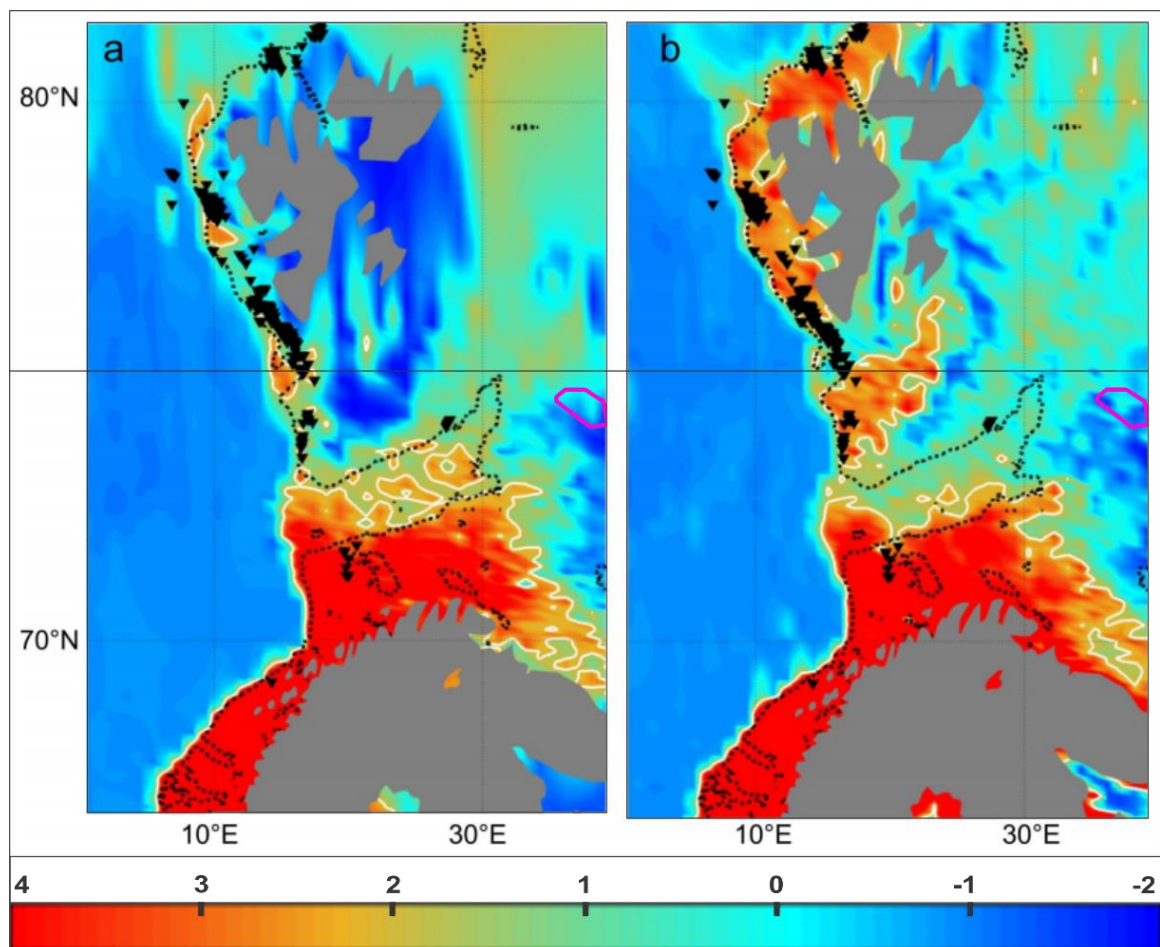


Figure 3.12: Bottom water temperature map situated along the Norwegian-Svalbard margin. (A) Shows the average temperature measured from January to April, whereas (B) displays an average bottom water temperature from July to October. The pink polygon represents the survey area ST14005. Modified from Ferré et al. (2020).

The gas composition and pore-water salinity affect the gas hydrate stability zone (GHSZ). Generally, low order of molecular hydrocarbons (mostly methane) is commonly developed in regions with low temperatures ( $<300$  K) and moderate pressure rates ( $>0,6$  MPa) (Rajput & Naresh, 2016).

Further nucleation of gas hydrates depends on the weight percent of the salt mixture ( $\sim 3,5\%$ ) in free water, concerning the hydrate system within the seafloor, which means that the absence of an inhibitor (e.g. NaCl) will reduce the depth needed for gas hydrates to be stable (Yang & Xu, 2007).

Gas hydrates located above the BSR results in an area of reduced permeability, implying that the BSR may act as a trapping structure for underlying free gas (Madrussani et al., 2010). Although, if the gas hydrates would to dissociate, the methane gas would potentially migrate through the water column and eventually reach the atmosphere (Ferré et al., 2020).

### **3.6 Water column imaging**

The driving forces for upward migration of gas in the bedrock emerge by overpressure (fluid migration) and the forces of buoyancy. In scenarios where gas leakage arises at the seafloor surface, gas bubbles (imaged as flares) are recognised within the water column (Zhao et al., 2017).

Predominantly, gas discharge occurs at depths shallower than the upper boundary of the GHSZ (Mau et al., 2017). Gas bubbles can emerge along faults, craters (pore pressure reduction within sediments after ice loading), zones of glacial erosion or termination of strata (e.g. the GHSZ). Several studies have been conducted relative to identification of gas flares in the Barents Sea area, certifying their existence and origin (Chand et al., 2012; Andreassen et al., 2017, Serov et al., 2017; Crémière et al., 2018).

By using hydroacoustic systems (e.g. a multibeam echosounder), an optimised seabed interaction can be extracted, which may reveal the presence of bubble streams (identified as clouds of strong scatter points) in the water column (figure 3.13). Free gas emits strong acoustic change in impedance, meaning that sonar systems are useful tools for identifying gas seepage along seafloor surfaces (Clarke, 2006; Urban et al., 2017).



The multibeam echosounder (MBES – used in this thesis) is a sensitive sonar system device. Its main advantages are the detection range and lateral coverage in the water column. By using swath imaging, with coverage of  $\sim 120^\circ$ , the MBES outperforms both single and split-beam systems. The WCI (water column image) survey is performed as a set of parallel lines to ensure sufficient water column imaging. These track-lines requires close-lying distribution to minimise the absence of water column data (WCD). The WCD is acquired perpendicular to the ships track-line in order to detect anomalies (Urban et al., 2017; Mareano, 2017).

After processing, the potential flares are evaluated according to the backscatter strength (a measurement of the reflected sound energy from materials in the water column). Gas flares are recognised as clouds of strong backscatter strength. Inclusively, the potential gas flare requires a connection to the seafloor, which sometimes can be difficult to determine. If the gas flare is situated beyond the minimum slant range, the lower parts will be challenging to detect, due to lack of data. As stated by Urban et al. (2017, p. 2), the minimum slant range is defined as “the shortest radial distance between the sonar transducer and the seafloor”. Weak amplitude anomalies may also suggest the occurrence of mammals, shoals of fish, plankton or other microorganisms (Veloso et al., 2015; Mareano, 2017). Gas flares comprise an almost vertical extension, whereas shoals of fish are represented by a horizontal extension that neglects vertical extension (Jansson, 2018).

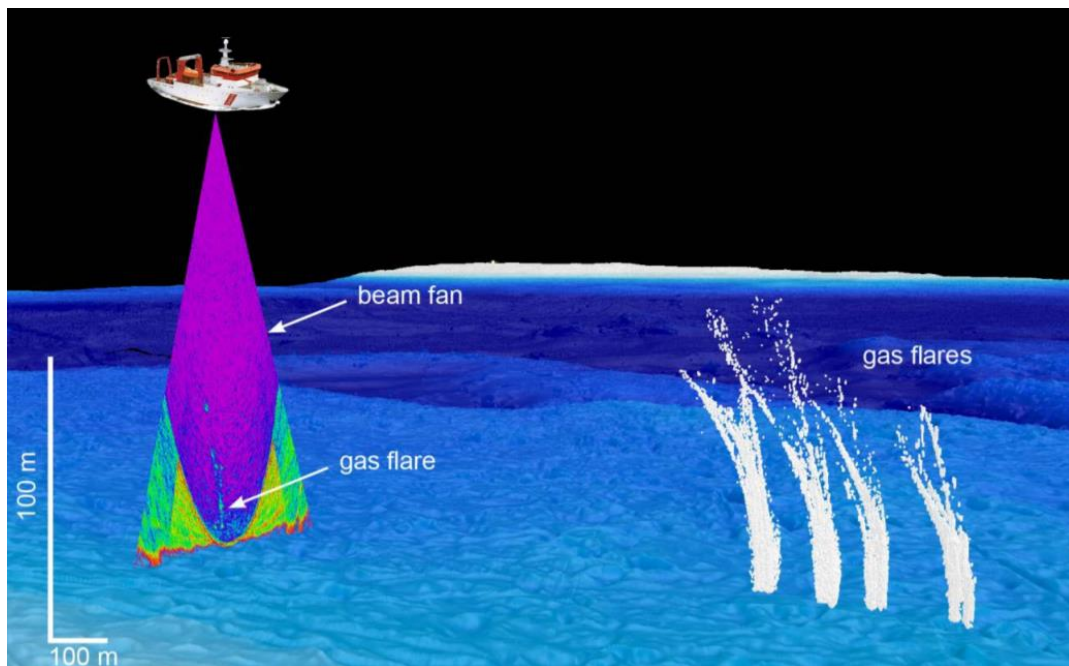


Figure 3.13: Simulating the process of water column data gathering. In this illustration, a Kongsberg EM710 multibeam echosounder system is displayed. The exemplified sonar system shows the presence of gas flares within the beam fan. Retrieved from Mareano (2017).

The WCD may comprise unwanted acoustic responses, such as acoustic artefacts/distortion, related to strong signal reflection from the seafloor interacted with side-lobe artefacts or ambient noise (figure 3.14A). Acoustic artefacts are therefore essential to identify and exclude from the WCD survey, to avoid degraded data quality (figure 3.14B) (Urban et al., 2017).

The upwards propagation of gas bubbles through the water column varies according to water currents and tidal influence. In areas where these factors are present, gas seepage is recognised as an oblique extensional shape in the WCI data (figure 3.13) (Urban et al., 2017).

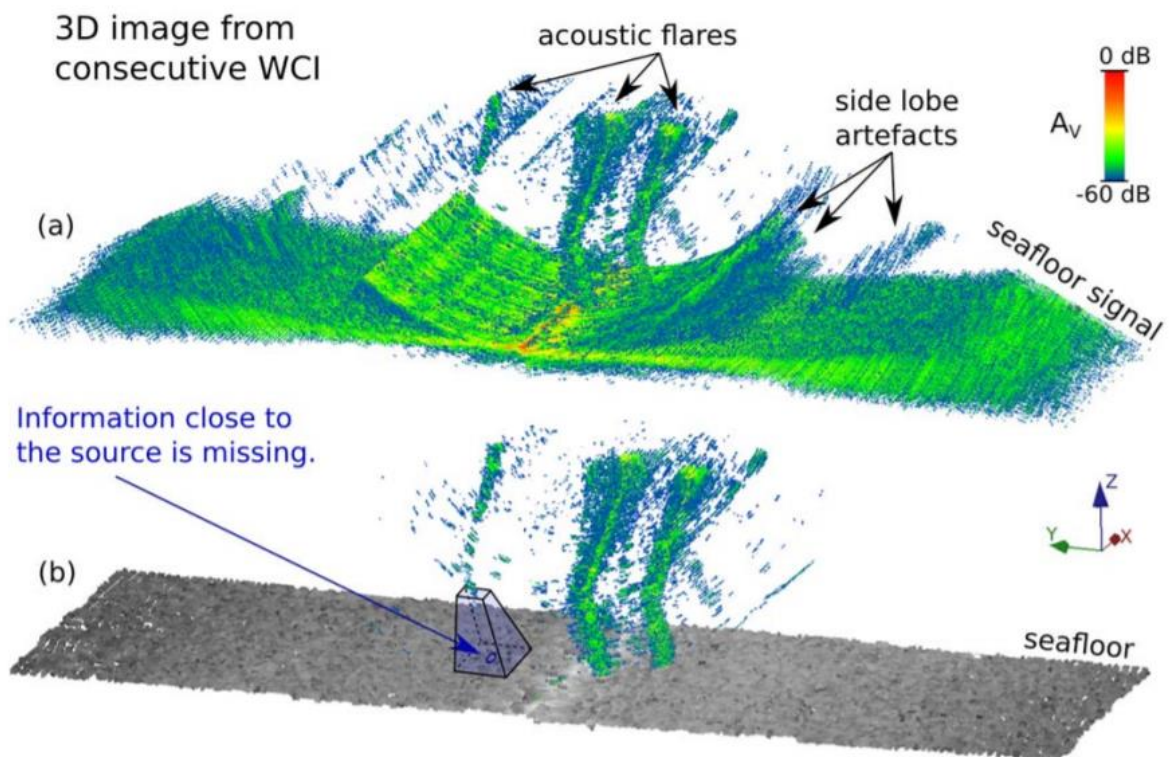


Figure 3.14: A 3D image from 120 consecutive water column images. (A) Displays three flares that are visible within the minimum slant range. Artificial side-lobes can be observed on the flanks of the minimum slant range. Note that only signal points above -60 dB are present. (B) Only shows the remaining flares. All the exceeding signal points situated outside the minimum slant range are removed. Retrieved from Urban et al. (2017).

### 3.7 Pockmarks

Pockmarks are circular depressional features within the seafloor that exhibits significant variations in size and shape (figure 5.22A). These features are suggested to have been formed through eruptions of gas, due to overpressure of shallow gas accumulations, or as a result of fluid discharge (Hjelstuen et al., 2010). Jensen et al. (2015) propose that most of the pockmarks in the Barents Sea originated after the retreat of the last glacial ice-sheet.

Generally, pockmarks are often associated with gas expulsions from subsurface sediments. Several geologists have used this theory as a potential guideline for hydrocarbon exploration. Pockmarks are commonly observed above zones of shallow gas hydrates, concordant with vertical chimney features situated underneath. Such observations may indicate upward fluid migration, potentially resulting in gas expulsion from the seabed (Rise et al., 2015).

## 4 Data and methodology

### 4.1 Datasets

The study area is defined by the seismic 3D dataset ST14005 (figure 4.1), which covers a region of approximately 5593km<sup>2</sup>. The survey was acquired in 2014 by PGS Geophysical AS, on behalf of Statoil ASA (Equinor ASA). General information about the seismic 3D dataset is presented in table 4.1.

*Table 4.1 – Overview of the seismic survey used in this study. Obtained from NPD (2019c).*

Survey name	Sub type	Company responsible	Year completed	Size	Location	Phase configuration
ST14005	3D	Statoil ASA (Equinor ASA)	2014	5593km <sup>2</sup>	Northeastern parts of the BSSE	Zero phase. Normal polarity

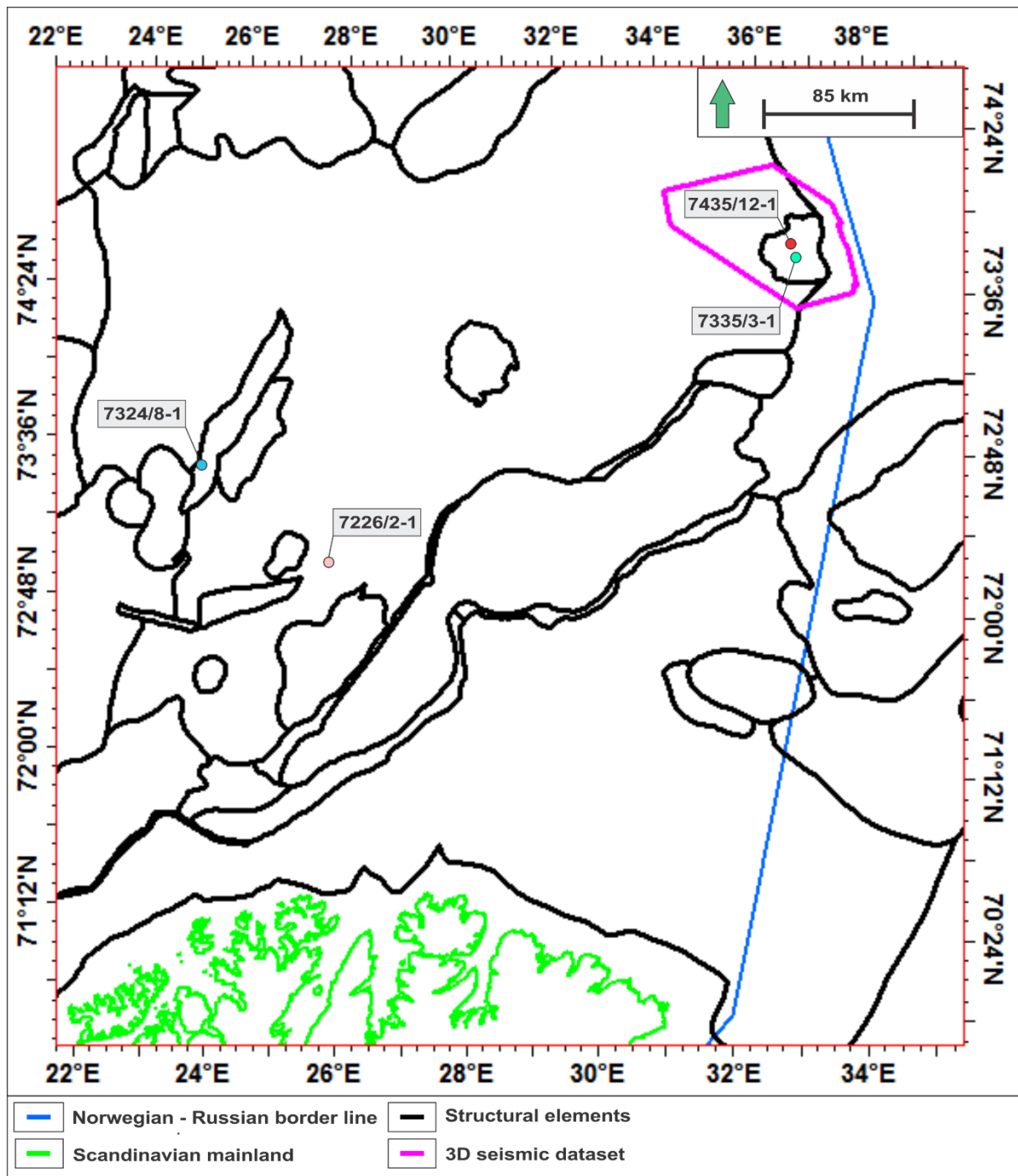


Figure 4.1: The location of the 3D seismic dataset and the utilised exploration wells. The structural elements are from NPD.no

## 4.2 Well data

Four exploration wells have been used for calibration of the stratigraphy (figure 4.1). Well 7435/12-1 was the primary calibration regarding the interpretation of seismic horizons to identify the exact position of subsurface horizons. Each seismic horizon was after that correlated with the gamma ray log from the wellbore. Additionally, velocity intervals for the prioritised seismic horizons were used to calculate both vertical and horizontal resolution.

Well 7335/3-1 was implemented to ensure deeper stratigraphic interpretation of the Kobbe, Klappmyss and Havert formations. The gas composition from well 7226/2-1 and 7324/8-1 (located ~319 km and ~364 km from the study area, respectively) was extracted from Løvaas (2016), where its chemical composition was used as an analogue to establish a gas hydrate stability model for the study area.

## 4.3 Phase and polarity

This thesis incorporates the polarity standards set by Sheriff (2002) in accordance with the SEG (Society of Exploration Geophysicists) convention. As displayed in figure 4.2, the phase and polarity of the survey reflect a normal polarity for a zero-phase pulse. For a zero-phase wavelet, the central peak is represented by a black peak.

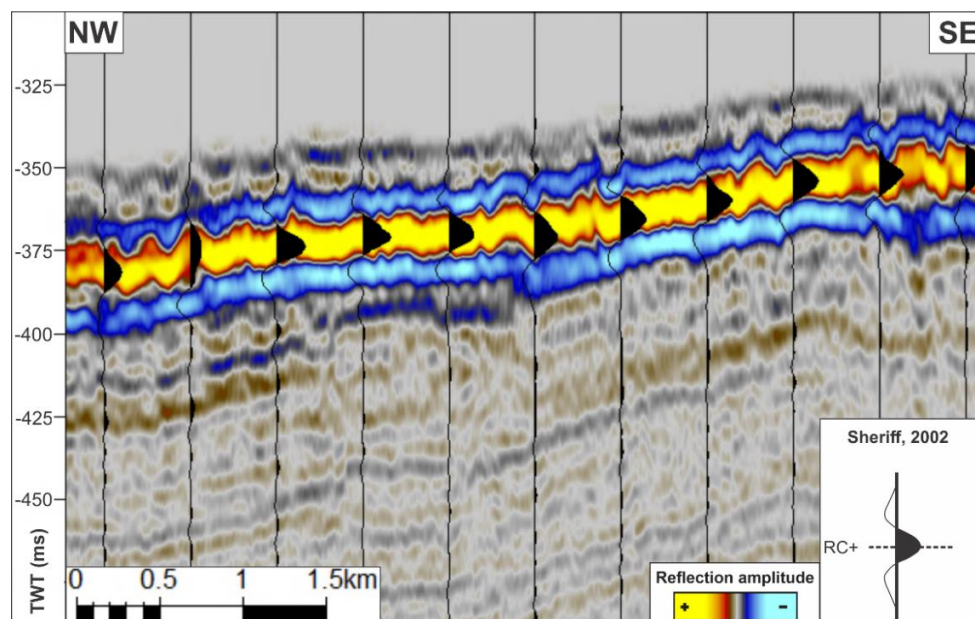


Figure 4.2: Seismic inline from the 3D dataset ST14005. The seafloor reflection displays a zero-phase wavelet of normal polarity according to the SEG convention set by Sheriff (2002).

## 4.4 Seismic resolution

After determining the polarity convention (figure 4.2), the vertical and horizontal resolution was calculated for the seismic 3D survey ST14005. The subsurface horizons of URU, top Hekkingen, top Fuglen and top Intra-Snadd were emphasised. The 3D cube was cropped in the Z-direction (TWT depth), dependent on the vertical extent of each horizon. Thereby, the frequency spectrum was concentrated along the individual horizons, where the dominant peak frequency was retrieved (figure 4.3). Only the most dominant frequencies for the individual horizons were used, where the higher frequency spectrum from 100 – 140 Hz was not considered. Besides, the calculations are only an approximation of the real resolution.

From the seismic well section, the interval velocity was extracted from the sonic log. By combining the specific horizons with the velocity log, an isolated seismic velocity interval can be estimated. The seismic wavelength was determined from equation 4.3 (Appendix 10.1). Equation 4.4 and 4.5 (Appendix 10.1) was after that used to calculate the vertical and horizontal resolution (Table 4.2). The vertical resolution from each interpreted horizon varies between 11.7 to 20.7 m, meaning that objects situated in the subsurface have to be larger than the estimated thickness to be visible.



**Table 4.2** – The estimated and calculated frequencies, wavelength, vertical- and horizontal resolution for the defined seismic horizons in the study area. Note that the horizontal resolution was calculated for unmigrated data.

Horizons	Velocity (m/s)	Peak frequency (Hz)	Wavelength (m) (v/f)	Vertical resolution (m)	Horizontal resolution (m) (unmigrated)	Depth TWT (s) from well 7435/12-1
URU	2106	45	46,8	11.7	94.10	0.35934
Hekkingen	2873	56.50	50.9	12.7	138.60	0.5257
Fuglen	2482	54.50	45.5	11.4	126.20	0.56365
Intra-Snadd	2923	35.40	82.6	20.7	225.85	0.84535

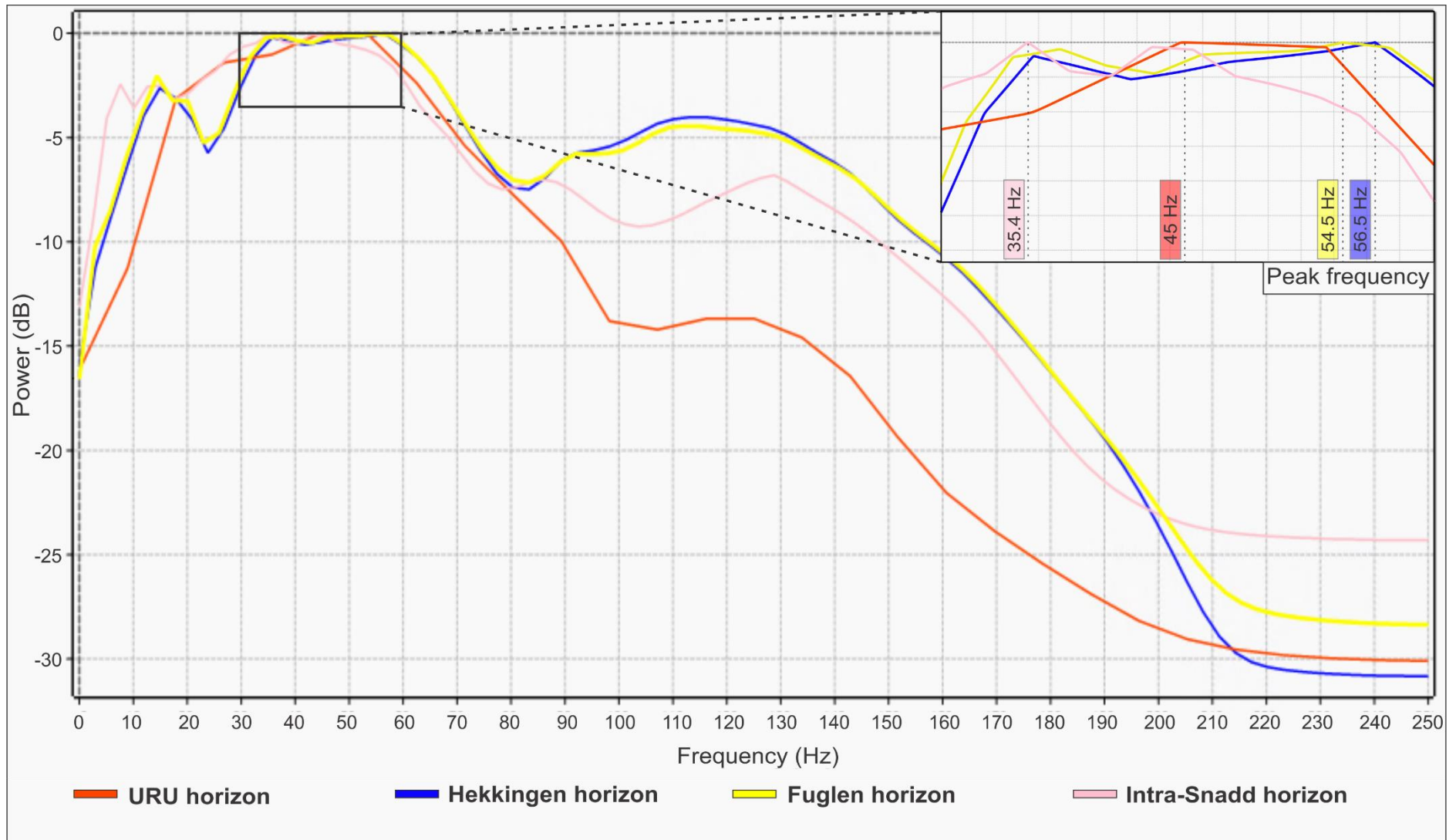


Figure 4.3: The frequency spectra for each horizon shown in Hertz. The frequency has been identified according to its peak for each horizon.



## **4.5 Methodology**

### **4.5.1 Software's**

Seismic investigation and interpretation were conducted in Schlumberger's seismic software, Petrel E&P Platform 2019. The software was used to interpret horizons, well-log analysis (gamma ray log and sonic log), generating surfaces, isochore mapping and surface attributes.

The software FM midwater from QPS emphasised processing of raw multibeam data. The processed water column data was analysed, where the most interesting seafloor features were extracted and implemented in QPS's Fledermaus software. The software Fledermaus was used to perform modelling of the potential gas flares. Every WCD line was investigated to ensure complete mapping regarding potential identification of gas flares in the study area (appendix 10.2). The software Dmagic and Global mapper were used as converter tools for exporting and importing water column data.

### **4.5.2 Seismic attributes**

The RMS (root mean square) amplitude attribute was used to produce several amplitude maps. This attribute calculates the square root of the sum of the squared amplitudes divided by the number of samples within a specific time window. Thus, the attribute emphasises variations in acoustic impedance over a selected sample window (Koson et al., 2014). In this thesis, the attribute was implemented to produce RMS surface maps along the Seafloor-, URU- and the Fuglen surface with specified search windows. Accordingly, the detection and visualisation of amplitude anomalies were conducted.

An isochore map was generated in two-way-travel time in Petrel to illustrate the vertical thickness of the glacial sediments between the URU and the seafloor horizon. The map displays lateral variations in time thickness between the two selected surfaces.

By using the edge method measurement, a variance attribute map was generated. The attribute measures trace-to-trace variability over a particular sample interval. Hence, it can visualise vertical discontinuities through a seismic dataset (Koson et al., 2014; Gogoi & Ghosh, 2017). The attribute was used to investigate the orientation and the prevalence of the fault planes in a 2D planar view.

### **4.5.3 Gas hydrate stability modelling**

A model for stable gas hydrates was generated by using a hydrate prediction program from Sloan (1998). This CSMHYD software is configured to calculate phase equilibria of hydrates according to available data. It calculates the pressure-temperature conditions for a phase transition between gas hydrates and free gas (Sloan, 1998). For identifying the equilibrium pressure, input parameters (bottom water temperature and gas composition) is required. The bottom water temperature ( $-1^{\circ}\text{C}$ ) was estimated from Ferré et al. (2020) (figure 3.12). Inclusively, the program can also evaluate pressure prediction at a given temperature with an inhibitor; in this case, a salinity of 3.5% was chosen.

The geothermal gradient (yellow line on figure 4.4) was calculated according to the bottom hole temperature ( $54^{\circ}\text{C}$ ) from well 7435/12-1 (NPD, 2017a), suggested to be  $\sim 0.035^{\circ}\text{C}/\text{m}$ . Well 7226/2-1 and 7324/8-1 were used as analogues to the study area, considering that the gas composition from well 7435/12-1 was not available. Thereby, the gas composition from both wells was extracted (Løvaas, 2016). In conjunction with all the parameters needed, a gas hydrate stability model was established for the study area (figure 4.4). Figure 4.4 comprises three phase boundaries, involving 100% methane (green curve), mixed gas hydrate phase boundary from well 7226/2-1 (blue curve) and a mixed gas hydrate phase boundary from well 7324/8-1 (red curve). Inclusively, the model displays at which depths BSRs may occur.

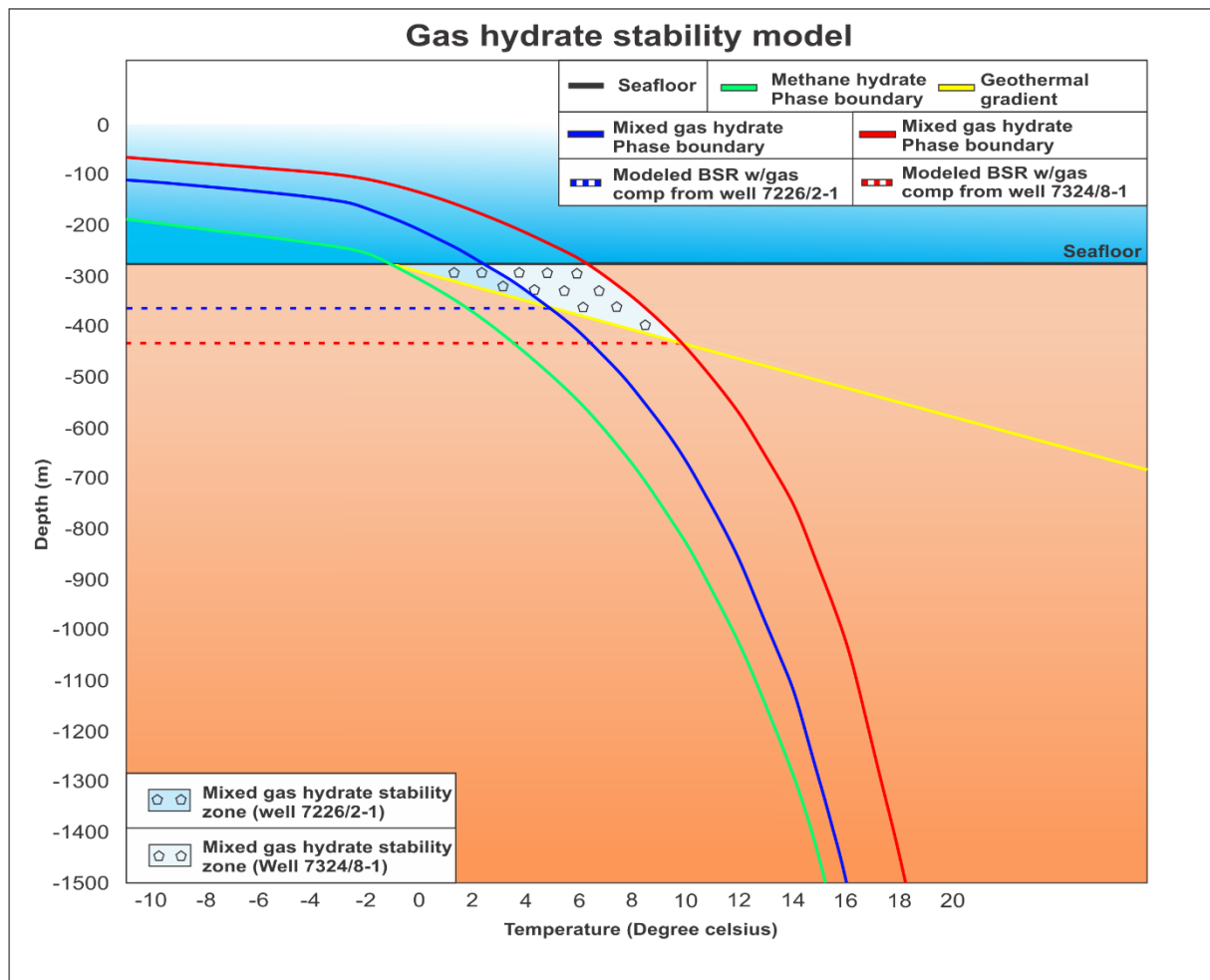


Figure 4.4: Illustration of the gas hydrate stability model. The model includes a 100% methane hydrate phase boundary (green curve), two mixed gas hydrate phase boundaries (blue and red curve), geothermal gradient (yellow curve), seafloor (black line), modelled BSR with a gas composition from well 7226/2-1 (Blue dotted line) and a modelled BSR with a gas composition from well 7324/8-1. The gas composition from well 7226/2-1 involves 98% C1, 1.2% C2, 0.31% C3, 0.04% iC4, 0.03% nC4, 0.02% C6 and 0.38% CO<sub>2</sub>. The gas composition from well 7324/8-1 involves 97.1% C1, 0.9% C2, 1.4% C3 and 1.84% CO<sub>2</sub>. Constructed based on Sloan (1998), Løvaas (2016), NPD (2017a) & Ferré et al. (2020).

#### **4.5.4 WCD acquisition**

The water column data was acquired by the Kongsberg Maritime service, conducted from January to June 2014 for the MAREANO program. During the acquisition, the Kongsberg EM 2040 multibeam echosounder system was used. The data was used to generate bathymetric seafloor models and investigate potential gas flares in the Haapet Dome area. Figure 1.1 shows the data coverage of the acquired water column data.

#### **4.5.5 Concepts of WCI**

In this study, water column imaging (WCI) emphasises the identification of continuous rising bubble streams through the water column. As mentioned in chapter 3.6, these bubble streams (figure 4.5) can be detected by their oblique to vertical pattern, strong acoustic change in impedance and their connection to the seafloor.

Figure 4.5 displays a raw swath image consisting of two visible acoustic flares. Beyond the minimum slant range, occurrence of side-lobe artefacts are predominant, resulting in difficulties in determining bubble streams. Hence, all observations were performed inside the minimum slant range to avoid acoustic artefacts. Artificial errors may still appear inside the minimum slant range (figure 4.6), which were mentioned in chapter 3.6.

When the water column is insonified (exposed by sonar imaging), the size of the gas bubbles needs to be larger than the resonance frequency ( $> 1$  mm in diameter) to be recognized. Figure 4.7 illustrate how a single gas bubble is recognised in the water column data. The most common gas bubble size is between 1 mm to 12 mm (Veloso et al., 2015).

Limitations regarding detection of possible gas flares vary according to the performance parameters of the multibeam echosounder, beam angle and the depth of the water column. Thus, minor miscalculations will affect the original shape and size of a possible gas flare, which may result in misinterpretation. As mentioned in chapter 3.6, fish shoals and microorganisms may develop similar hydroacoustic signatures, which could interfere with rising gas bubbles. The backscatter strength and morphological characteristics of gas bubbles can be used to prevent misinterpretations. (Veloso et al., 2015; Zhao et al., 2017).

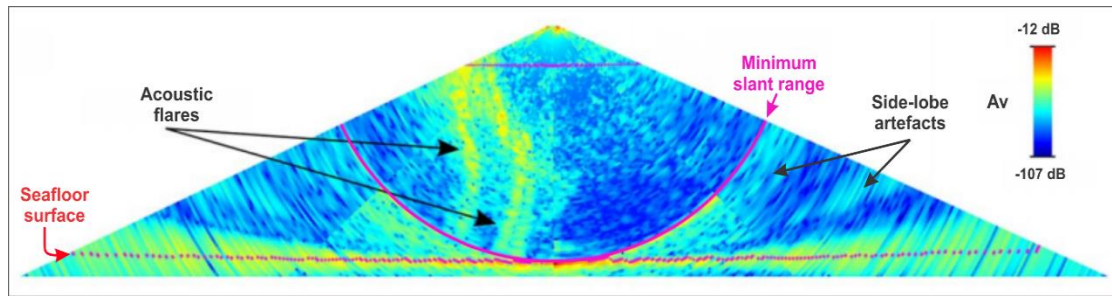


Figure 4.5: Raw swath water column image displaying the observational acoustic features inside and beyond the minimum slant range. Modified from Urban et al. (2017).

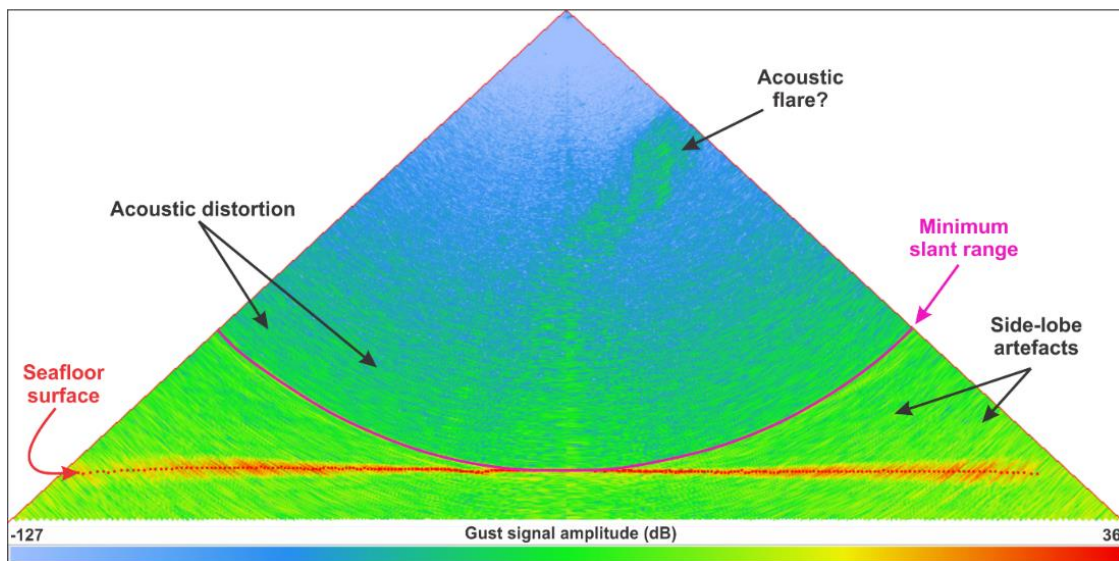


Figure 4.6: Processed water column image from WCD line 4842, illustrating the same acoustic features as the previous figure, including Acoustic distortion inside the minimum slant range. Note that one fan stack was used to enhance the anomalies. Data from Mareano (2014).

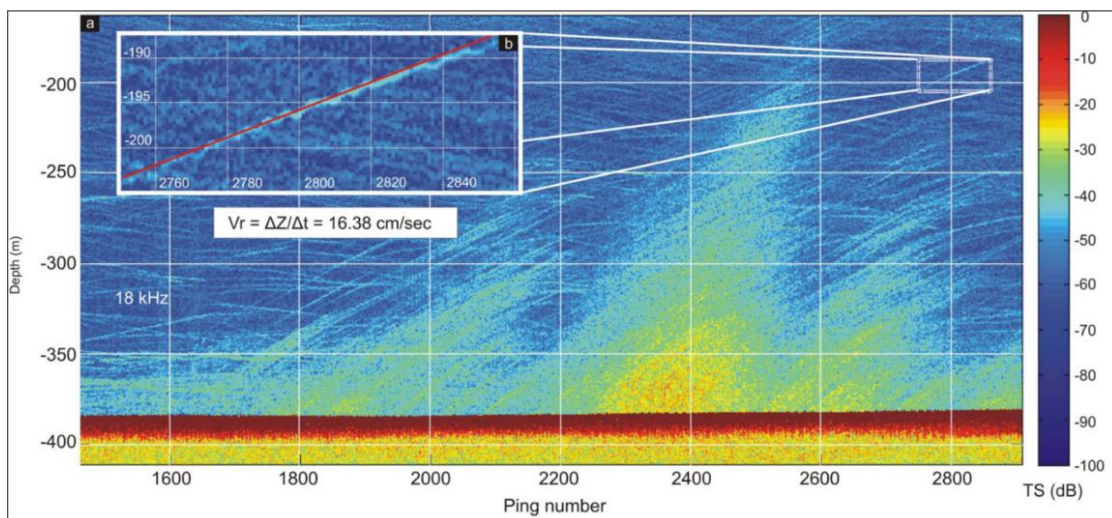


Figure 4.7: (A) Echogram displaying the backscatter of single gas bubbles captured with a slow sampling rate. (B) Illustrates an enlarged version of a single gas bubble and its hydroacoustic signature. Modified from Veloso et al. (2015).

# 5 Results

The following chapter includes the results of the seismic interpretations presented in chronological order, starting with an overview of the interpreted surfaces in the study area. After that, an assessment of fault interpretations in connection with shallow seismic anomalies. Subsequently, the potential relation between shallow seismic anomalies and potential gas flares will be presented.

## 5.1 Stratigraphic overview

In this chapter, the mapping of five main horizons down to 1250 ms (TWT) will be the focus (figure 5.2 & 5.3). Depth of maximum 1250 ms (TWT) was chosen considering that the thesis emphasises mapping of shallow seismic anomalies. The five main horizons are the seafloor, URU, top Hekkingen horizon, top Fuglen horizon and top Intra-Snadd horizon (summarised in figure 5.1). Local deposits of Quaternary sediments, which overlies the Cretaceous unit, can be observed across the study area. The interpreted horizons (figure 5.3A) was calibrated based on the well-log information from well 7435/12-1.









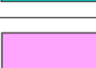

Stratigraphic legend - 3D seismic survey					
Period	Age	Group	Unit color	Unit boundary color	
Cenozoic	Quaternary	Adventdal		 Seafloor horizon	
				 URU horizon	
Mesozoic	Cretaceous			Cretaceous unit	
			Jurassic		 Top Hekkingen horizon
					 Top Fuglen horizon
Triassic			 Top Intra-Snadd horizon		
		Kapp Toscana			

Figure 5.1: Schematic overview displaying colour codes and names for each specific seismic unit and unit boundary in the study area.



### Seismic 3D inline 4120

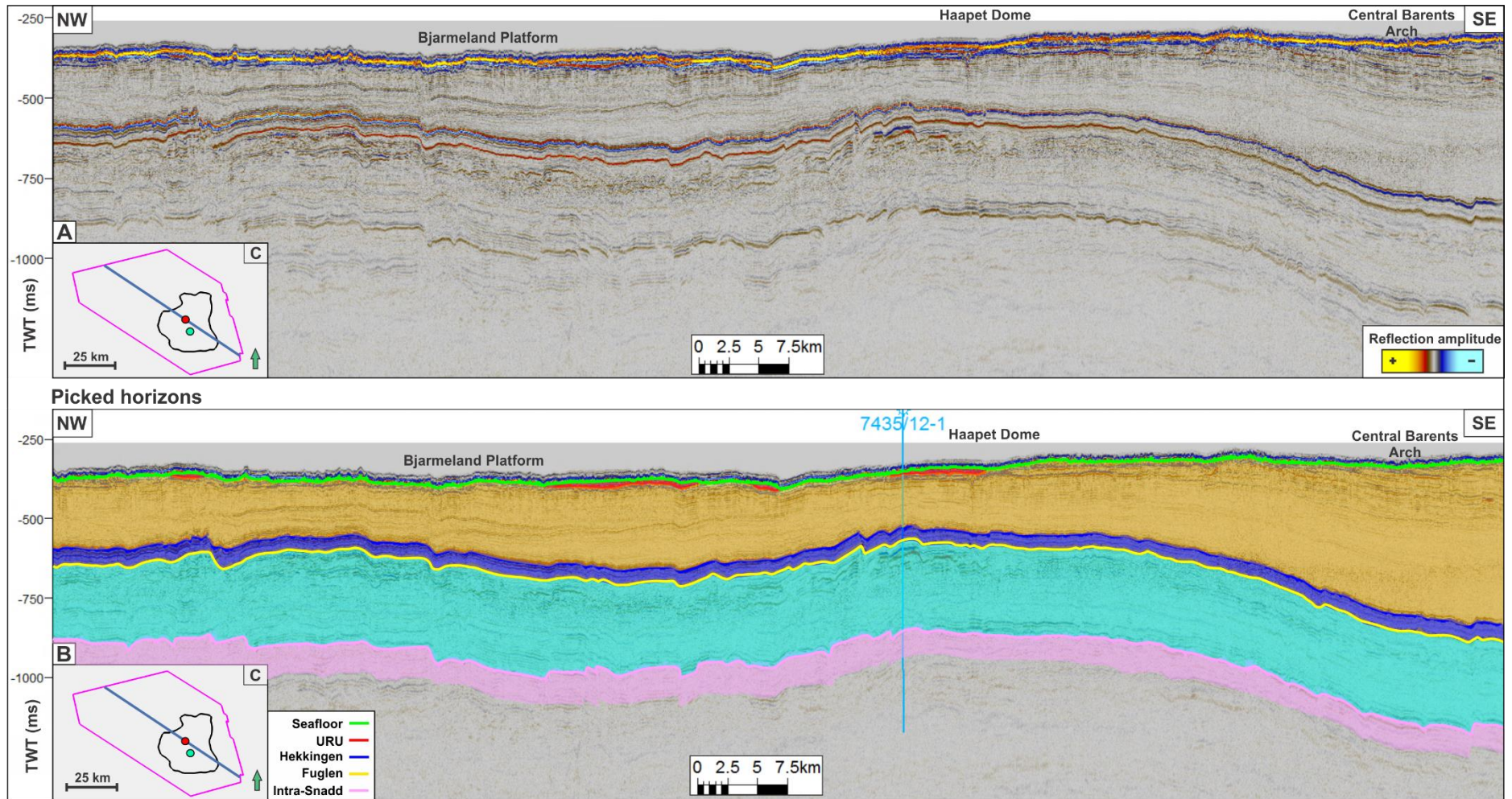


Figure 5.2: Seismic inline 4120, displaying (A) the uninterpreted seismic inline and (B) interpreted seismic sequence boundaries and seismic sequences. (C) Indicates the position of the inline, in addition to well 7435/12-1 (red) and 7335/3-1 (green). The blue vertical line in (C) marks the borehole for well 7435/12-1. Note that the light-blue unit colour comprises the Fuglen, Stø, Nordmela, Tubåen and upper parts of the Snadd formations.



Seismic 3D xline 7900

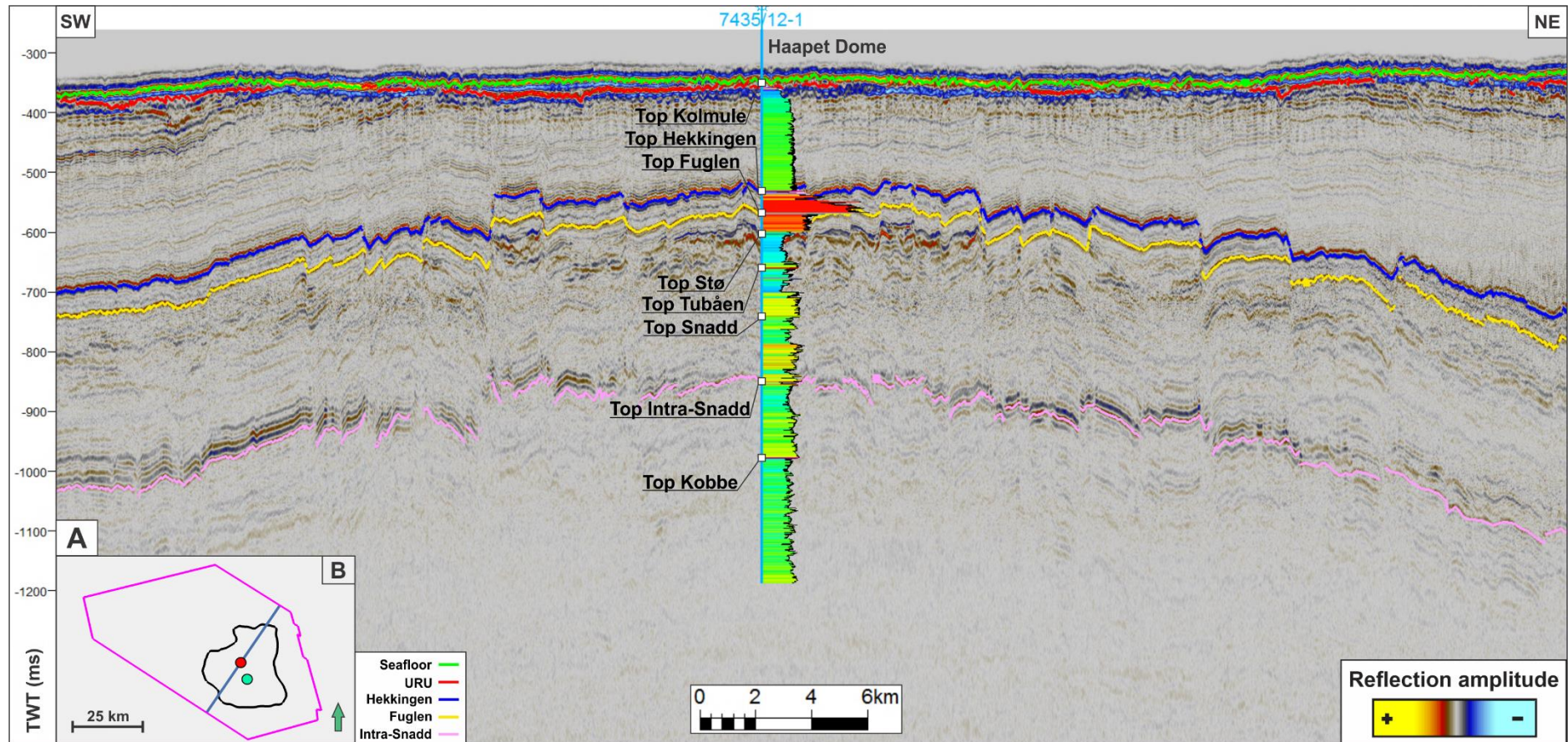


Figure 5.3: (A) Seismic xline 7900, illustrating the selected horizons. Seismic-to-well tie was used to ensure correct interpretation of horizons by utilising the formation tops from the borehole. Note that the vertical blue line marks the well 7435/12-1, which displays the gamma ray log for each stratigraphic unit between 351 to 1169 ms (TWT). (B) Indicates the position of the selected xline and the well 7435/12-1 (red) and 7335/3-1 (green).



## 5.2 Interpreted horizons and isochore maps

The top Intra-Snadd horizon (figure 5.2B & 5.3A) marks the deepest interpreted surface in this study. The horizon is presented by a moderate to high amplitude reflection, with an overall continuity throughout the study area. On the 3D seismic dataset, the horizon was interpreted on a peak reflection. Two closely spaced reflections were observed in the top Intra-Snadd formation, where the lower reflection was selected for interpretation, considering that it represents a stronger and more consistent amplitude reflection than the above reflector.

The time structure map for the top Intra-Snadd horizon is shown in figure 5.4A, which indicated two structural highs situated in the northwest and the southeast (the Haapet Dome). The shallowest depth is estimated to be of 750 ms (TWT) in the Haapet Dome area. The deeper parts are situated between the structural highs and in the most southeastern parts of the study area.

The top Fuglen horizon (figure 5.2B & 5.3A) has a continuous character in the study area, which is represented by a high amplitude reflection, interpreted on a peak reflection. The time structure map for the top Fuglen horizon (figure 5.4B) is represented by two structural highs, with a deeper area in between. The most southeastern parts illustrated the deepest areas, reaching depths of 900 ms (TWT).

The top Hekkingen horizon (figure 5.2B & 5.3A) is represented by a strong amplitude reflection, interpreted on a trough. The seismic reflection of top Hekkingen has a continuous character in the study area. Figure 5.4C has a similar surface characteristic as of the top Fuglen surface, where deeper depths are located in the most southeastern areas, including a minor depression between the structural highs.

The seafloor horizon (figure 5.2B & 5.3A) is also represented by a continuous high amplitude reflection, interpreted on a peak. The time structure map of the seafloor horizon is displayed in figure 5.4D. The surface is represented by shallower elevation depths (~300 ms TWT) on the Haapet Dome area and across the central Barents arch. In the western parts of the study area, smaller highs are observed with dimensions ranging from 1000 to 5000 m in length, with a relief ranging from 25 to 45 ms (TWT).

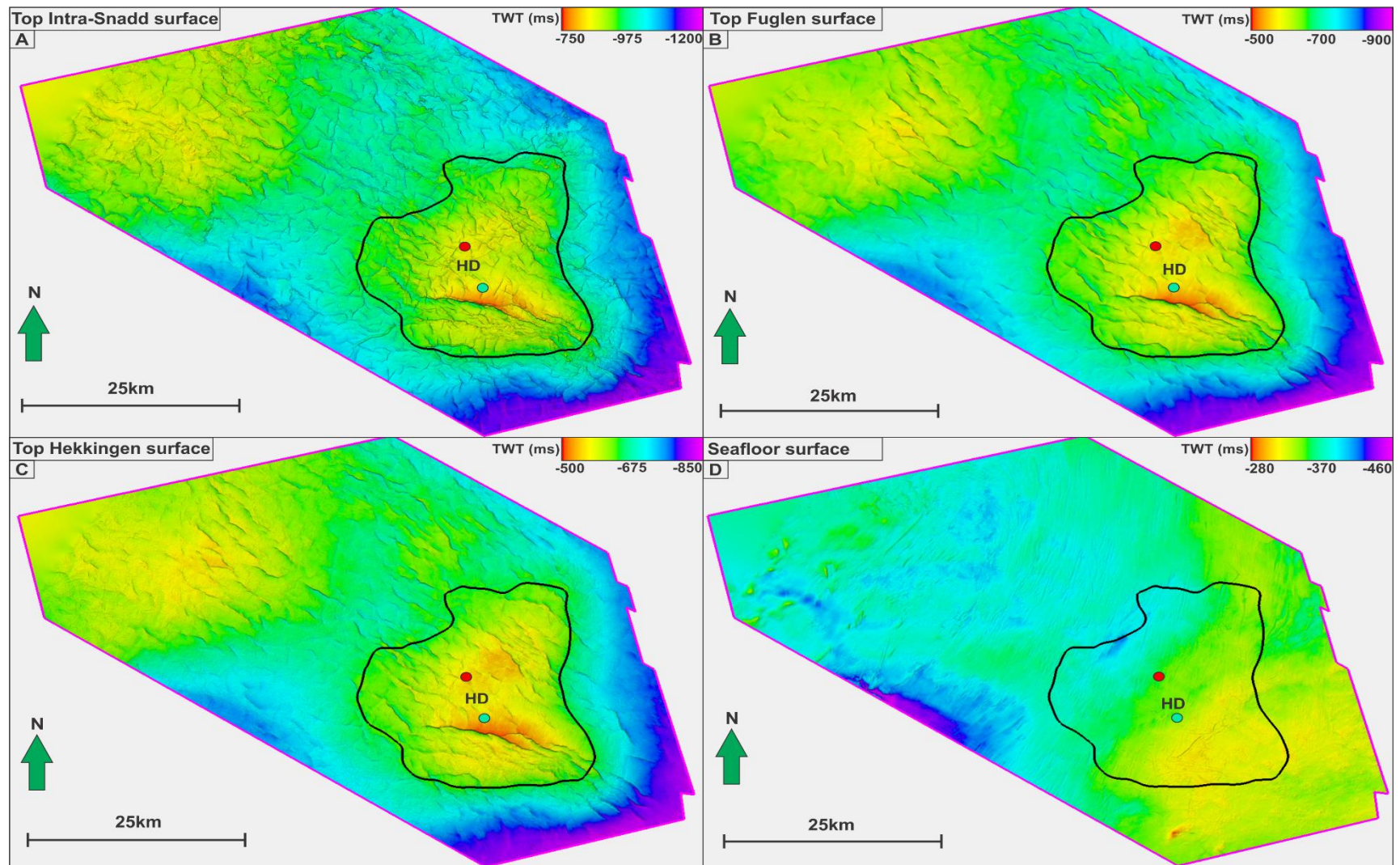


Figure 5.4: Four of the five interpreted horizons within the ST14005 3D seismic survey (Vertical exaggeration of 5). The individual surfaces represent elevation depths in ms (TWT) for (A) top Intra-Snadd horizon, (B) top Fuglen horizon, (C) top Hekkingen horizon and (D) the seafloor horizon. The black polygon displays the Haapet Dome structural element. HD = Haapet Dome. Note that the red and green circles indicate the position of well 7435/12-1 and 7335/3-1, respectively.

The Upper Regional Unconformity (URU) is represented by a discontinuous but high amplitude reflection, interpreted on a peak (figure 5.2B). The URU is primarily present in the central parts of the study area (figure 5.5). The unconformity reaches a depth of ~460 ms (TWT) in the southwestern parts. Shallower parts are situated at the structural highs, ranging from 390 to 320 ms (TWT) (figure 5.5). The URU seems to have terminated at the structural highs. Besides, the terminated URU horizon marks the area where the URU- and the seafloor horizon cannot be distinguished from another. The surface is relatively flat northeast of the Haapet Dome, compared to the eastern and southwestern parts.

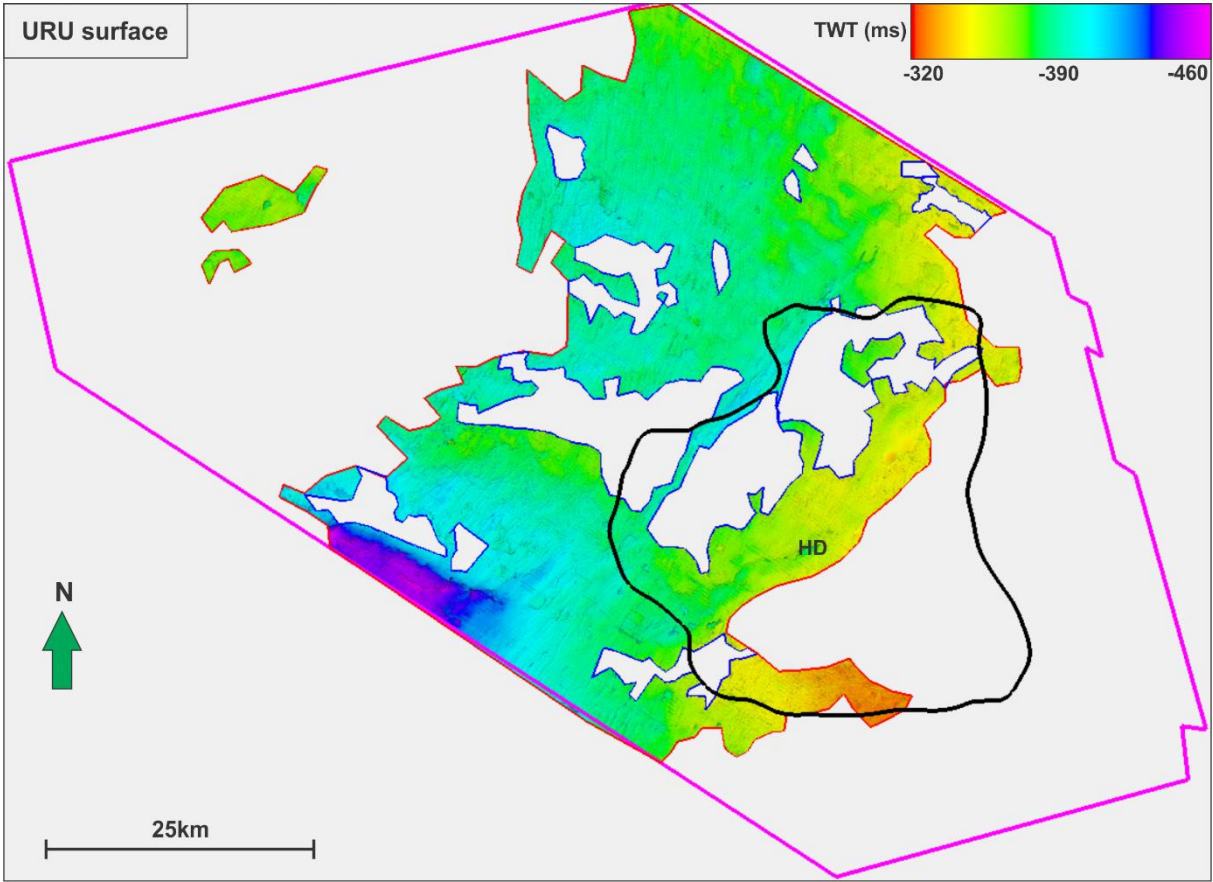


Figure 5.5: Time-structure map of the URU surface map. The black polygon shows the Haapet Dome structural elements. An outer polygon (red) and inner polygon (blue) was implemented to illustrate the distribution of the glaciogenic sediments based on the limits of vertical resolution. HD = Haapet Dome.

The thickness of the Quaternary sediments varies from zero to ~42 ms (TWT) (figure 5.6). The presence of Quaternary sediments is primarily situated in the central parts of the study area. Quaternary deposits can also be observed above the structural highs, both located in the northwestern parts and on the Haapet Dome.

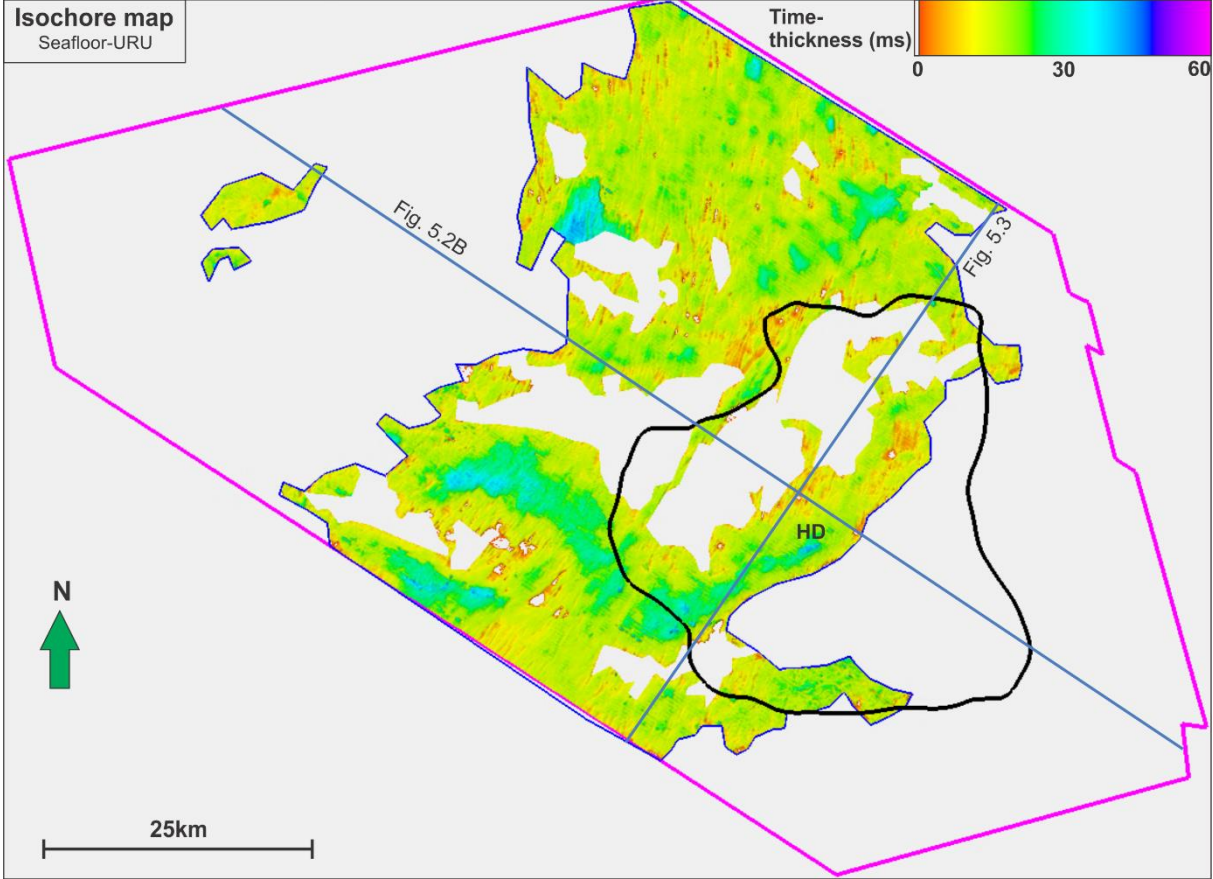


Figure 5.6: Isochore map showing the vertical time-thickness of the Quaternary deposits (vertical exaggeration of 7.5). The black lines indicate the Haapet Dome (HD). The two blue lines represent the cross-section of figure 5.2B & 5.3. An outer polygon (blue) was implemented to illustrate the distribution of the glacial sediments based on the limits of vertical resolution. Note that the opacity was manipulated to cancel out thickness values of 0 ms (TWT).



### 5.3 Faults

The Haapet Dome region comprises faulted strata that predominantly extends from the lower parts of the Intra-Snadd formation (might extend deeper) and terminates below the seafloor reflection.

The fault system is represented by similar fracture patterns in the Fuglen and Hekkingen formations (figure 5.4B & 5.4C). The top Intra-Snadd surface (figure 5.4A) indicates a fracture pattern that is cross-cutting one another and generally appears more chaotic. The seafloor surface remains none-faulted (figure 5.4D).

A variance map was generated to illustrate the distribution of vertical variations from the Hekkingen Formation (figure 5.7). During a particular sample interval, high variance coefficients could develop during encounters of discontinues features, which might suggest the presence of faults (Gogoi & Ghosh, 2017). Within the study area, the majority of the faults are associated with structural highs, while the area in between appears to be less influenced.

In general, the faults indicated a dominant dip direction towards both northeast and southwest (figure 5.8, 5.9, 5.10 & 5.11). The lateral changes in acoustic impedance along the top Hekkingen surface indicates that both shallow- and deep-seated faults have a predominant northwest-southeast strike orientation (figure 5.7).

Along the southwest-northeast oriented cross-sections, the horizontal spacing between each fault was measured to vary from 0.4 to 8 km. Inclusively, the vertical rock displacement (fault throw) were measured. The most significant fault throw is indicated in figure 5.8B, where the maximum vertical displacement of rocks (~185 ms (TWT)) are occurring between the top Fuglen and the top Intra-Snadd horizon.

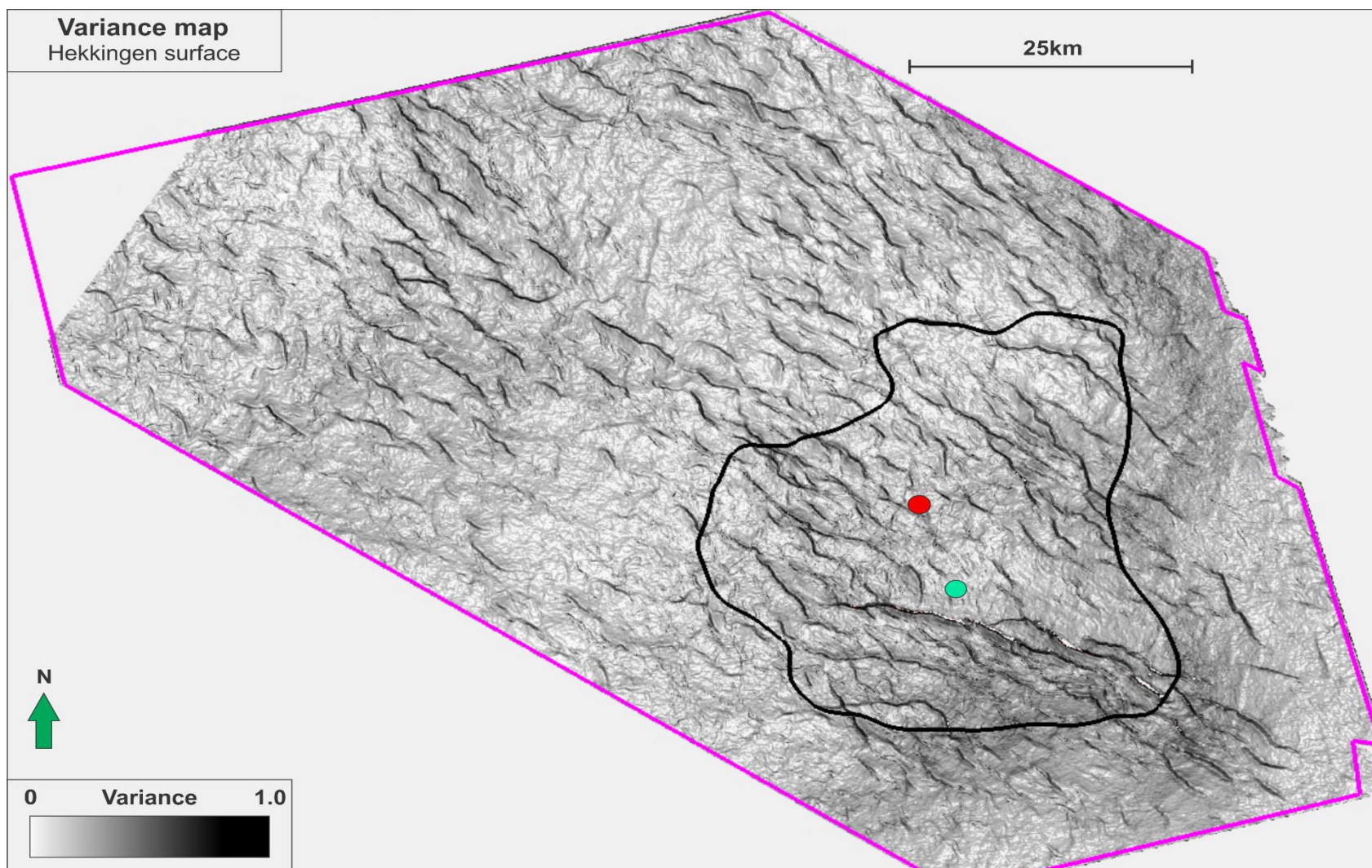


Figure 5.7: A variance surface extracted from the top Hekkingen surface with a vertical exaggeration of 20. The variance map displays the major fault structures situated in the study area. The black polygon represents the Haapet Dome, whereas the purple polygon indicates the limits of the survey area ST14005. The majority of the faults shows a northwest-southeast strike orientation. Note that the red and green circles indicate the position of well 7435/12-1 and 7335/3-1, respectively.



Seismic 3D xline 8370

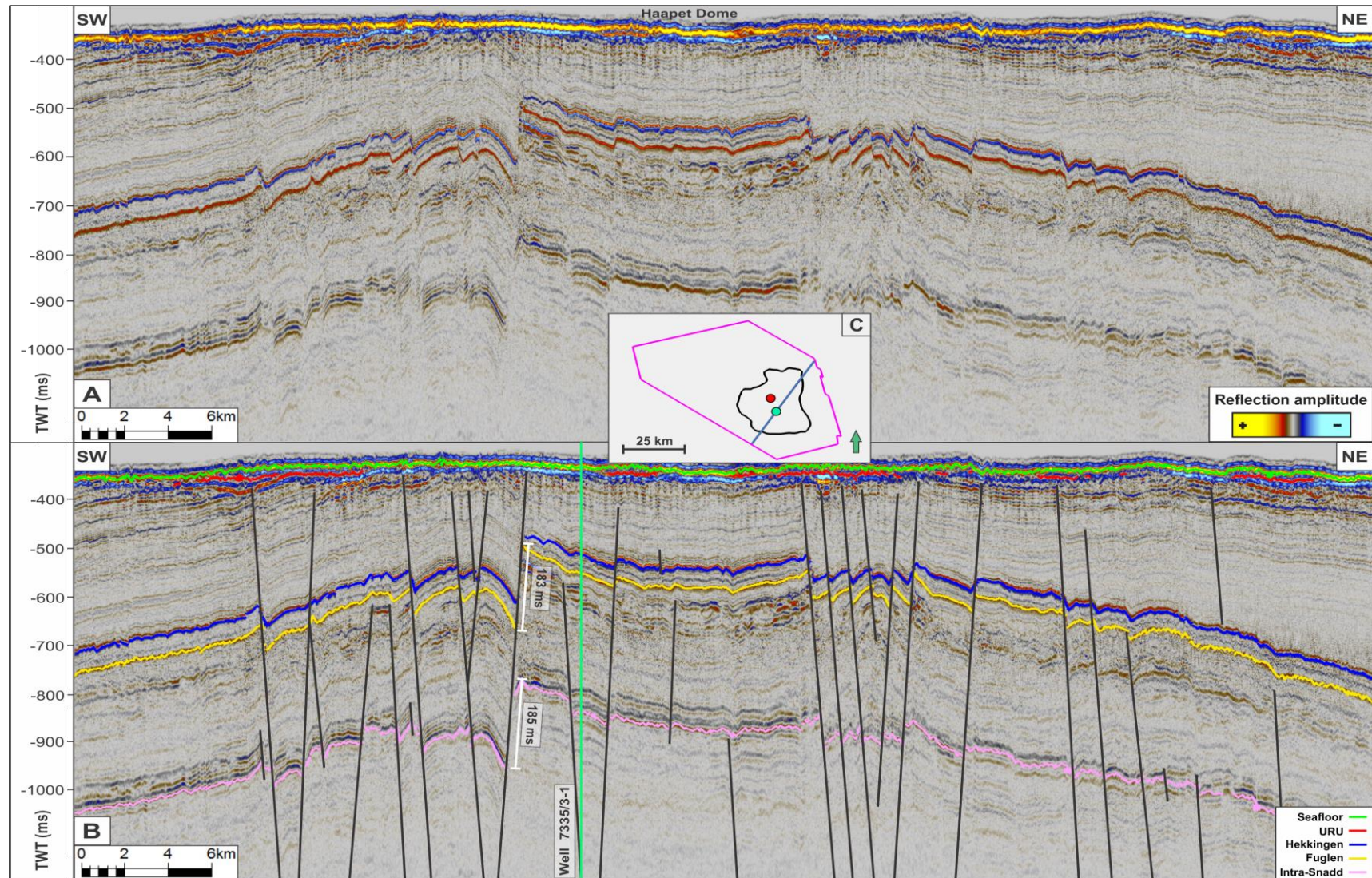


Figure 5.8: Seismic section showing (A) the uninterpreted seismic xline, (B) the interpreted horizons and faults with well 7335/3-1 (vertical green line). Notice that the measurements for the largest fault throw were indicated. (C) The position of the seismic section and location of well 7435/12-1 (red) and 7335/3-1 (green).



Seismic 3D xline 6200

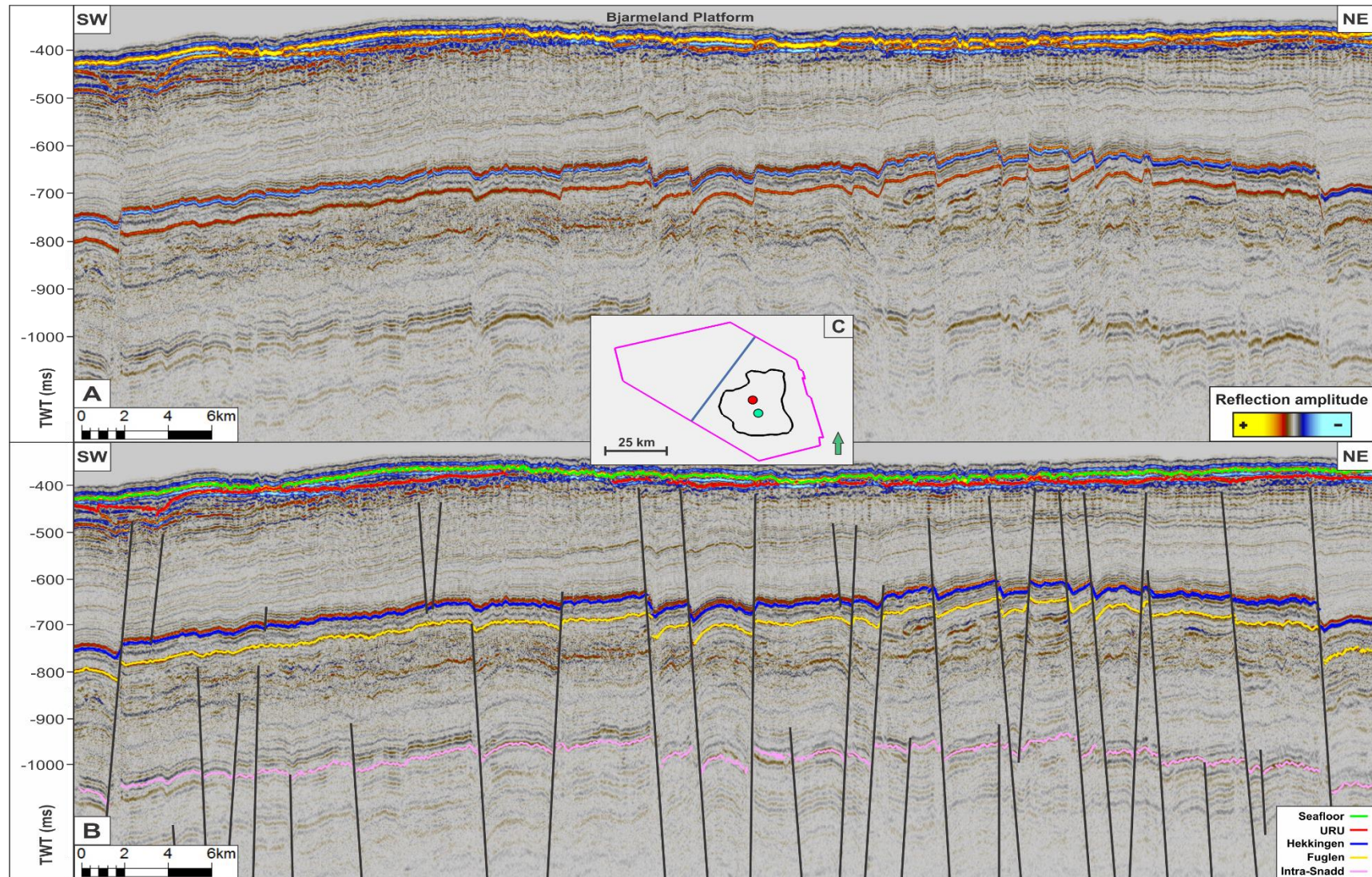


Figure 5.9: Seismic section showing (A) the uninterpreted seismic xline, (B) the interpreted horizons and faults, including (C) the position of the seismic section and location of well 7435/12-1 (red) and 7335/3-1 (green).



Seismic 3D xline 3800

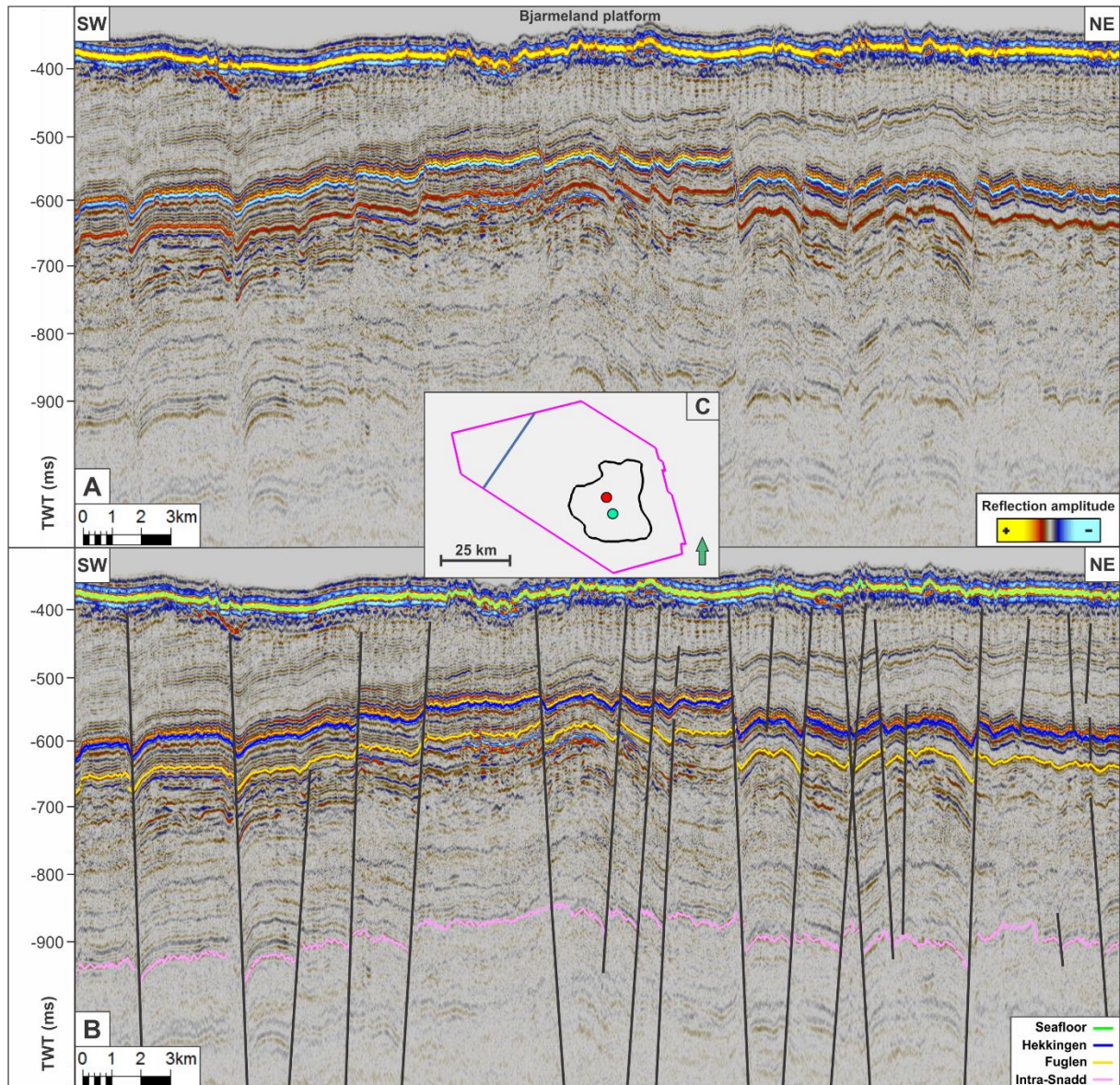


Figure 5.10: Seismic section representing (A) the uninterpreted seismic xline, (B) the interpreted horizons and faults, including (C) the position of the seismic section and location of well 7435/12-1 (red) and 7335/3-1 (green).



Seismic 3D inline 4080

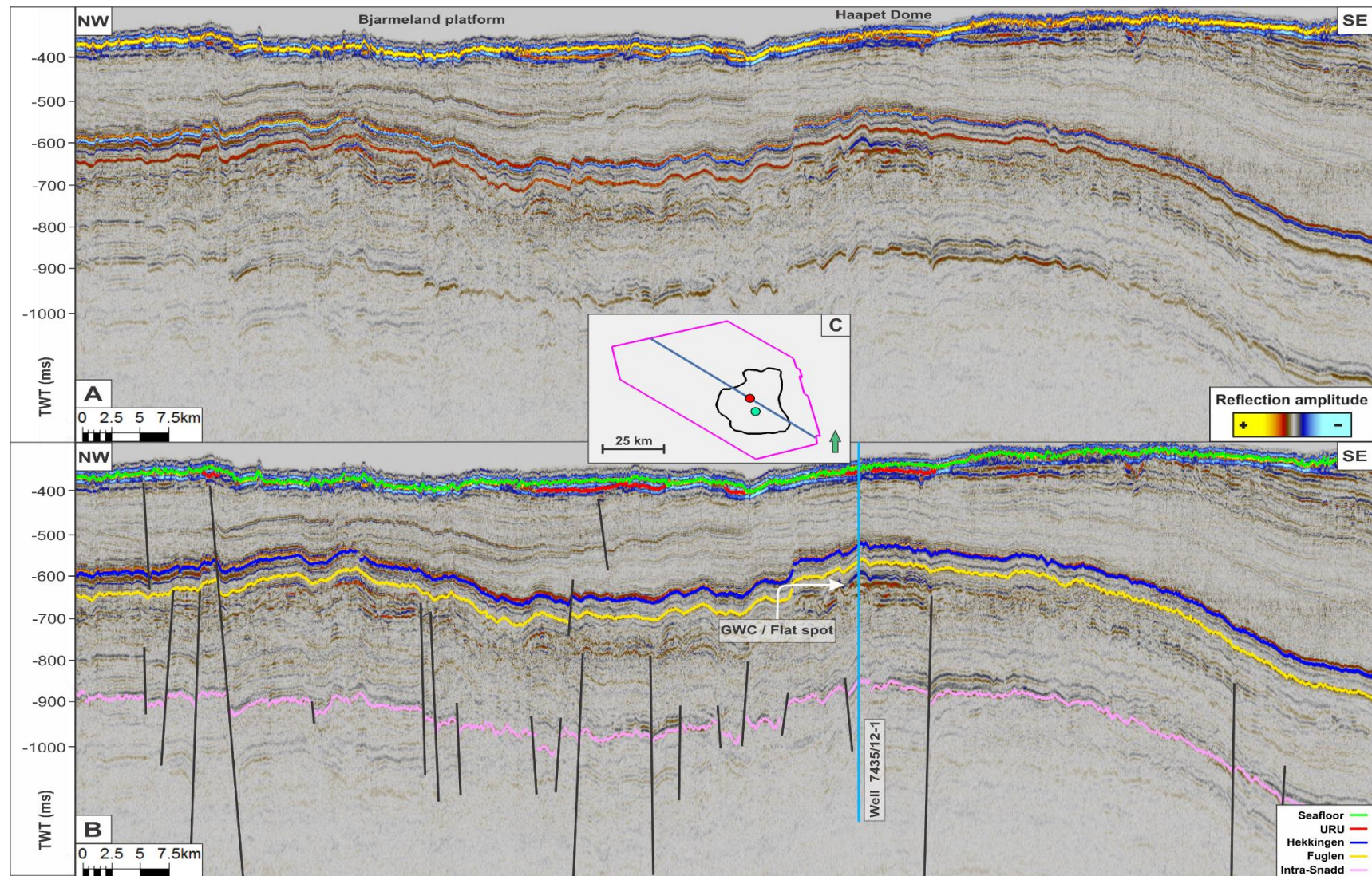


Figure 5.11: Seismic section showing (A) the uninterpreted seismic inline, (B) the interpreted horizons and faults, including (C) the position of the seismic section and location of well 7435/12-1 (red) and 7335/3-1 (green). Note that the flat spot was tested to represent the GWC in well 7435/12-1.



Specified composite line

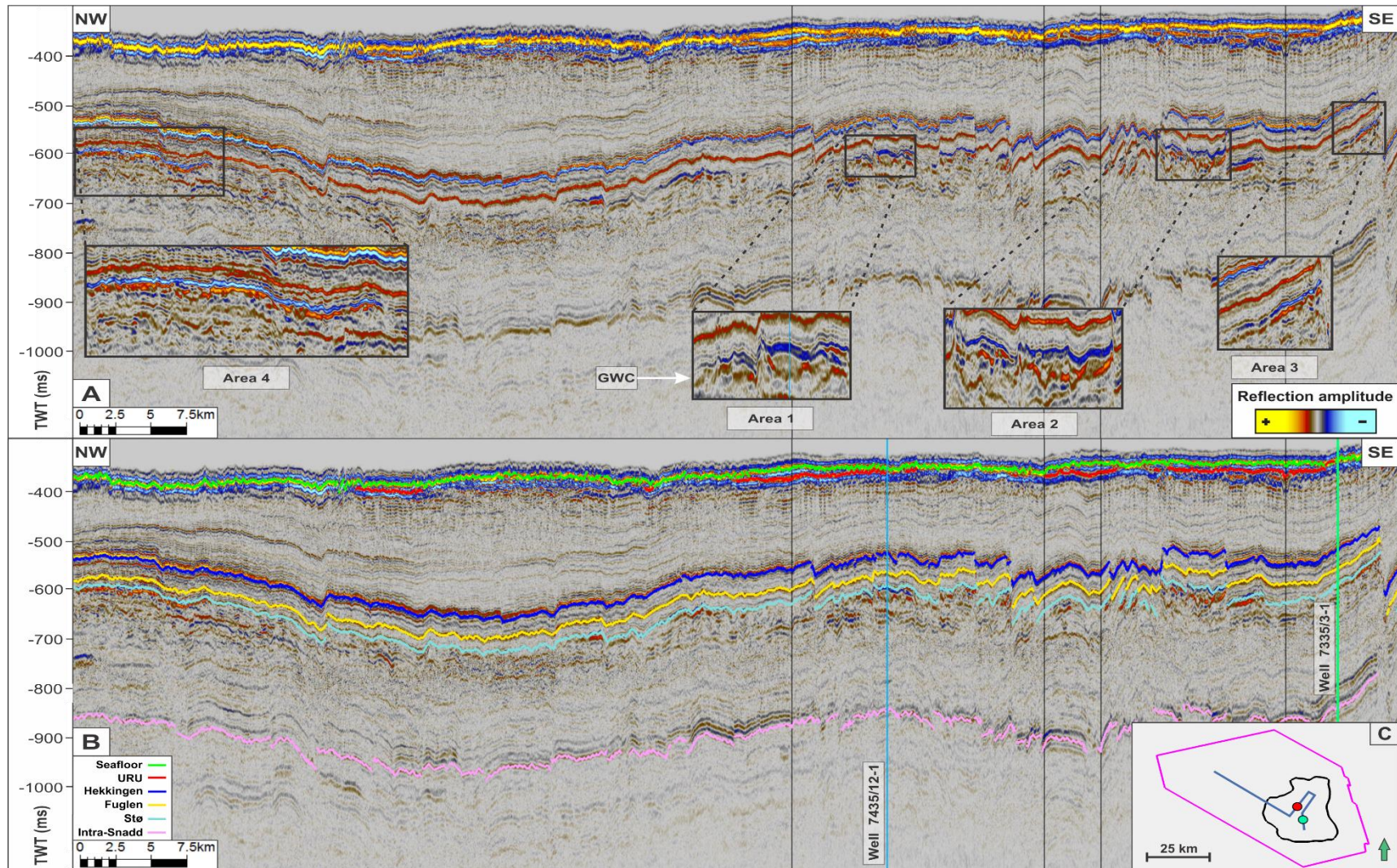


Figure 5.12: (A) Uninterpreted seismic composite profile shown in a northwest-southeast orientation, illustrating four zones with shallow amplitude anomalies in the Stø and Nordmela formations. (B) Seismic-to-well tie was used to ensure correct interpretation of the top Stø horizon (light blue colour) by using the formation tops from the borehole. Note that the vertical blue and green line marks the well 7435/12-1 and 7335/3-1. (C) Displays the location of the composite line.

## 5.4 Shallow amplitude anomalies and leakage zones

In this study, the seismic amplitude anomalies are defined according to the following criteria; (1) occurrence of increased amplitude, (2) reflection discontinuity, and (3) polarity reversal in comparison with the seafloor horizon (e.g. a decrease of AI). As explained in chapter 3.4, if these criteria's are present, the identified amplitude anomalies could be associated with potential hydrocarbon-saturated sediments.

As the Stø Formation comprised poor data quality across the study area, a single line was interpreted to illustrate the elevation level of the top Stø horizon, relative to amplitude anomalies in figure 5.12B. Given that the Stø and Nordmela formations are situated roughly on top of each other (~2 ms (TWT) separating them), both of them will be represented as the Stø Formation onwards in this thesis. The strongest amplitude anomalies were observed in the Stø Formation. An extracted composite line (figure 5.12A) was implemented to localise amplitude anomalies beneath the seafloor/URU horizon relative to amplitude anomalies within the Stø Formation. Thus, four areas of amplitude anomalies were further investigated (figure 5.12A).

The identified amplitude anomalies in the Stø Formation were defined to an RMS response above 1300 (figure 5.13), where most of the anomalies are situated in the northwestern parts and inside the Haapet Dome area. Each seismic amplitude response within the Stø Formation is presented with a search window of 30 ms (TWT). There seem to be a relation between faults (figure 5.8A) and zones of high amplitude responses (figure 5.13). A majority of the amplitude anomalies are situated on the flanks of a fault.

Figure 5.14 illustrates an RMS amplitude surface that emphasises the detection of amplitude anomalies beneath the seafloor and URU horizon. For this RMS amplitude surface, the amplitude anomalies were defined to RMS responses above 4500. Amplitude anomalies can be observed in several areas beneath the seafloor and the URU surface (figure 5.14). By investigating the seafloor horizon on figure 5.15A, strong discontinues amplitude brightening is observed.

According to NPD (2017d), well 7435/12-1 indicated that the Snadd Formation has potential for gas accumulations. Along the interpreted top Intra-Snadd horizon, the presence of amplitude anomalies are occurring (figure 5.16A, 5.17A & 5.18A). However, the thesis emphasises the detection of shallow amplitude anomalies as representatives of potential gas accumulations. Both Exploration wells (well 7435/12-1 and well 7335/3-1) confirmed the absence of hydrocarbons in the Snadd Formation, including poor reservoir quality. Hence, no further investigation of the amplitude anomalies along the top Intra-Snadd horizon was conducted. Inclusively, dry gas was observed in the Kobbe Formation from NPD (2017d), but no amplitude anomalies were observed in the seismic section.

As explained in chapter 3.1.1, tuning effects might result in constructive interfering where seismic reflections are progressively interfering and eventually producing a single seismic reflection. Thereby, an increase in amplitude response will occur (figure 5.15A).



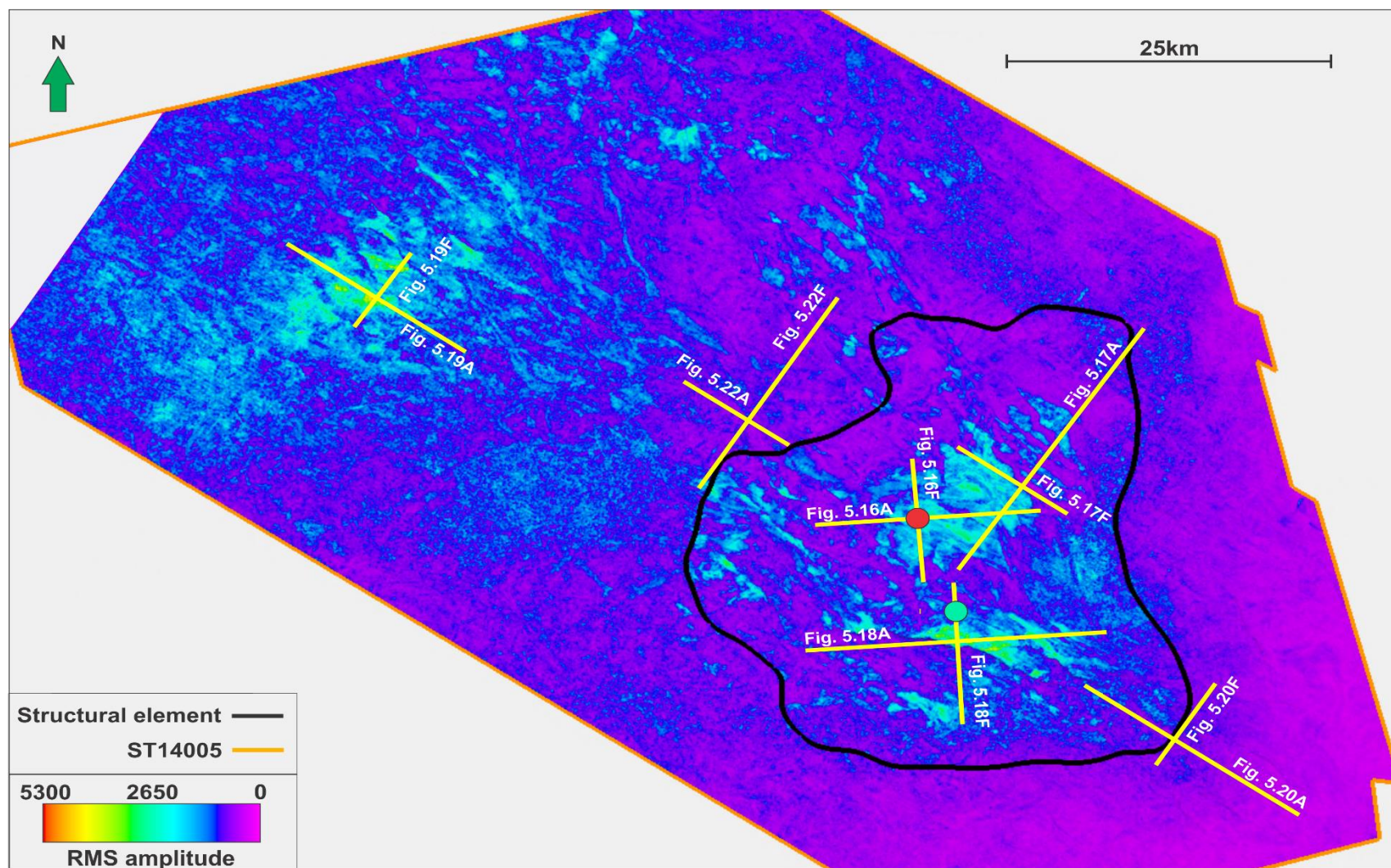


Figure 5.13: 2D planar view of the seismic amplitude anomalies and their spatial distribution shown on an RMS amplitude surface across the Stø Formation. The surface was extracted 20 ms (TWT) below the top Fuglen horizon, with a search window of 30 ms (TWT). The yellow lines illustrate the individual seismic profiles. Note that the red and green circles indicate the position of well 7435/12-1 and 7335/3-1, respectively.



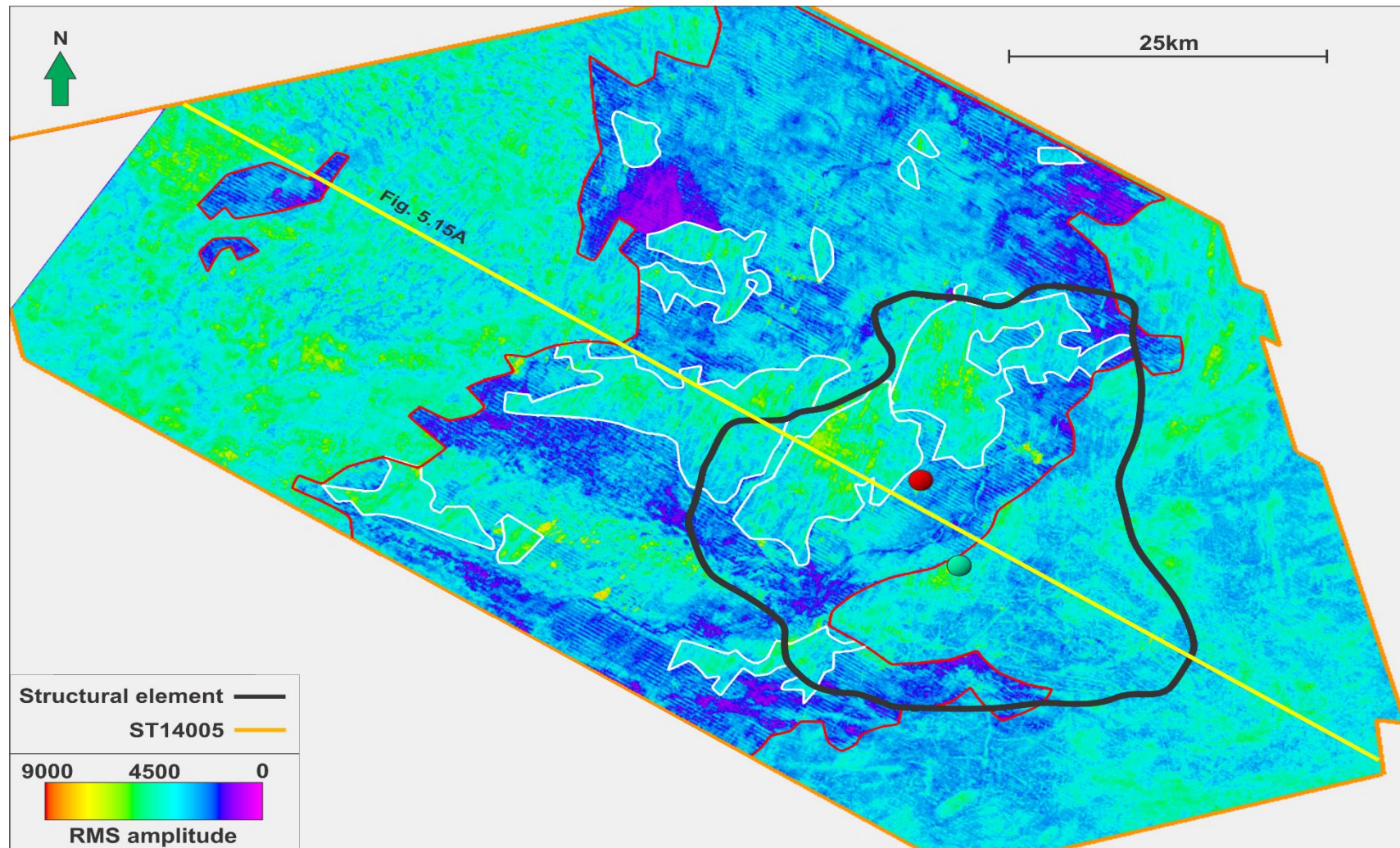


Figure 5.14: 2D planar view of the seismic amplitude anomalies and their spatial distribution shown on an RMS amplitude surface located beneath the seafloor (Outside red polygon and inside white polygons) and the URU (Inside red polygon). As comparison to figure 5.5 and 5.6, Quaternary units are mapped below the seabed in the central parts of the study area. Both the seafloor and the URU surface is represented with a search window of 50 ms (TWT). Note that the red and green circles indicate the position of well 7435/12-1 and 7335/3-1, respectively. The yellow line illustrates the orientation of the seismic profile in figure 5.15A.



Seismic 3D inline 4300

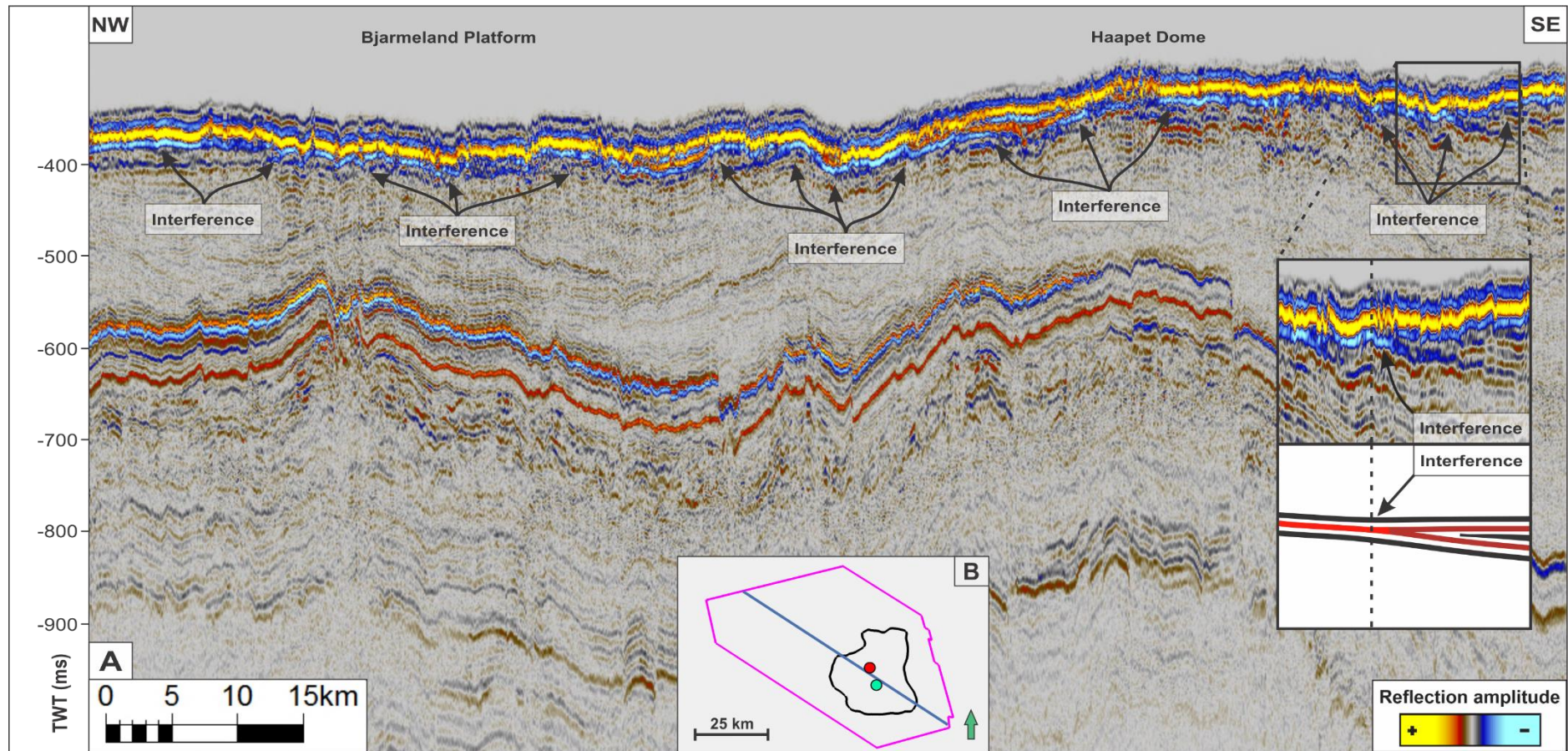


Figure 5.15: (A) Uninterpreted seismic inline shown in a northwest-southeast orientation, illustrating constructive interference of seismic reflections. The most southeastern example illustrates two seismic reflections that pinch out towards northwest and produce a single seismic reflection with a stronger amplitude response. (B) Indicates the position of the seismic profile.



### 5.4.1 Area 1

Figure 5.16A is a seismic profile with a west-east orientation. Figure 5.16E represents the location of the seismic profiles that cross-cuts well 7435/12-1. The amplitude anomaly (AA1) is situated in the top Stø Formation (figure 5.16B & 5.16F). By using a seismic wiggle trace section (figure 5.16C), the same amplitude is observed with a reversed polarity relative to the seafloor reflection. A flat spot can be observed in the Stø Formation.

Where well 7435/12-1 penetrates the flat spot, a gas-water contact (GWC) was identified at depths of 612 m, equivalent of 620 ms (TWT). The seismic reflection of the flat spot emits an RMS response ranging from ~1400 to ~4000 (figure 5.16D). According to NPD (2017d), Well 7435/12-1 proved 6 – 12 billion Sm<sup>3</sup> of recoverable gas.

The flat spot is associated with an overlying bright spot situated in the top Stø Formation. The bright spot corresponds to a negative RMS response ranging from ~1300 to ~3100 (figure 5.16D). Along its 3D planar view, the area of AA1 was measured to 99.98 km<sup>2</sup>. Its structural closure indicated a vertical distance of 35 ms (TWT) from the top of the bright spot to the flat spot reflection. The outer flanks of the amplitude anomaly seem to be bounded by deep-seated faults, with a sealing structure that seems to dip in all directions (figure 5.16B & 5.16F).

Appendix 10.3A illustrates the localised water column data (WCD line 4651) above figure 5.16A. No hydroacoustic signatures were identified along the WCI.

Specified composite line

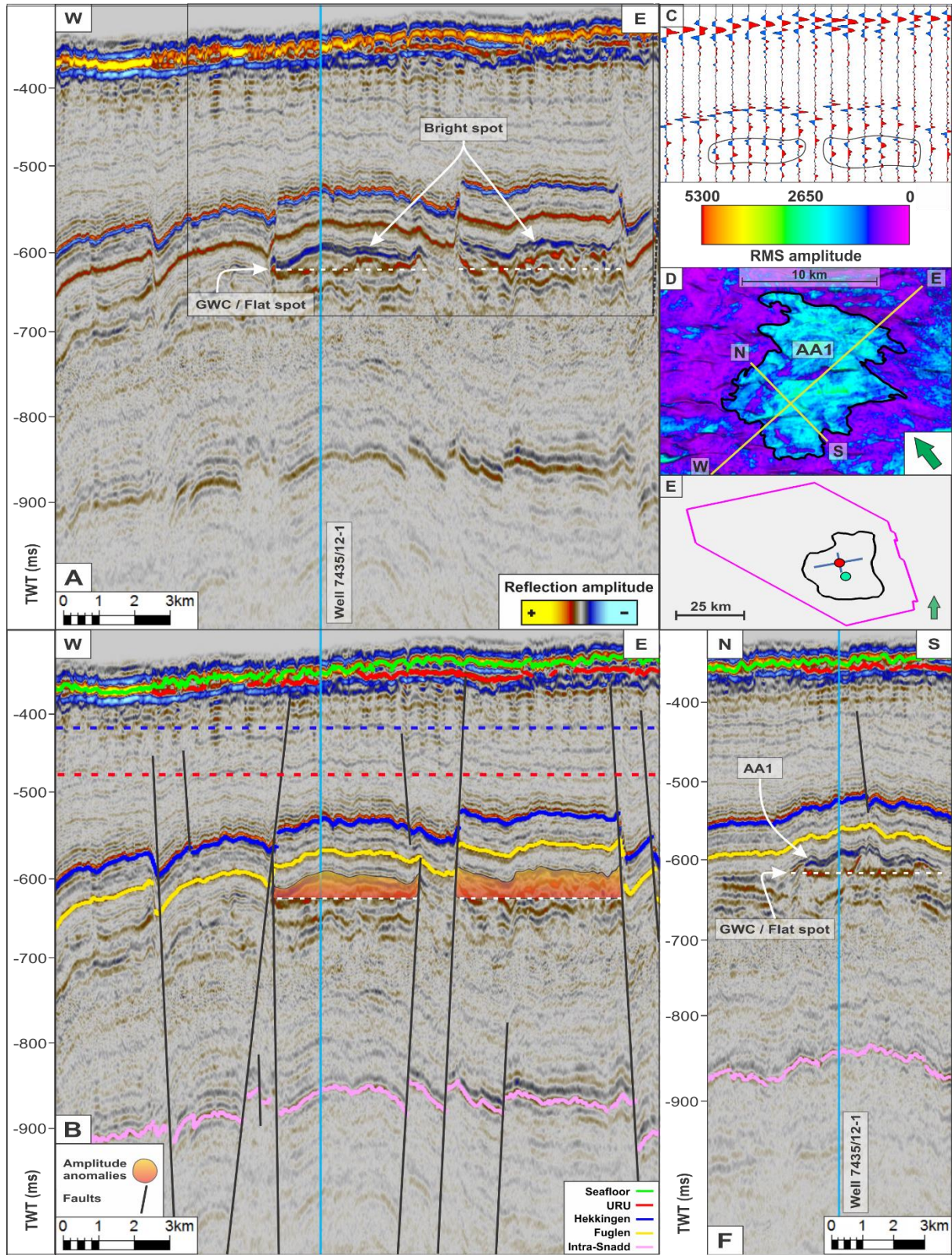


Figure 5.16: Area 1 illustrating (A) the uninterpreted seismic 3D composite line with a W-E orientation. The blue vertical line represents borehole 7435/12-1. (B) The interpreted seismic horizons and faults. Red (from well 7324/8-1) and blue (from well 7226/2-1) dotted line represents the modelled BSRs (C) Seismic wiggle section of the 3D composite line, showing the polarity reversal (black circles) of the interpreted amplitude anomalies in relation to the seafloor reflection. (D) RMS amplitude surface of the amplitude anomaly (within the black polygon) in the Stø Formation. Yellow lines illustrate the orientation of the seismic profiles. (E) The position of the seismic profiles with well 7435/12-1 (red) and 7335/3-1 (green). (F) A cross-section of the W-E oriented composite line.

## 5.4.2 Area 2

Figure 5.17A is a seismic profile from the Haapet Dome area with a southwest-northeast orientation (figure 5.17E). A seismic wiggle section (figure 5.17C) of xline 8300 illustrates the reversed polarity of the interpreted amplitude anomalies (figure 5.17B) in relation to the seafloor reflection.

The amplitude anomalies are primarily situated in the Stø Formation, with an overlying amplitude anomaly located beneath the seafloor reflection (figure 5.17A). Four amplitude anomalies were identified in the Stø Formation (figure 5.17B). The southwestern amplitude anomaly (AA1) is related to the previous amplitude anomaly from figure 5.16D. Further northeast, three additional amplitude anomalies were identified, comprising an area of  $\sim 1.9 \text{ km}^2$  (AA2),  $\sim 2.7 \text{ km}^2$  (AA3) and  $\sim 9.6 \text{ km}^2$  (AA4). Overall, the amplitude anomalies reflected an RMS response ranging from  $\sim 1300$  to  $\sim 3100$ , where the smallest amplitude anomalies correspond to the lowest RMS values.

The shallowest amplitude anomaly occurs at depths from 345 to 395 ms (TWT). The RMS amplitude reflects an amplitude response ranging from  $\sim 3000$  to  $\sim 13000$ . Between two major deep-seated faults (figure 5.17B), a dimmed zone of chaotic reflections (acoustic masking) is present. Below the shallowest amplitude anomaly, a push-down effect can be observed. Such occurrence might develop beneath fluid accumulations (most often gas), illustrated as low seismic velocity intervals. Along the seismic xline 8300, the trap configuration for the amplitude anomalies in the Stø Formation seems to be bounded by faults, with a sealing structure that is dipping both southwest (AA1, AA2 and AA3) and northeast (AA4) (figure 5.17B).

Appendix 10.3B illustrates the water column data (WCD line 6489) above figure 5.17A. No hydroacoustic signatures were observed along the WCI.



Seismic 3D xline 8300

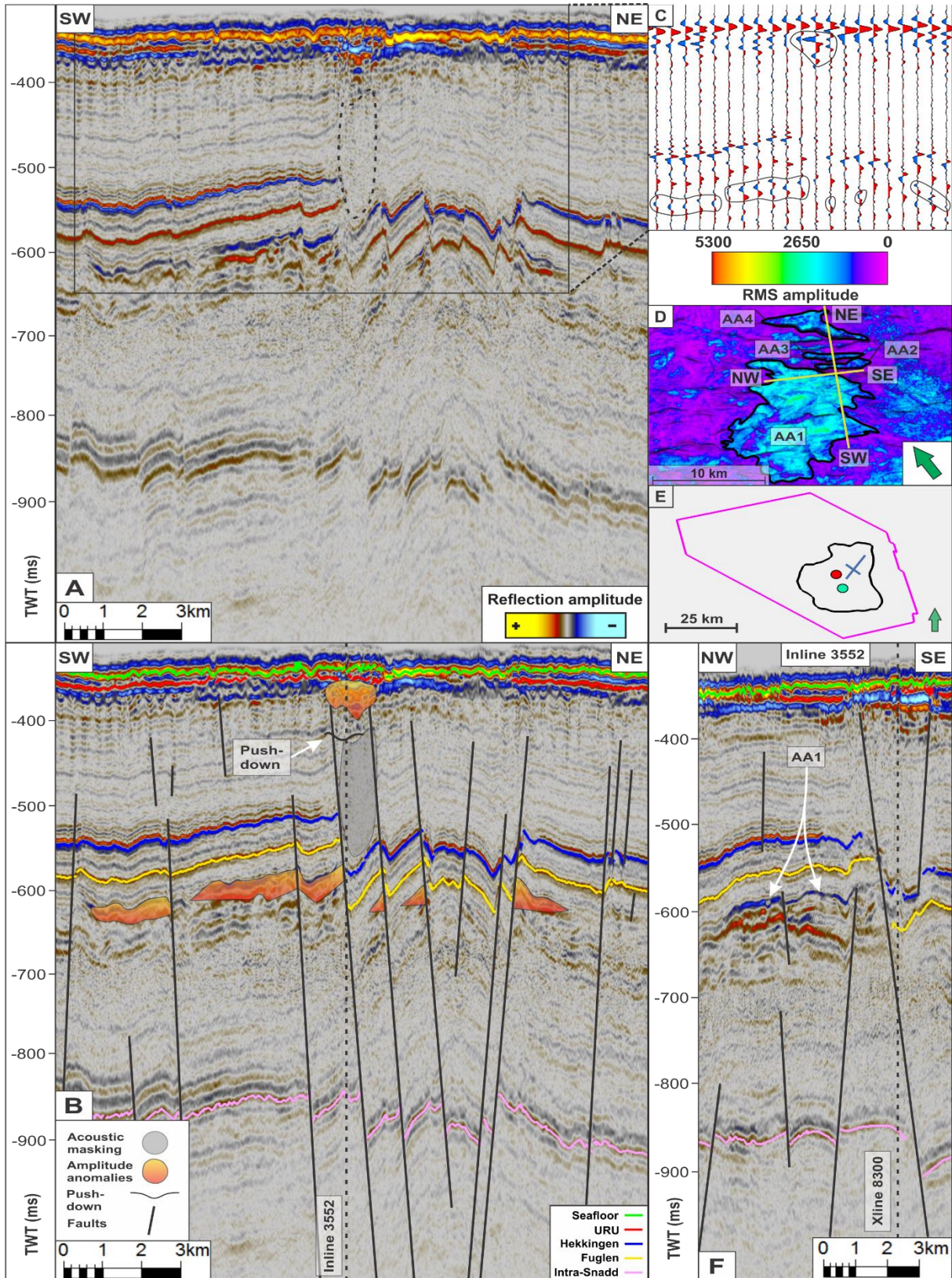


Figure 5.17: Area 2 illustrating (A) the uninterpreted seismic 3D xline 8300. (B) The interpreted seismic horizons and faults. (C) Seismic wiggle section of the 3D xline 8300, indicating the polarity reversal (black circles) of the interpreted anomalies compared to the seafloor reflection. (D) RMS amplitude surface of the amplitude anomalies (within the black polygons) in the Stø Formation. Yellow lines illustrate the orientation of the seismic profiles. (E) The position of the seismic profiles with well 7435/12-1 (red) and 7335/3-1 (green). (F) A cross-section of the 3D inline 3552 seismic profile.

### 5.4.3 Area 3

This area (figure 5.18E) encompasses two amplitude anomalies situated in the Stø Formation. Figure 5.18C illustrates the polarity changes (black circles) compared to the seafloor reflection.

Figure 5.18D was composed to investigate the size of the amplitude in the Stø Formation. From figure 5.18D, the amplitude anomalies seem to be connected (AA5). The amplitude anomaly emits an RMS amplitude response ranging between ~1300 to ~4100, where the RMS amplitude response is increasing towards the deep-seated fault with the largest fault throw in the study area (~185 ms (TWT)). The AA5 comprises an area of ~48.2 km<sup>2</sup>.

A vertical distance of 65 ms (TWT) beneath the structural apex (top of the AA5) a potential flat spot can be observed (figure 5.18A & 5.18F). The potential flat spot is situated at depths of ~575 ms (TWT), emitting an RMS amplitude response between ~1300 to ~2100. Two deep-seated faults are penetrating the AA5 (figure 5.18B). Above the down-faulted hanging wall, which encloses the larger amplitude anomaly, identification of smaller amplitude anomalies (RMS response between ~1400 to ~7500) can be observed (figure 5.18A). The AA5 seem to be bounded by faults, with a sealing structure that dips towards the east (figure 5.18B) and north (figure 5.18F).

Appendix 10.3C displays the localised water column data (WCD line 4436) above figure 5.18A. No hydroacoustic signatures were identified along the WCI.



Specified composite line

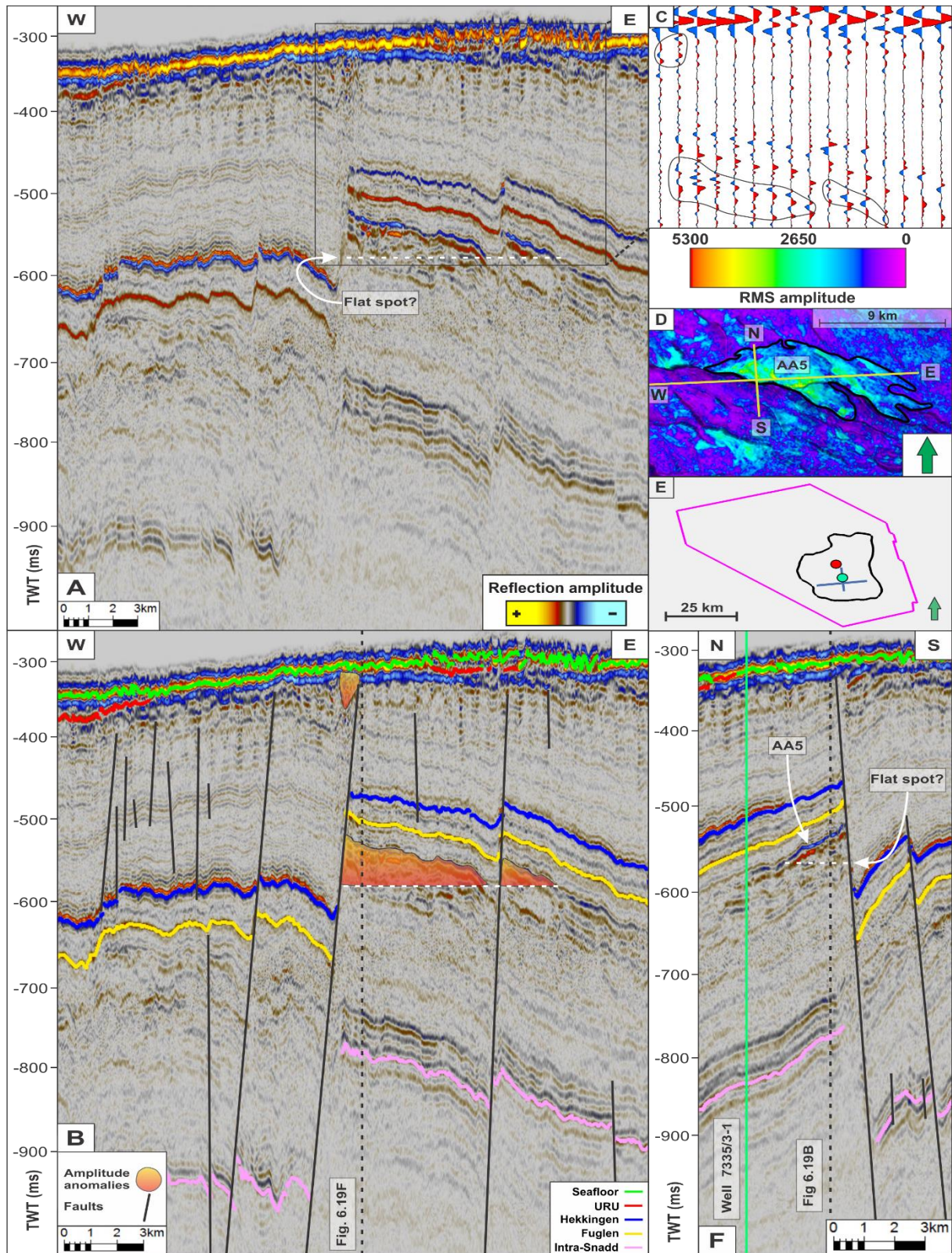


Figure 5.18: Area 3 illustrating (A) the uninterpreted seismic 3D composite line with a W-E orientation. (B) The interpreted seismic horizons and faults. (C) Seismic wiggle section of the 3D composite line, showing the polarity reversal (black circles) of the interpreted amplitude anomalies compared to the seafloor reflection. (D) RMS amplitude surface of the amplitude anomalies (within the black polygons) in the Stø Formation. Yellow lines illustrate the orientation of the seismic profiles. (E) The position of the seismic profiles with well 7435/12-1 (red) and 7335/3-1 (green). (F) A cross-section perspective of the W-E oriented composite line. The vertical green line represents borehole 7335/3-1.

#### 5.4.4 Area 4

Another amplitude anomaly (AA6) is observed in the Stø Formation (figure 5.19B) in the northwestern parts of the study area, linked with a smaller amplitude anomaly found beneath the seafloor horizon (figure 5.19B). Figure 5.19C represents the reversed phase polarity of the amplitude anomalies. A potential flat spot is observed in figure 5.19F, suggesting the presence of a fluid contact.

The northwestern parts of the study area enclose a stratigraphic high. The identified AA6 were further investigated in figure 5.19D. From its 3D planar view, the amplitude anomalies seem to be connected, comprising an area of  $\sim 57.3 \text{ km}^2$ . The outer and inner black polygons were defined based on the presence of faults (figure 5.19D). Being penetrated by four deep-seated faults, the AA6 emits an RMS amplitude response ranging from  $\sim 1300$  to  $\sim 5000$  (figure 5.19F). Beneath the seafloor horizon, a smaller amplitude anomaly is occurring (figure 5.19B) with an RMS amplitude response between  $\sim 1300$  to  $\sim 5000$ .

The potential flat spot (figure 5.19F) was measured with a horizontal length of  $\sim 1.4 \text{ km}$ , situated at a depth of 613 ms (TWT). From its structural apex, a vertical distance of 26 ms (TWT) was measured. The flat spot measured an RMS amplitude response between  $\sim 4000$  to  $\sim 8000$ .

An extensive vertical zone of acoustic masking is indicated in figure 5.19B, which appears to delineate the AA6 in the Stø Formation. Figure 5.19F shows that the acoustic masked zone is a result of two deep-seated faults cross-cutting one another. The AA6 seems to be bounded by several faults, with a complex sealing structure that seem to be dipping in several directions (figure 5.19B & 5.19F)

No water column data has been acquired in area 4.



Seismic 3D inline 4650

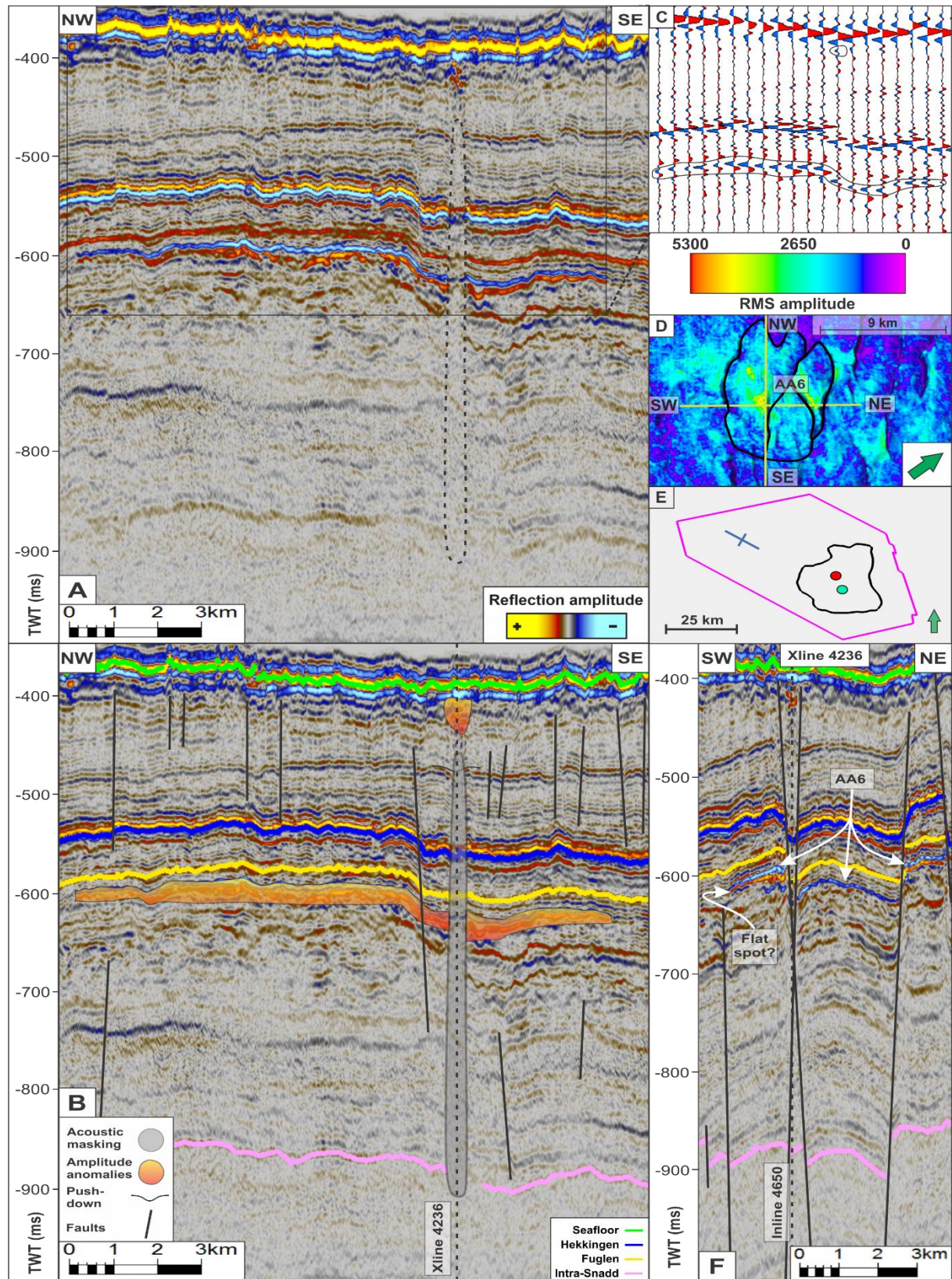


Figure 5.19: Area 4 illustrating (A) the uninterpreted seismic 3D inline 4650. (B) The interpreted seismic horizons and faults. (C) Seismic wiggle section of the 3D inline 4650, illustrating the polarity reversal (black circles) of the interpreted anomalies compared to the seafloor reflection. (D) RMS amplitude surface of the amplitude anomalies (within the black polygons) in the Stø Formation. Yellow lines illustrate the orientation of the seismic profiles. (E) The position of the seismic profiles with well 7435/12-1 (red) and 7335/3-1 (green). (F) A cross-section of the 3D xline 4236 seismic profile.



## 5.5 Potential gas flares and shallow amplitude anomalies

A total number of 2192 water column lines from the MAREANO program (data-volume of ~4.95 TB) was processed and analysed. Information about the processed water column data can be retrieved from appendix 10.2. This chapter emphasises the evaluation of two hydroacoustic signatures that can be related to gas seepage. Potential gas leakage evaluation was conducted in chapter 3.6. The hydroacoustic signatures will be defined based on the characteristics of a potential gas flare and the correlation with subsurface strata. The north-south distance between each gathered WCD line is ~400 m, making it difficult to interpret the exact position of the potential gas flares. Thus, the position of potential gas flare 1 and 2 deviates with ~500 m and ~150 m, respectively.

### 5.5.1 Location 1

The processed water column data (WCD), which emphasises WCD line 6902 (figure 5.20B and 5.20C), reveals the presence of a vertical hydroacoustic feature, situated on the edge of the Haapet Dome structural element (figure 5.20D). Its hydroacoustic signature suggests the presence of a small potential gas flare. The signature comprises a recorded decibel spectrum of 0 to -28 dB, with an average value of ~21 dB, with a detectable height of 25 m.

A vertical exaggeration of 4 was used to enhance the size of the potential gas flare 1, including the surrounding topographic features. Through the R-stacked profile (figure 5.20C), remains of weak acoustic distortion is observed. The potential gas flare 1 records a brighter amplitude anomaly compared to the prominent artefacts. Thus, it can be separated from most of the acoustic distortion. Figure 5.20B shows the presence of the potential gas flare 1 in a fan view.

As stated in chapter 3.6, the hydroacoustic signatures for potential gas flares are evaluated according to their characteristics. Thus, only the central hydroacoustic feature (within the white rectangle) was emphasised in figure 5.20C. From chapter 3.6, the remaining anomalies are assumed to be results of potential plankton or fish. However, according to the criteria's for gas flare evaluations, the identified hydroacoustic signature illustrates a degree of uncertainty regarding the possibility of gas seepage in this area, which will be further assessed in the discussion part.

WCD Line 6902

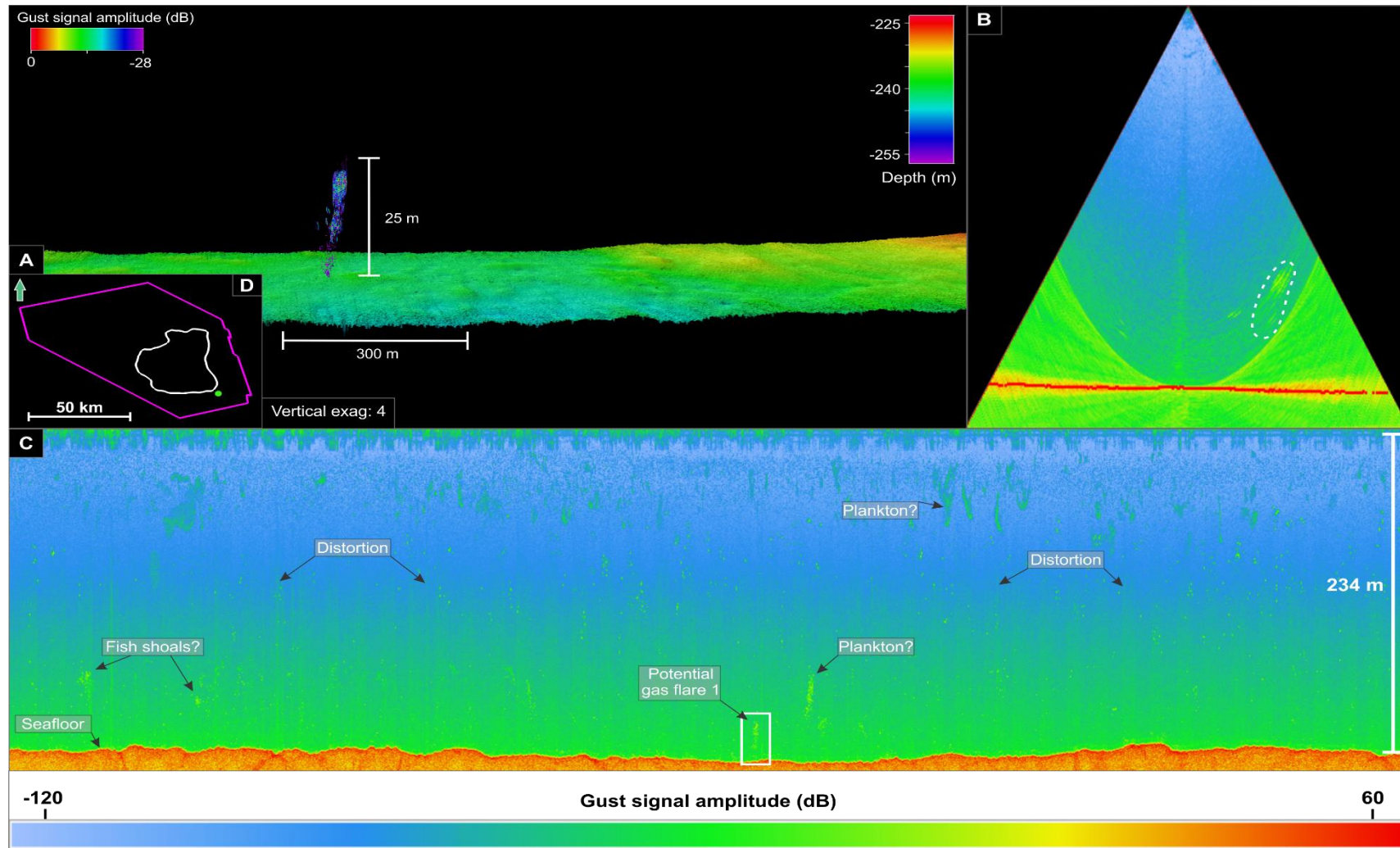


Figure 5.20: (A) 3D view of the surface line 6902, illustrating a potential gas flare of 25m with a vertical exaggeration of 4. Its hydroacoustic signature was measured in decibel (dB). (B) Displays the potential gas flare (strong amplitude anomalies within the white polygon) in a fan view. One fan stack was used to enhance the anomalies of the possible gas flare. (C) Water column data (WCD) shown in an R-stack view. The potential gas flare is situated within the white rectangle. (D) A green dot marks the location of the potential gas flare within the study area. Data from Mareano (2014).

The potential gas flare 1 was further correlated with subsurface strata to investigate the possibility of gas seepage in this area. The area (figure 5.21E) encloses amplitude anomalies (AA7 and AA8) confined beneath the seafloor horizon (figure 5.21B). A seismic wiggle section (figure 5.21C) was used to locate the amplitude anomalies.

Three amplitude anomalies were observed beneath the seafloor (figure 5.21A). The AA7 and AA8 comprise an RMS amplitude response between 1400 and 6800 (figure 5.21D). A connection between the two most southeastern amplitude anomalies (AA7) are suggested (figure 5.21B). Along its time-slice intersection, the area of AA7 and AA8 were measured to  $\sim 1.5 \text{ km}^2$  and  $\sim 0.88 \text{ km}^2$ . The potential gas flare 1 was localised above the strongest amplitude response, situated in the southeastern parts of figure 5.21D (Green circle).

Figure 5.21F illustrates that the dimmed zone is related to fault development, which terminates beneath the seafloor horizon. Internally, zones of acoustic masking can be referred to as push-down effects. In total, five areas of possible push-down effects are observed, where four of them are situated in the most northwestern dimmed zone (figure 5.21B).



Seismic 3D inline 4466

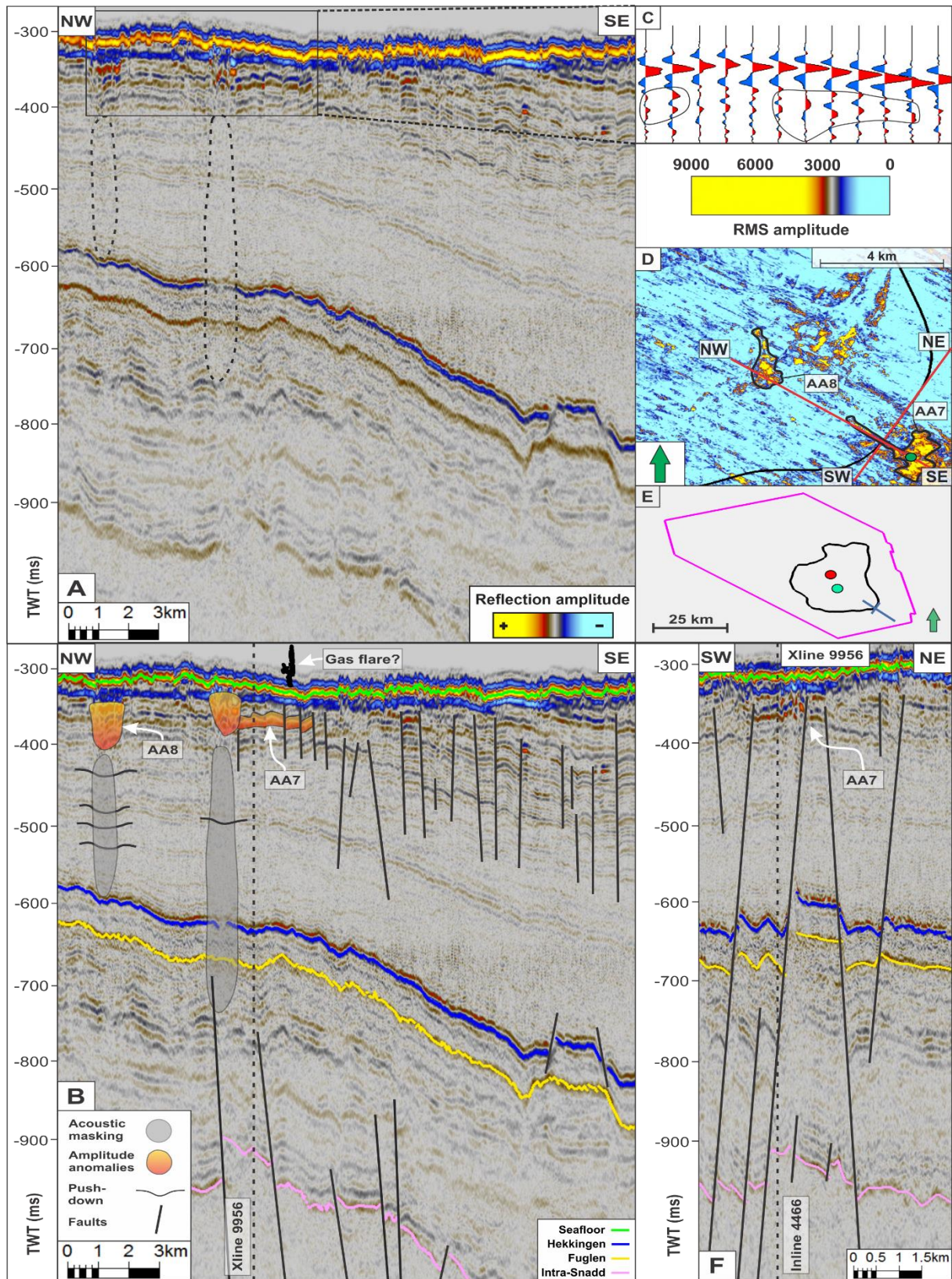


Figure 5.21: (A) Uninterpreted seismic 3D inline 4466. (B) The interpreted seismic horizons and faults. Note that the potential gas flare is not to scale. (C) Seismic wiggle section of the 3D inline 4466, illustrating the polarity reversal (black circles) of the interpreted anomalies compared to the seafloor reflection. (D) RMS amplitude time-slice (348 ms (TWT)) of the emphasised amplitude anomalies (within the black polygons) beneath the seafloor reflection. Red lines illustrate the orientation of the seismic profiles. (E) The position of the seismic profiles with well 7435/12-1 (red) and 7335/3-1 (green). (F) A cross-section of the 3D xline 9956 seismic profile.

## 5.5.2 Location 2

Another hydroacoustic signature was observed adjacent to a terminating URU horizon (figure 5.24B). It comprises the processed WCD line 4842, which emphasises the extensional feature (white rectangle) in figure 5.22C. The hydroacoustic feature is situated northwest of the Haapet Dome structural element (figure 5.22D).

The hydroacoustic signature reflects a decibel spectrum between -10 to -55 dB, with an average anomaly value of -52 dB. Its extensional length was measured to 263 m, assuming that the flare has a connection with the seafloor.

A vertical exaggeration of 4 was used to enhance the topographic features and the size of what could be a potential gas flare. As a result of improved resolution (1-meter grid), small pockmarks can be detected along the seafloor, reaching widths of ~25 m and depths of ~2.5 m.

Distribution of vertical thin lines (acoustic distortion) is scattered across the profile (figure 5.22C), reaching a vertical length of ~140 m. The potential gas flare 2 shows similar decibel spectrum as the adjacent acoustic distortion. Hence, if the colour scheme (figure 5.23A) were reduced to minimise the artificial error, the flare would fade away (figure 5.23B). Figure 5.22B displays the difficulties in determining the length of the flare. The dotted line illustrates the traceable length.

Overall, the potential gas flare 2 (figure 5.22A) comprises a lower section of stronger amplitude anomalies, compared to its upper amplitude anomaly section. A couple of pockmarks seem to be situated beneath the potential gas flare. Similar to the potential gas flare 1, the potential gas flare 2 comprises some uncertainties regarding the criteria's for gas flare evaluations, which will be further assessed in the discussion part. Besides, a connection to the seafloor was only estimated, not determined.



WCD Line 4842

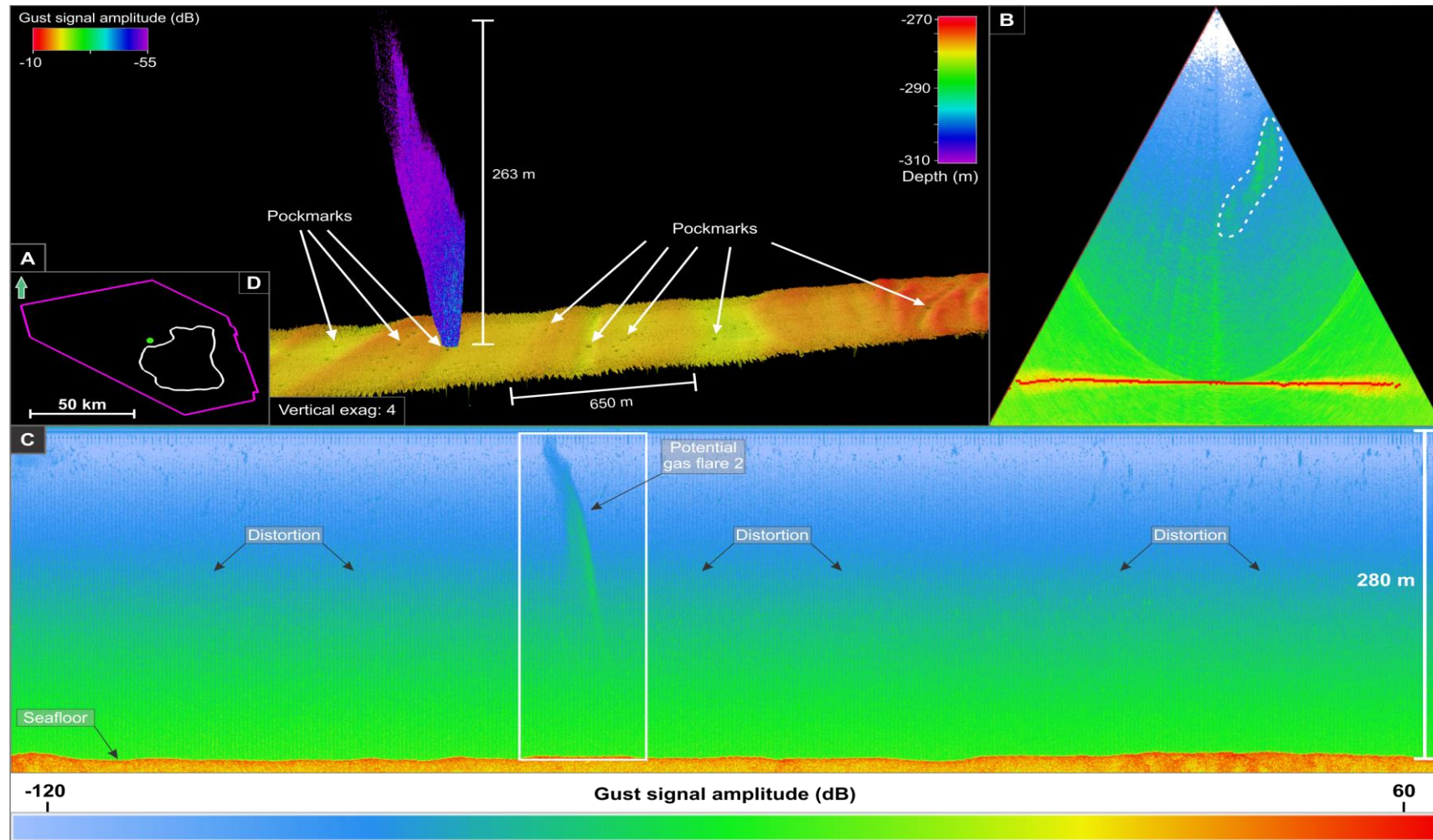


Figure 5.22: (A) 3D view of the surface line 4842, illustrating a potential gas flare of 275m with a vertical exaggeration of 4. Its hydroacoustic signature was measured in decibel (dB). Pockmarks can be identified on the seafloor. Note that the flare was assumed to have a connection with the seafloor. (B) Displays the potential gas flare (strong amplitude anomalies within the white polygon) in a fan view. One fan stack was used to enhance the anomalies of the potential gas flare. (C) Water column data (WCD) shown in an R-stack view. The assumed gas flare is situated within the white rectangle. Note that the surrounding distortion made it difficult to tell if the potential flare had a connection with the seafloor or not. (D) A green dot marks the location of the potential gas flare within the study area. Data from Mareano (2014).

## WCD Line 4842

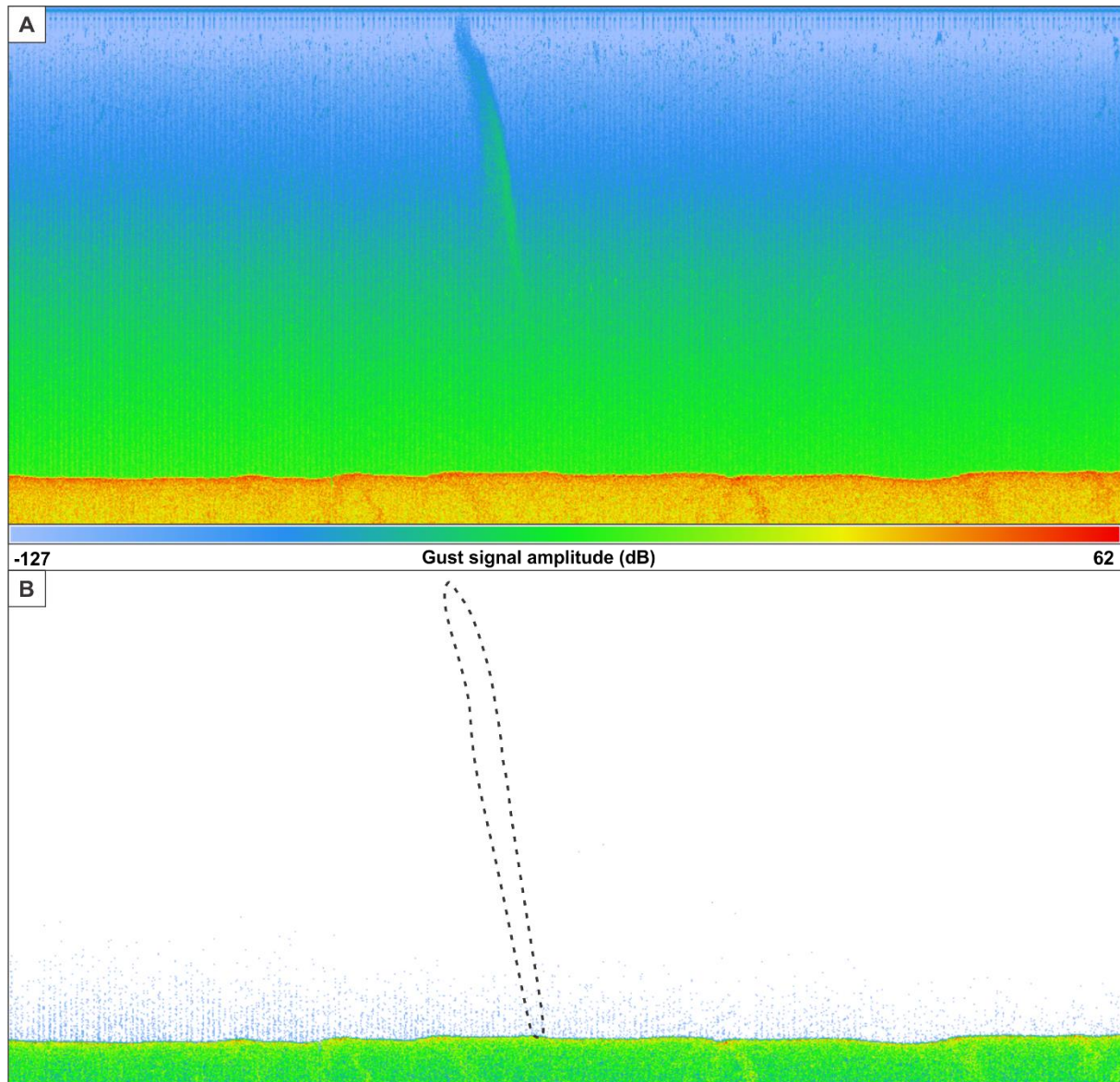


Figure 5.23: (A) R-stack view of the WCD line 4842 with emphasis on the potential gas flare located in the middle. The figure reflects a decibel colour spectrum between -127 dB to 62 dB. (B) Displays the same r-stack view of WCD line 4842. Note that the colour scale has been reduced to a decibel spectrum of -23.24 dB to 62 dB. The stippled polygon indicates where the potential gas flare is supposed to be. Data from Mareano (2014).



A correlation with subsurface strata was conducted for the potential gas flare 2. The area encloses a single amplitude anomaly, which was observed beneath the URU horizon (figure 5.24A & 5.24B).

A seismic wiggle section was used to localise the reversed phase polarity of the selected amplitude anomaly (figure 5.24C). By using the RMS time-slice (figure 5.24D), the observed amplitude anomaly (AA9) seems to comprise a group of smaller amplitude anomalies. The AA9 encloses an RMS amplitude response of 1800 to 5000, with an area of ~2.1 km<sup>2</sup>. The adjacent anomalies are related to the reflection of the seafloor.

The potential gas flare 2 was identified where the URU horizon terminates towards the southwest in figure 5.24B, with a deep-seated fault localised beneath. Besides the AA9, no evidence of strong amplitude anomalies with a connection to the potential gas flare 2, was localised in the subsurface or along the adjacent faults (figure 5.24A, 5.24B & 5.24F).

Seismic 3D xline 6592

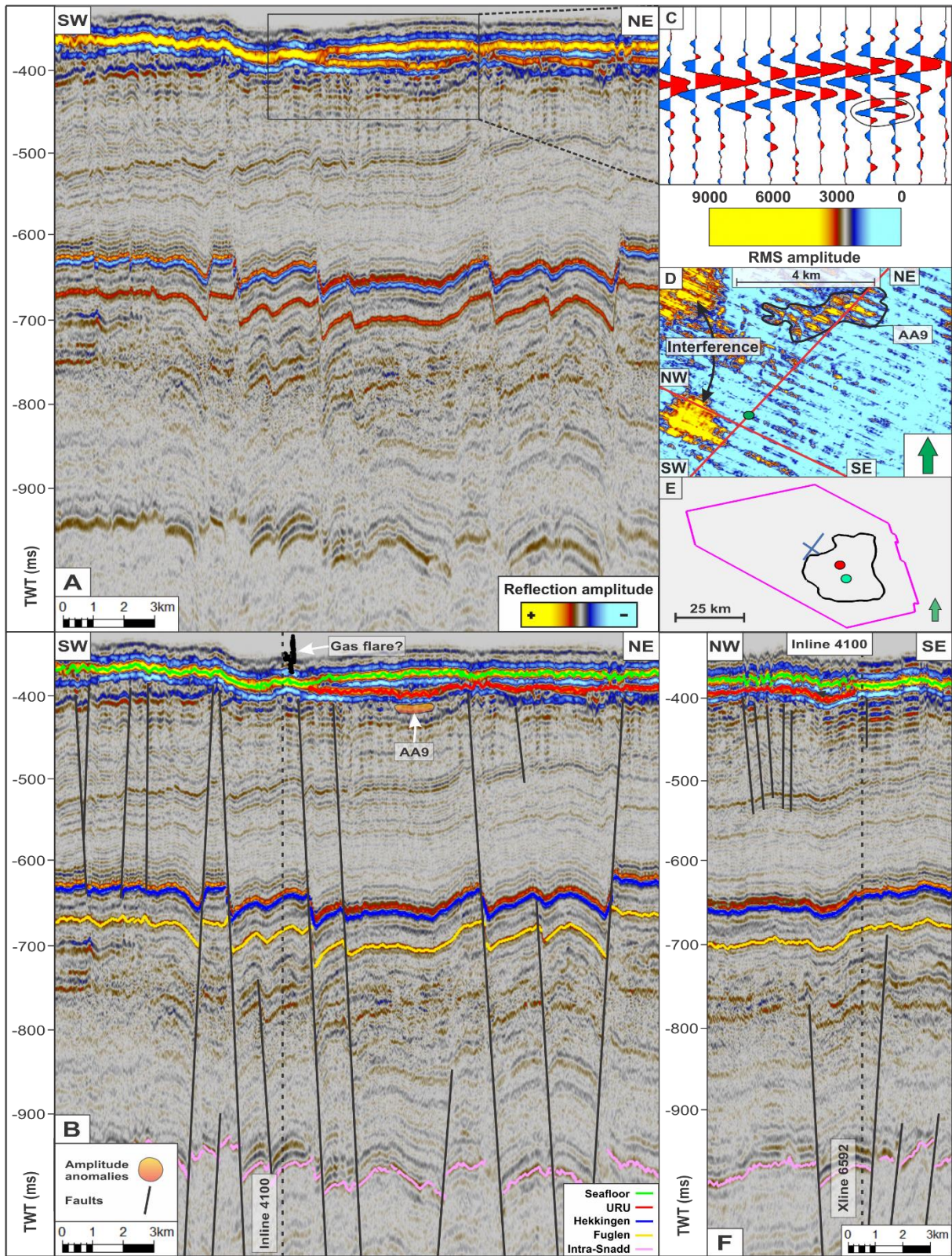


Figure 5.24: (A) Uninterpreted seismic 3D xline 6592. (B) Displays the seismic interpretations in accordance with the location of the potential gas flare. Note that the potential gas flare is not to scale. (C) Seismic wiggle section of the 3D xline 6592, illustrating the polarity reversal (black circles) of the interpreted anomaly compared to the seafloor reflection. (D) RMS amplitude time-slice (414 ms (TWT)) of the emphasized amplitude anomalies (within the black polygons) beneath the URU reflection. Red lines illustrate the orientation of the seismic profiles. (E) The position of the seismic profiles with well 7435/12-1 (red) and 7335/3-1 (green). (F) A cross-section of the 3D inline 4100 seismic profile.

## **6 Discussion**

The following chapters aim to investigate the possibility of gas seepage in relation to subsurface migration pathways. Hence, five migration models were evaluated in connection with shallow amplitude anomalies and potential gas seepage.

The study area comprises both shallow amplitude anomalies (figure 5.16B – 5.18B) and two areas of potential gas seepage (figure 5.21 & 5.24). Two models were proposed to evaluate the identified amplitude anomalies relative to possible entrapment zones, which involves (#1) glaciogenic sediments as a seal and (#2) the existence of stable gas hydrates as potential seals. At the end of the chapter, a discussion of model #3 will evaluate the possibility of an active source rock, relative to potential hydrocarbon generation.

The individual models will be supported by seismic observations and published work. Finally, a conceptual model for subsurface migration and potential seepage in the Haapet Dome area will be implemented.

### **6.1 Subsurface drainage systems**

This chapter incorporates the evaluation of the potential pathways for gas migration (figure 6.1 – 6.3). Well 7435/12-1 discovered gas-bearing sediments in the Stø Formation. The identified gas accumulation (figure 5.13) in the Haapet Dome area encompasses adjacent amplitude anomalies, with almost identical seismic amplitude responses (chapter 5.4.1 – 5.4.3) of which was observed from the gas accumulation where exploration well 7435/12-1 was drilled. Besides, the amplitude anomalies are situated at approximately similar stratigraphic depths (~600 m), which encompasses the same reservoir interval (the Stø Formation). This suggests that the nearby amplitude anomalies could also be results of potential gas accumulations.

As the shallow seismic amplitude anomalies might represent gas accumulations, the presence of a deeper source rock will be further evaluated in chapter 6.4. The expulsion of gas initiates when the source rock exceeds critical rates of burial. The process of pressure differences could result in assumed gas migration from areas of higher pressure to lower pressures by forces of buoyancy. If forces of buoyancy are sufficient, vertical or lateral movements of hydrocarbons could proceed, dependent on the overlying lithology (Schowalter, 1979).

Amplitude anomalies are spatially distributed throughout the Stø Formation (below the top Fuglen Horizon) and beneath the seafloor horizon (e.g. figure 5.16 – 5.19). There seems to be a link between faults and the assumed gas accumulations, given that the accumulations are observed along structures delineated by faults – e.g. along fault blocks (figure 5.16, 5.17, 5.18, 5.19 & 5.21). Faults could act as conductors for hydrocarbon transportation or develop closures for accumulations. The majority of the amplitude anomalies are situated in the footwalls (figure 5.16 – 5.18) of deep-seated faults. These structures are possibly related to the extensional rifting phase that lasted until Early Cretaceous.

### **6.1.1 Migration modelling**

The possible leakage zones examined in chapter 5.4 and 5.5 illustrates that the assumed migration pathways are mainly controlled by faults. Zones of low reflectivity, acoustic masking, push-down effects and amplitude anomalies suggest the presence of gas. These assumed gas accumulations were mainly observed in conjunction with faults. In chapter 3.3.2, faults were suggested to represent zones of vertical migration pathways for redistribution of hydrocarbons.

In well 7435/12-1, the sandstones of the Stø Formation proved good to moderate reservoir quality (NPD, 2017a), which could act as carrier beds for lateral migration. The overlying Fuglen Formation indicates moderately high velocity values (Table 4.2), a sharp increase in gamma ray- (figure 5.3A) and density responses, which is a characteristic feature for mudstones (Dalland et al., 1988). Well 7435/12-1 also confirmed moderate to high density properties for the Fuglen Formation, which act as a sealing rock for underlying gas.



The migration models (figure 6.1 – 6.3) indicate that gas, which originates from a deeper stratigraphic level than the Intra-Snadd formation, might have migrated upwards and eventually reached a zone of accumulation. In area 1 (figure 6.1A), a gas migration pathway to the Stø Formation was suggested. No amplitude anomalies were observed in the Cretaceous unit, implying that the fault structures could act as a seal in combination with the dense lithology of the Fuglen Formation. Vrolijk et al. (2016) illustrate that fault processes that deform layered stratigraphy (in this case, the Fuglen Formation) could develop clay-smearing along its fault plane and prevent further migration, and which might be the case for the Fuglen Formation in the study area. Based on the evaluated trap configuration from chapter 5.4.1, the presumed gas accumulation in area 1 was suggested to be stored in a fault-bounded dip closure.

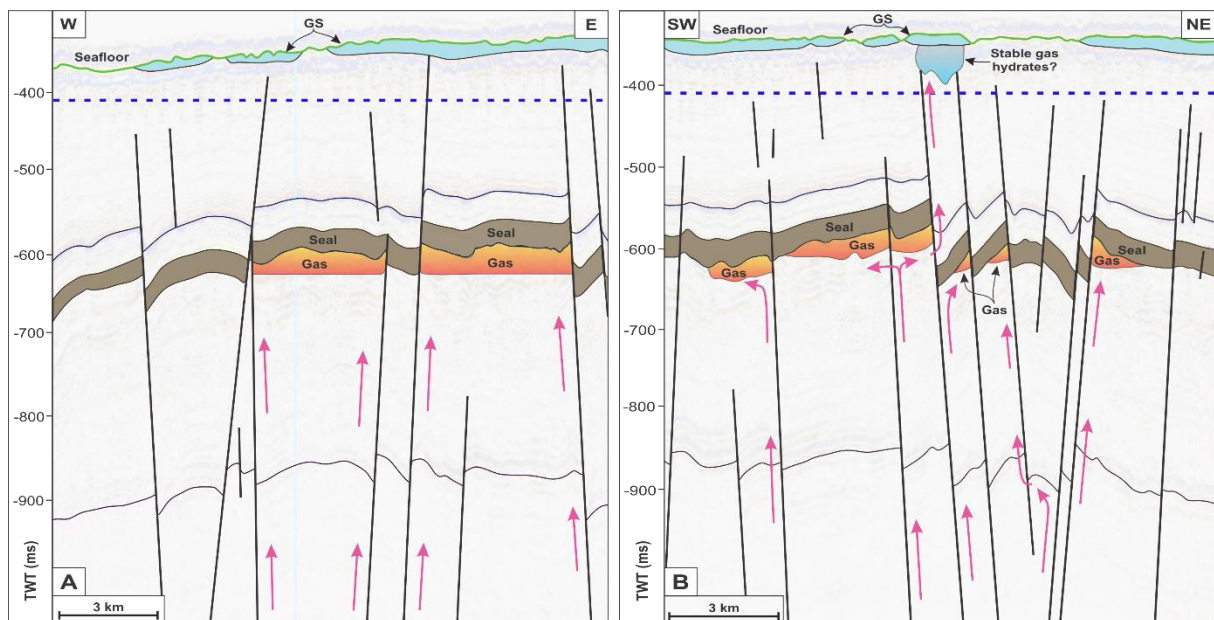


Figure 6.1: (A) Displays a possible migration pathway for gas along area 1. (B) Illustrates a possible migration pathway for gas along area 2. GS = Glacigenic sediments. Notice how the shallowest presumed gas accumulation could develop a potential zone of stable gas hydrates (see text for discussion). The blue dotted line represents the modelled BSR from well 7226/2-1. Pink arrows indicate the potential migration pathways. The location can be found in figure 5.16E and 5.17E. Constructed from figure 5.16B and 5.17B.

Area 2 (figure 6.1B) encompasses several assumed gas accumulations in the Stø Formation, with a potential overlying accumulation situated beneath glacigenic sediments. The deep-seated faults are assumed to be the controlling factors for vertical migration. Several faults terminate in the lower Cretaceous unit, which might constrain further vertical migration. According to the evaluated closures from chapter 5.4.2, the presumed gas accumulations in the Stø Formation are suggested to be stored in fault-bounded dip closures.

Area 3 (figure 6.2A) comprises a similar scenario as area 2, where possible gas accumulations are situated in the Stø Formation, including a smaller accumulation observed in the younger stratigraphy, probably of Early Cretaceous age below the seabed. In this case, the migration pathways are suggested to be controlled by faults. The amount of vertical rock displacement is about ~185 ms (TWT). Area 2 and 3 illustrate that the shallowest presumed gas accumulation could be representative of potential stable gas hydrates, as it was located above the modelled BSR. Similar to area 1 and 2, the presumed gas accumulation in the Stø Formation was also suggested to comprise a potential fault-bounded dip closure in area 3.

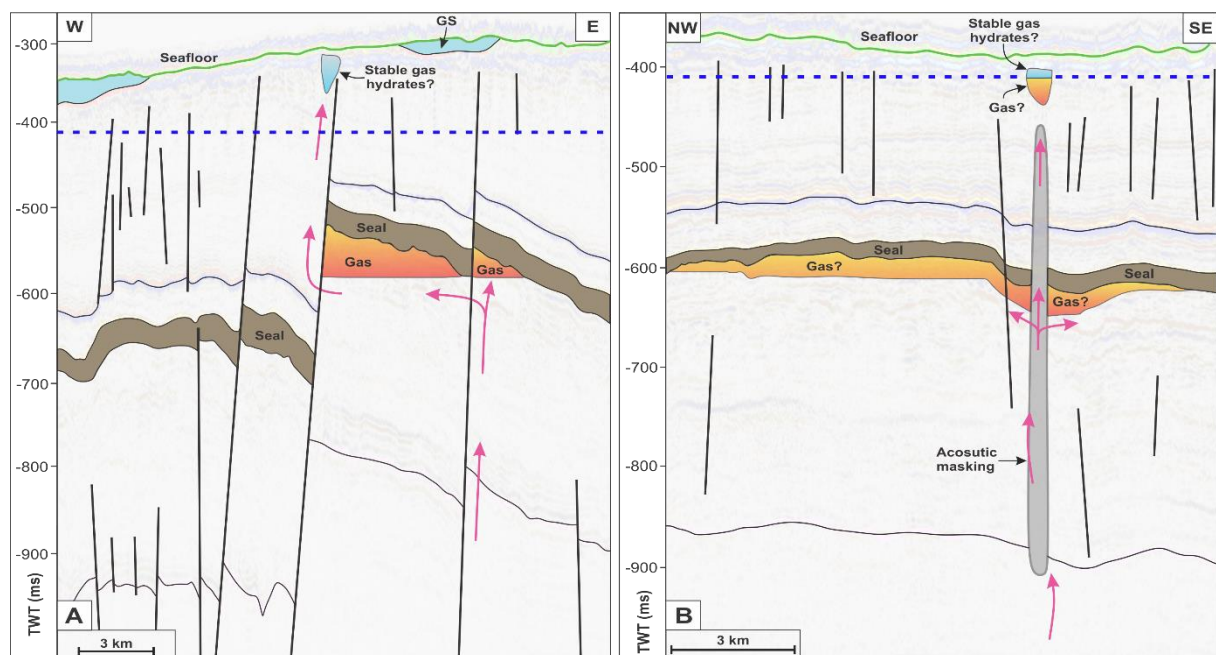


Figure 6.2: (A) Displays a possible migration pathway for gas along area 3. (B) Illustrates a possible migration pathway for gas along area 4. GS = Glacigenic sediments. Notice how the shallowest presumed gas accumulations could develop a potential zone of stable gas hydrates (see text for discussion). The blue dotted line represents the modelled BSR from well 7226/2-1. Pink arrows indicate the potential migration pathways. The location can be found in figure 5.18E and 5.19E. Constructed from figure 5.18B and 5.19B.

Area 4 (figure 6.2B) involves possible gas accumulations, penetrated by several deep-seated faults (figure 5.19F). The possible gas accumulation is linked to a vertical zone of acoustic masking (figure 6.2B). As shown in chapter 5.4.4, the acoustic masked zone is a result of two deep-seated faults, possible representing the controlling factor for migration in this area. Given that a smaller accumulation is situated above the zone of acoustic masking, possibly sealed by a stable zone of gas hydrates, implies vertical migration through the Cretaceous unit. Area 4 comprise a possible trap structure that involves several up-faulted and down-faulted blocks that enclose possible gas accumulations (figure 5.19F). Thus, the presumed gas accumulations in the Stø Formation was assumed to be stored in fault-bounded dip closures.



In general, a connection between the presumed gas accumulations as represented by shallow amplitude anomalies and faulting is suggested. However, no evidence of gas seepage was observed from area 1 – 3, based on the analysed water column data. For area 4, the data coverage from figure 1.1 illustrates that water column data was not gathered in the northwestern parts (figure 5.19) of the study area. Hence, the evaluation of potential gas seepage could not be performed in area 4.

### **6.1.2 Potential gas seepage**

In figure 5.17 and 5.18, where shallow amplitude anomalies are situated close to the seafloor, no compelling evidence of gas seepage was observed in the water column data. However, observation of two potential gas flares in figure 5.20 and 5.22, could suggest the possibility of gas leakage (figure 5.21 & 5.24) from the seafloor.

Two hydroacoustic signatures of potential gas seepage have been observed in conjunction with subsurface faults (figure 5.20 & 5.22). The columnar zones of potential gas bubbles from the seafloor will be evaluated according to the following criteria's; (1) the gas flare must be connected to the seafloor, (2) occurrence of a strong acoustic change in impedance in the water column and (3) its morphological feature (Gentz et al., 2014; Veloso et al., 2015; Zhao et al., 2017).

Figure 5.20 represents the potential gas flare 1 along the processed WCD line 6902. From observations (figure 5.20B & 5.20C), no connection between the potential gas flare 1 and the seafloor was observed. In general, gas bubbles emit a greater acoustic change in impedance relative to acoustic distortion (Zhao et al., 2017). By comparing with figure 4.5, an even greater acoustic change in impedance are expected for gas release, which figure 5.20C is lacking. Besides, figure 5.20B and 5.20C show that the assumed gas flare barely exceeds the weak amplitude anomaly of the acoustic distortion.

The morphological feature of the gas bubbles was used to evaluate the acoustic distortion. The upward migration of gas bubbles, through the water column, varies with height, width and area, including the effect of bottom currents (Urban et al., 2017; Zhao et al., 2017).

Beneath the potential gas flare 1, a connection between amplitude anomalies and faults were indicated (figure 5.21B & 5.21F). The migration model (figure 6.3) illustrates what could have been a migration route, based on the location of amplitude anomalies, presence of fault planes and permeable strata.

Figure 5.22 illustrates the potential gas flare 2. The exact length of the hydroacoustic signature could not be determined due to the amount of acoustic distortion. As the morphological shape of the signature could be representative of possible gas seepage, it was assumed to have a connection to the seafloor, despite being disturbed by acoustic distortion. Compared to the potential gas flare 1 (figure 5.20B), the signature from potential gas flare 2 has an even weaker acoustic change in impedance (figure 5.22B).

The identified hydroacoustic signature is extensively distributed, where it almost reaches the sea surface through a water depth of ~280 m. According to Urban et al. (2017), methane gasses that are released from water depths that exceed 150 m are assumed to dissolve before they reach the sea surface. However, Chand et al. (2012) observed flares with a length of 200 m, suggesting that gas bubbles could exceed water depths of 150 m.

Figure 5.24B represents the location of the hydroacoustic signature (figure 5.22C). The potential gas flare 2 is located adjacent to a terminating URU horizon, potentially correlated to subsurface fault zones. However, no amplitude anomalies were identified beneath or along adjacent fault planes. 3.8 km northeast of the potential gas flare, a cluster of smaller amplitude anomalies (figure 5.24D) are detected, which is assumed to be non-influential at present-day, due to its distance.

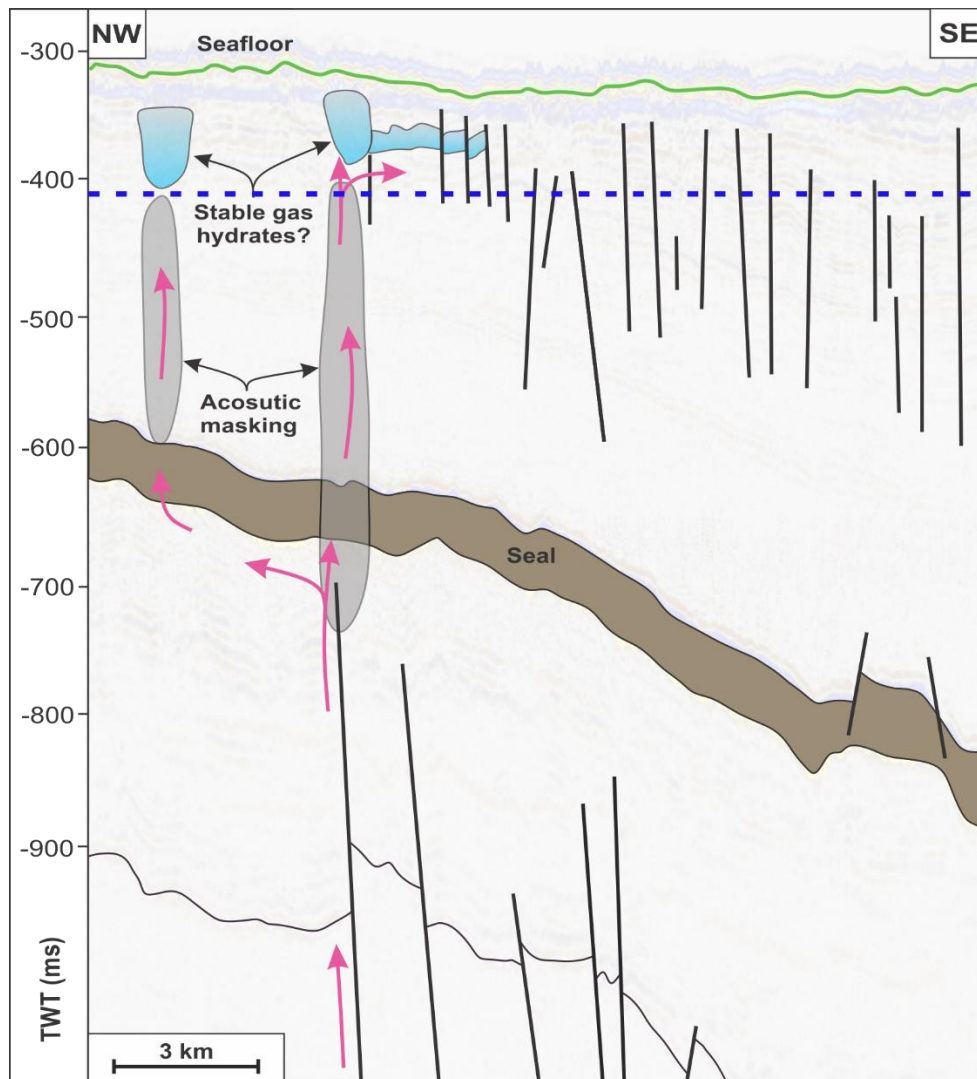


Figure 6.3: Displays a possible migration pathway for gas along area 5. Notice how the shallowest presumed gas accumulations could develop a potential zone of stable gas hydrates (see text for discussion). The blue dotted line represents the modelled BSR from well 7226/2-1. Pink arrows indicate the potential migration pathways. The location can be found in figure 5.21E. Constructed from figure 5.21B.

According to criteria 1 and 2, the potential gas flare 1 is probably not a result of gas release from the seafloor, due to no visible connection to the seafloor and a weak backscatter strength. However, area 5 (figure 6.3) could have released potential gas during a former period, possibly after the last glacial maximum (18000 – 20000  $^{14}\text{C}$  years ago). Chand et al. (2012) clarify that erosion and deglaciation could result in re-opening of pre-existing faults, including the establishment of new faults. Hence, the faults beneath the seafloor (figure 6.3) could have re-opened or been established during this period, which might have enabled further gas migration through the water column.

Based on the same criteria's as the potential gas flare 1, the potential gas flare 2 indicates an even weaker acoustic change in impedance. Besides, a connection to the seafloor could not be determined due to the acoustic distortion, which increases the uncertainty. Hence, the potential gas flare 2 (figure 5.22C) is probably not related to gas seepage, and could be representative of possible plankton or microorganisms, instead.

However, identification of one or two gas bubbles (> 1mm in diameter) could be detected as small hydroacoustic anomalies, if present. In that case, the gas bubble would be displayed as an almost straight line in the water column (figure 4.7). Although, literature that emphasizes detection of single gas bubbles at depths deeper than 100 m, is suggested to be insufficient, due to lack of good quality data (Veloso et al., 2015). Some of the processed water column data from the Haapet Dome area exhibit significant acoustic distortion (figure 5.22C), which complicates the detection of single gas bubble release. Hence, a low quantity of gas bubble discharge could potentially occur in the Haapet Dome area, without being detected.

## **6.2 Glacigenic sediments acting as seal**

Model 1 intend to discuss the possibility of having glacigenic sediments as potential entrapment zones. In several areas (figure 5.17, 5.18 & 5.24), amplitude anomalies are present beneath or adjacent to an URU horizon. From mapping herein, the glacial sediments comprise a maximum thickness of ~42 ms (TWT) in the study area (figure 5.6). The interpreted URU surface (figure 5.5) was mainly identified in the middle parts of the study area, with some overlying and assumed glacial deposits situated on the Haapet Dome (chapter 5.2).

Well 7435/12-1 was drilled through 6 m of glacigenic sediments (NPD, 2017b). Concerning the seismic profiles from figure 5.16B and 5.16F, the adjacent URU reflection was not interpreted at the borehole. This suggests that glacigenic sediments might be present outside where it is seismically mapped, especially given that the vertical resolution at these levels are about 11-12 m (Table 4.2).

The seafloor reflection shows areas of increasing amplitude response (figure 5.15), which are suggested to be the results of tuning effects, due to constructive interference by underlying seismic reflectors. Although, an increase in a discontinuous amplitude reflection, with underlying amplitude anomalies, could also suggest the presence of gas-saturated sediments.



The Upper Regional Unconformity is an erosional surface that encompasses a lithological transition, which could act as a barrier for potential gas migration. Besides, glacigenic deposits are dense and less permeable sediments, which could also act as a functional trapping system for upward gas migration (Tasianas et al., 2016).

### **6.3 Stable gas hydrates acting as seal**

Model 2 intend to discuss the possible existence of stable gas hydrates as potential seals. If a sufficient amount of hydrocarbon gasses (mostly methane) are situated in a marine environment, where high ambient pressure and low temperatures are occurring, hydrates might evolve (Madrussani et al., 2010). Gas hydrates could then act as hydrocarbon barriers, trapping underlying free gas (Paganoni et al., 2016). Madrussani et al. (2010) suggest that gas hydrates might act as areas of reduced permeability, and thus act as vertical barriers.

The study area comprises water depths between 280 m to 460 m and low temperatures (-1°C). Andreassen et al. (2017) estimate that methane hydrates are globally observed at water depths that exceed 300 m with water temperatures of -5°C. Although, if the hydrates were to contain heavier gas components (such as ethane or propane) along with methane, they might occur at shallower depths (Chand et al., 2012).

In areas where a sufficient amount of gas hydrates is stable, a BSR could be observed. However, Paganoni et al. (2016) have previously observed gas hydrates in areas with the absence of a continuous BSR. It has been suggested that the occurrence of a BSR could relate to paleo-pressure and temperature conditions or multiple bases of gas hydrate stability zones (Paganoni et al., 2016).

Considering that no geochemical data regarding the gas composition from well 7435/12-1 was available, well 7226/2-1 and 7324/8-1 was used as an analogue for the identified gas accumulation (Stø Formation) in the Haapet Dome area. As both wells encompass a similar geological setting to the Haapet Dome area, their gas composition was ideal as an analogue. The gas composition from well 7226/2-1 and 7324/8-1 was extracted from Løvaas (2016). Both gas compositions contained heavier gas components that correspond to a stable generation of gas hydrates at shallow stratigraphic depths.

By calculating the gas composition from well 7226/2-1 and 7324/8-1 (figure 4.1), a gas hydrate stability model was generated (figure 4.4). This model comprises three gas hydrate phase boundaries, with distinct chemical compositions. According to theoretical calculations and modelling, the possibility of having gas hydrates present in the study area is possible, given the same gas composition as in exploration well 7226/2-1 and 7324/8-1.

By using well 7226/2-1 and 7324/8-1 as an analogue, a gas hydrate stability zone was expected to reach depths of ~360 m and ~430 m, equivalent of ~415 ms (TWT) and ~470.5 ms (TWT). Given that well 7226/2-1 lies closest to the Haapet Dome area and contains lighter gas components than well 7324/8-1, the gas composition from well 7226/2-1 was mainly used for gas hydrate estimation. If the potential gas composition contained pure methane concentration, no zone of stable gas hydrates would occur.

The potential BSR (figure 6.1 – 6.3) from well 7226/2-1 have been interpreted according to its modelled gas hydrate stability zone. Seismic amplitude anomalies situated above the modelled BSR might suggest the presence of stable gas hydrates (figure 6.1 – 6.3). Figure 6.2B demonstrates a possible scenario where the base of stable gas hydrates could act as an overlying trapping mechanism for free gas.

Ferré et al. (2020) relate that seasonal variations (figure 6.4) might have an impact on the gas hydrate stability zones across the Barents Sea. The arctic continental shelves are characterised as a region of seasonal variations in bottom-water temperatures. During the winter season of May 2016, the hydroacoustic survey presented by Ferré et al. (2020) discovered that cold bottom-water has a negative impact on gas release, (equivalent to a reduction of 43% compared to warmer circumstances) meaning that less amount of gas is released during cold seasons.

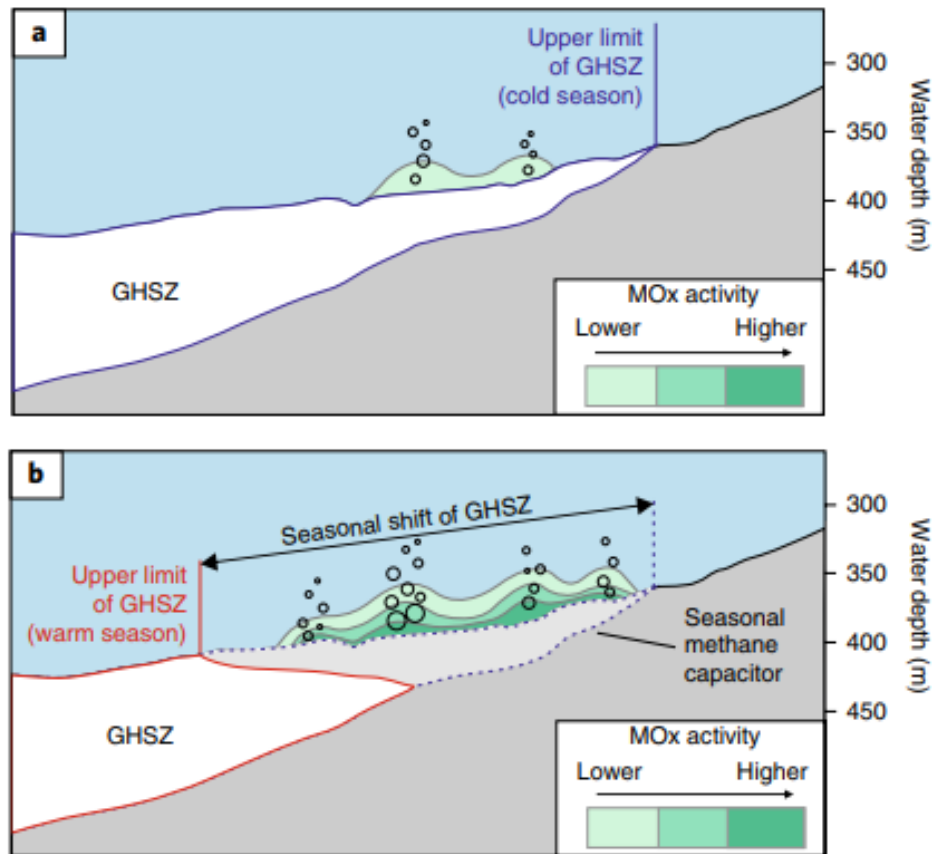


Figure 6.4: Illustration of seasonal variations in relation to methane seepage. (A) Illustrates a cold season scenario, where a strong reduction in methane release is occurring. (B) Displays a warm-season scenario with a substantial increase in methane release. MOx activity = the seep-associated aerobic  $\text{CH}_4$  oxidation rate. The GHSZ was estimated from Berndt et al. (2014). Retrieved from Ferré et al. (2020).

When hydrates are exposed to a decrease in temperature and increase in pressure, their crystalline compound becomes denser and more impermeable. One unit of methane hydrate volume corresponds to  $\sim 160$  unit volumes of gas (Chernov et al., 2017). The analysed water column data was gathered from January to June 2014, which is recognised as a season that comprises cold bottom-water temperatures. The gas hydrates might act as barriers for upwards migration of free gas due to its solid crystalline structure.

On the other hand, Ferré et al. (2020) relate to variation in bottom-water temperatures across the Barents Sea (figure 3.12). The Haapet Dome area shows almost no variation in bottom-water temperatures, suggesting that an almost constant temperature of  $\sim -1$  is occurring annually. No seasonal variation in bottom-water temperatures implies that the GHSZ in the study area, if present, would remain stable. Considering that the annual variation in bottom-water temperature remains constant, gas hydrate dissociation would not occur.

The pilot hole for well 7435/12-1 confirmed no shallow hydrocarbon accumulation above the Hekkingen Formation. However, sample logging was not conducted until depths of 547 m, where above-laying strata were probably not registered (NPD, 2017a). Thus, data regarding the presence of stable gas hydrates from well 7435/12-1 is non-existent.

## 6.4 Geological model

In this thesis, model 3 proposes that the potential gas accumulations (according to the observed seismic anomalies and well 7435/12-1) are assumed to be generated and expelled from a stratigraphic deeper source rock. Deeper gas accumulations, as in well 7435/12-1, could give rise to further remigration to shallower levels, pending the stratigraphic or structural entrapment capacity.

According to Ohm et al. (2008), the Norwegian Barents Sea encompasses several source rock intervals. As stated in chapter 3.3.2, uplift and erosion have resulted in a redistribution of fluids across large distances in the Barents Sea region. Inclusively, the impact of uplift and erosion causes a reduction in temperature, which give rise to the assumption that source rocks are no longer generating hydrocarbons in the affected areas (Ohm et al., 2008). The Bjarmeland Platform is suggested to have been affected by an uplift ranging from 1.5 to 2 km (Henriksen et al., 2011b).

As stated by Henriksen et al. (2011a), four potential source rocks are proposed to be present in the greater Barents Sea, where three of them are situated in the study area. The potential source rock distribution is displayed in figure 6.5. The individual maps are represented by three colours that evaluates their presence. Green colour represents an area of high confidence; yellow colours indicates moderate confidence and red colours implies high risk. The amount of risk is evaluated according to the presence of a source rock (Henriksen et al., 2011a).

The map for the Late Permian source rock (figure 6.5A) shows areas of high confidence and low risk across the study area. At present-day, the source rock is assessed to be over-mature in most areas (figure 6.5D) across the Norwegian Barents Sea (Henriksen et al., 2011a), meaning that the source rock has reached its limits of hydrocarbon generation and expulsion (Al-Areeq, 2018).



The source rocks that comprise the Early to Middle Triassic (figure 6.5B) are by Henriksen et al. (2011a) suggested to be well-developed in the northwestern parts of the Barents Sea. In the study area, the source rock is assumed to have moderate risk regarding its presence. According to present-day maturity modelling, both Early and Middle Triassic (figure 6.5E & 6.5F) source rocks comprise a maturity level that implies oil and gas generation in the basin regions. The Early Triassic source rock is more mature than the Middle Triassic source rock (Henriksen et al., 2011a).

The Late Jurassic source rock is suggested by Henriksen et al. (2011a) to be present across the majority of the Barents Sea shelf (figure 6.5C).

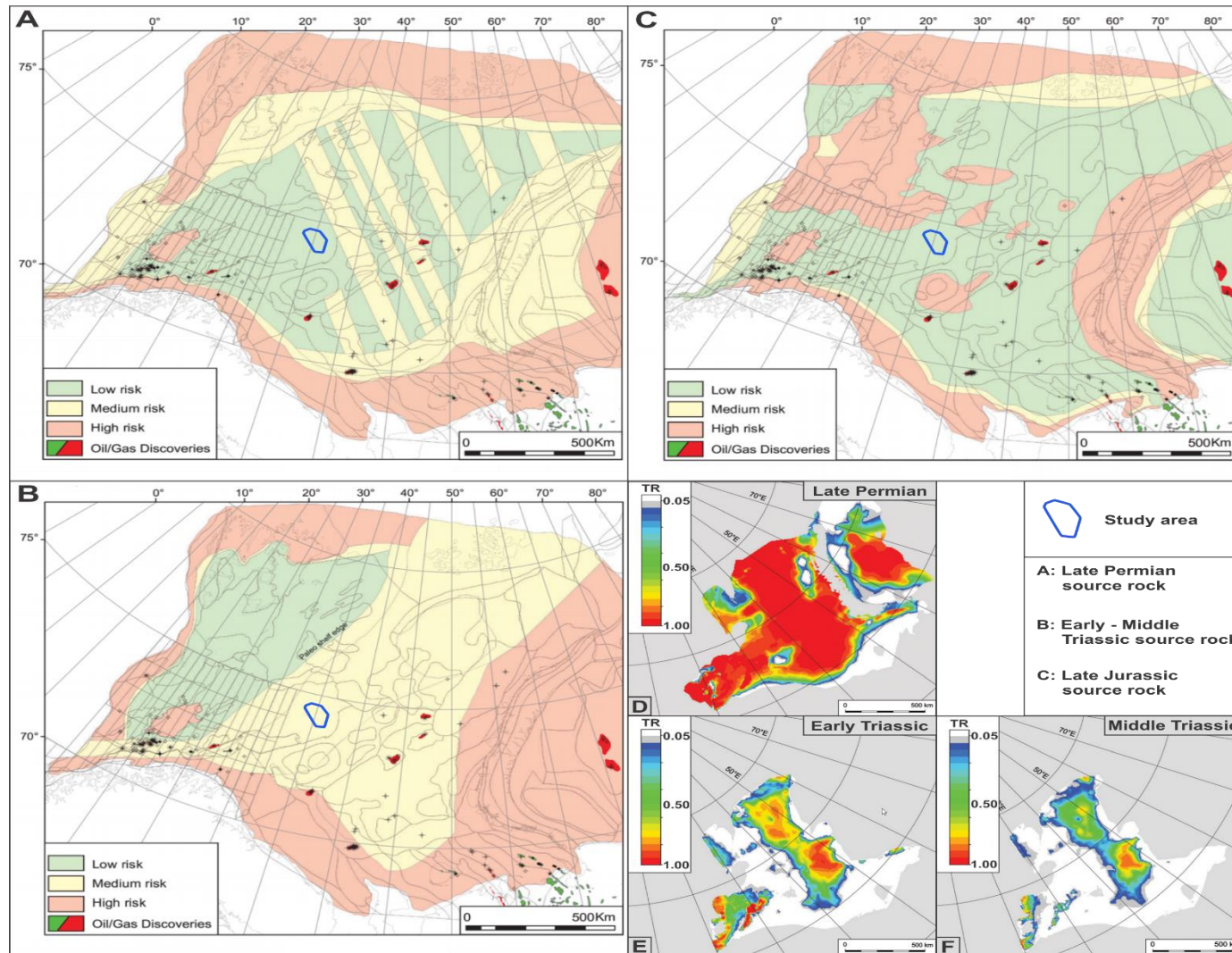


Figure 6.5: A map that displays the distribution of source rocks in the Barents Sea: (A) Late Permian, (B) Early to Middle Triassic and (C) Late Jurassic. Figures (D-F) illustrates the present-day source rock maturity (Transformation ratio: TR) for (D) Late Permian, (E) Early Triassic and (F) Middle Triassic. Modified from Henriksen et al. (2011a).

The possible gas accumulations discussed above could have originated from a long-distance migration beyond the study area. Considering that no geochemical data was available in this study, from well 7435/12-1, the identified gas accumulation could not be directly correlated to a source rock.

The marine shales from the Late Permian suggest good source rock potential (NPD, 2017c). Although, the source rock is estimated to be over-mature, due to its burial depth and high transformation ratio (> 100%), which suggests that the source rock has exceeded the time of significant generation and expulsion of hydrocarbons (Ohm et al., 2008; Henriksen et al., 2011a; Al-Areeq, 2018). Thus, no hydrocarbons are believed to be generated at present-day.

According to Henriksen et al. (2011a), the Early to Middle Triassic source rock could be generating hydrocarbons at present-day, particularly in the north and south Barents basins, including the western parts. Well 7335/3-1 did not discover any potential source rocks of Early to Middle Triassic age (NPD, 2019a). Due to lack of Early to Middle Triassic source rock confirmation in the eastern parts of the Barents Sea, alongside with moderate confidence regarding its existence (Henriksen et al., 2011a), the presence of an Early to Middle Triassic source rock remains uncertain in the Haapet Dome area.

In the study area, the Late Jurassic source rock (the Hekkingen Formation) is situated at a shallow stratigraphic depth (-750 ms to -480 ms in TWT). The consequence of 1.5 to 2 km of uplift caused a reduction in temperature, as mentioned in the previous chapter. Hence, hydrocarbon generation might have ceased (Ohm et al., 2008). Analogue to the geological assessment conducted by NPD (2017c), the Late Jurassic source rock in the Barents Sea North is situated at similar stratigraphic depths. Both study areas are located relatively close by, suggesting that the same Late Jurassic source rock is occurring at both areas. In that case, the source rock is immature at its present depths in the Haapet Dome area (NPD, 2017c). Based on the fact that 1.3 to 2.5 km of sediments were removed, including 1.5 to 2 km of uplift, on the Bjarmeland Platform during the Cenozoic period (Henriksen et al., 2011b; Lasabuda, 2018), could suggest that an earlier hydrocarbon generation from the Late Jurassic source rock might have occurred during the pre-uplift and -erosional stage.

According to the above-discussed source rocks, a conceptual model (figure 6.6A) for the study area was integrated to display how migration pathways could have been working in the area. If the presumed gas accumulations originated from the Permian source rock, the present-day amplitude anomalies would represent earlier generated hydrocarbons, which have since been preserved.

However, as no physical limits might predict the migrational distance for fluids (Schowalter, 1979), the assumed gas accumulations could also be results of re-migrated gas from a distant entrapment zone.

Regarding the uncertainties of an Early to Middle Triassic source rock in the study area, its presence in the model discussed here was not considered. As the primary source rock in the Barents Sea, the Late Jurassic Hekkingen Formation is immature within, and also at a distance from the study area, a conceptual model (figure 6.6A) is presented based on the assumption of a former generating older – potentially Permian source rock.

The well 7435/12-1 encountered gas in the Stø Formation. From chapter 2.3, rapid differential loading of sediments during Triassic time probably affected the suggested Permian source rocks transformation ratio. Exposure of a significant increase in temperature and pressure could have resulted in a complex evolution of its kerogen type. The Permian source rock might have bypassed the earlier stages of the kerogen evolution, thus resulted in a temperature and pressure levels proportional to the characteristics of metagenesis (Selley & Sonnenberg, 2015). Therefore, the Permian source rock might have only generated and expelled gas, implying the absence of heavier hydrocarbon components (liquid) in the study area.

Three major faults are mapped to affect the Permian strata (figure 6.6A). During the Early Cretaceous time, the Permian source rock reached a significant level of maturity, suggesting expulsion of lighter gas components. The three fault structures might have presumably acted as the main pathways for the possible gas accumulations. As the hydrocarbons reached the permeable Stø Formation, the individual accumulation areas might have reached spill-point and thereby resulted in remigration, leaving the remaining gas accumulations behind. Fractured overburden sediments contribute to further vertical migration, where the majority of the hydrocarbons are presumably either trapped by glaciogenic deposits, zones of stable gas hydrates or they have previously leaked from the seafloor into the water column.



For gas seepage to occur from the seafloor, the availability of migrational pathways (e.g. faults) that are connecting an active source rock to the seafloor, is some of the main factors needed to enhance fluid flow and potentially result in gas leakage from the seafloor (Crémière et al., 2018). Additionally, some of the identified gas seepages in the Barents Sea have mainly been in conjunction with either dissociation of gas hydrates (Serov et al., 2017; Ferré et al., 2020) or a combination of gas hydrate dissolution and the presence of an active source rock (Andreassen et al., 2017; Crémière et al., 2018), where both scenarios enhance the probability of gas seepage from the seafloor.

As discussed, the Haapet Dome area is today suggested to comprise an over-mature source rock of Late Permian age. Hence, no hydrocarbon expulsion or generation is occurring at present-day. If gas hydrates are present in the study area, dissociation was estimated not to occur (from chapter 6.3), which additionally reduces the possibility of gas leakage from the seafloor. Compared to the observations mentioned above regarding the identified gas seepage in the Barents Sea, the Haapet Dome area exhibits none of the available factors. Hence, the conducted evaluation might explain why gas leakage is most likely not occurring at present-day in the Haapet Dome area.

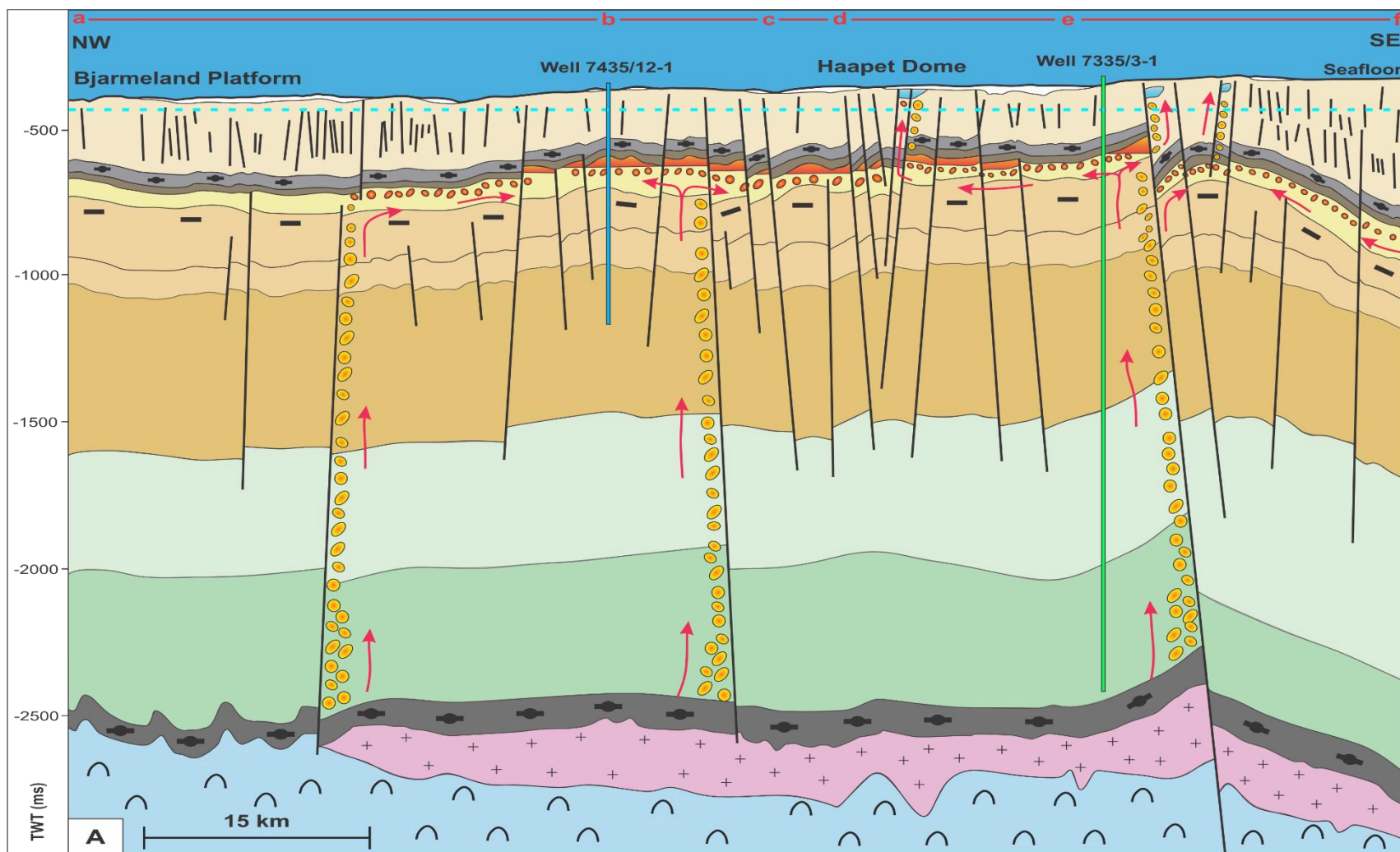


Figure 6.6: (A) An integrated conceptual model illustrating the most likely scenario of a former working petroleum system. Excluding the identified gas accumulation through well 7435/12-1, the remaining accumulations are assumed to be of gas. The legend and the overview of the utilised composite line for the modelled petroleum system are displayed in figure 6.6B and 6.6C. The model was constructed based on seismic observational features, chronostratigraphic and lithostratigraphic diagram from NPD (2017c) and well-data from well 7435/12-1 (blue vertical line) and 7335/3-1 (green vertical line).

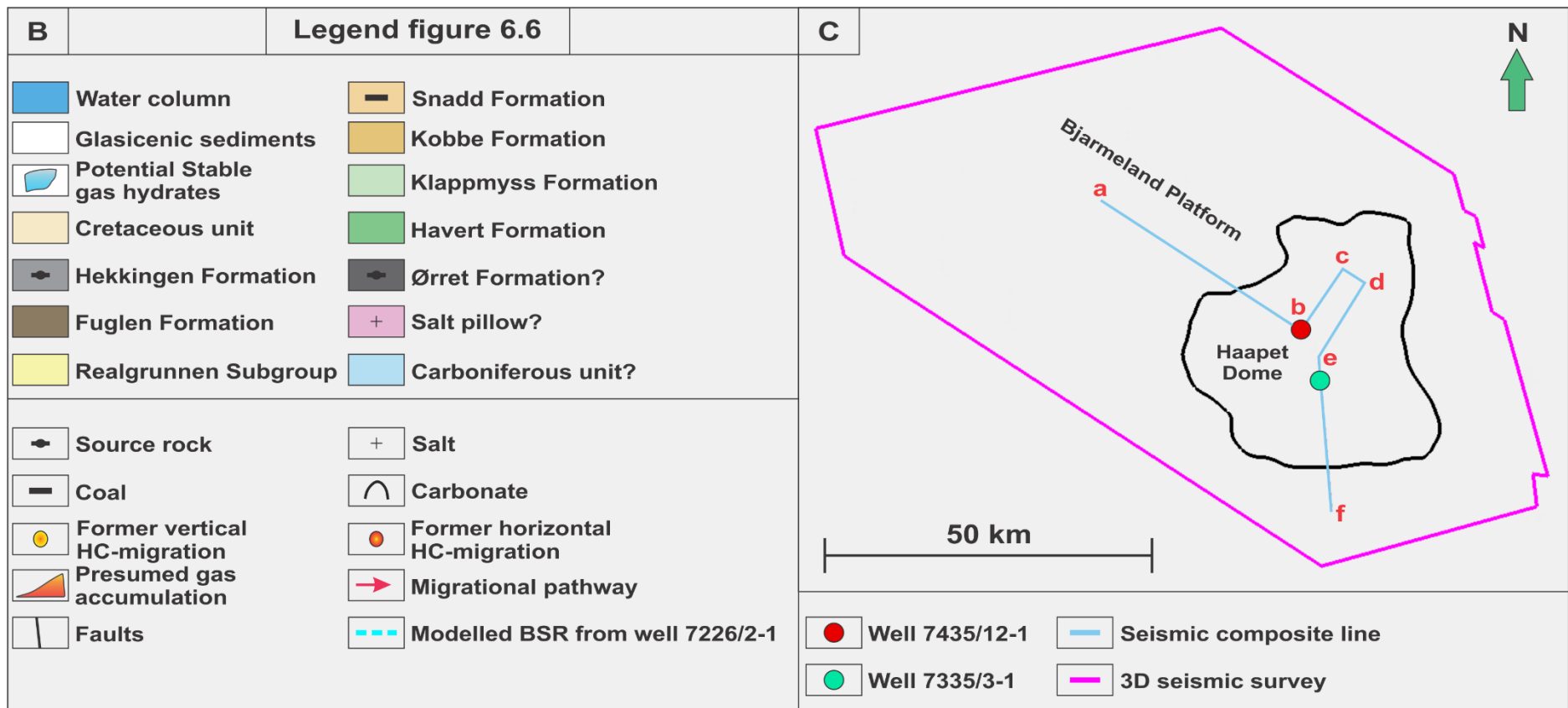


Figure 6.6: (B) Illustrates the legend for the conceptual model in figure 6.6A. Note that there are uncertainties related to the interpreted Ørret Formation, Salt pillow and the Carboniferous unit, due to lack of well-data. HC = Hydrocarbon. (C) Displays the overview of the utilised seismic composite line for figure 6.6A.

## 7 Conclusion

Analysis of seismic 3D data, combined with water column observations from the Haapet Dome area, has provided a detailed assessment of the connection between shallow seismic anomalies and subsurface faulting, along with an evaluation of potential gas release from the seafloor. By integrating the data and observations, potential models for gas migration to and within the Haapet Dome area has been suggested. The main findings are summarized below:

- The study area encompasses shallow amplitude anomalies, which are mainly confined to the Stø Formation and the upper parts of the Cretaceous unit. These amplitude anomalies are assumed to represent shallow accumulations of gas, also calibrated to the identified GWC in well 7435/12-1. The discussed migration models indicate a trend where subsurface faults and permeable carrier beds are suggested to be the controlling factors for possible gas migration.
- A total number of 2192 processed water column lines from the MAREANO program (with a data-volume of ~4.95 TB) was analysed. However, no gas flares were identified in the Haapet Dome area.
- Glacigenic sediments are present in the study area, but might be represented by a thin or discontinuous cover. Where present, these assumed dense, shallow units might represent potential entrapment zones for underlying shallow gas accumulations.
- Modelling of gas hydrate stability zones was conducted based on the gas composition from well 7226/2-1 and 7324/8-1. By using a modelled bottom simulating reflector (BSR) from well 7226/2-1, local zones of potential stable gas hydrates could be estimated. The base of stable gas hydrates might act as hydrocarbon barriers, and cause trapping of underlying accumulations of shallow gas.
- The Late Permian source rock is suggested as the origin of the possible gas accumulations in the study area. Given that the Late Permian source rock (correlative to the Ørret Formation) probably generated hydrocarbons during Early Cretaceous time, but are no longer active (over-mature at present-day), suggests that the observed assumed gas accumulations have been in the system for a significant time. Considering that no present-day hydrocarbon expulsion or gas hydrate dissociation, including the presence of dense lithological seals, was assumed to take place, suggests that potential gas seepage from the seafloor is less unlikely to occur in the Haapet Dome area.



## 8 Future work

This study has led to a better understanding of how the combination of water column imaging, in correlation with shallow amplitude anomalies and faulted strata, might be used to detect possible gas leakage from the seafloor. Further, the combination of data and the application of geological models might contribute to assess the presence of hydrocarbons in the subsurface. Future work might expand this approach:

- Despite having the presence of shallow amplitude anomalies and faults close by the seafloor, gas seepage may still not occur. The Haapet Dome comprises several amplitude anomalies situated beneath the seafloor, correlated with an excellent connection to faults. Some of the water column data illustrated significant acoustic distortion, which complicated the detection of possible gas flares. Future work would be to reduce degraded water column data quality by eliminating unwanted acoustic responses, which would improve the capability of detecting potential gas flares.
- Detecting of gas flares through water column imaging is a relatively new area of research, where the majority of previously published work has focused on locating large quantities of gas seepage across the Norwegian Barents Sea. Future investigation is recommended to analyse the possibility of smaller gas leakage in deep water (>100 m) and focus on understanding their distribution and existence better.
- In order to understand why gas flares were not observed in the water column data in this study, shallow lithological entrapment zones need to be evaluated in the Haapet Dome area. The thesis proposes two potential hydrocarbon seals: Glacigenic sediments and zones of stable gas hydrates. In areas where glacigenic sediments were not identified, zones of stable gas hydrates were suggested to trap underlying free gas. However, the gas hydrates were modelled based on a gas composition from an exploration well ~319 km from the study area. Potential future work could analyse the gas composition from well 7435/12-1, to better indicate if gas hydrates could be stable or not in the study area. If stable gas hydrates might occur, this thus could support gas hydrates being a possible seal in the study area.

## 9 References

- Al-Areeq, N.M. (2018). *Petroleum Source Rocks Characterization and Hydrocarbon Generation*. Recent Insights in Petroleum Science and Engineering, Mansoor Zoveidavianpoor, IntechOpen, DOI: [10.5772/intechopen.70092](https://doi.org/10.5772/intechopen.70092). Acquired: 29.10.2019.
- Allan, U.S. (1989). *Model for hydrocarbon migration and entrapment within faulted structures*. AAPG Bulletin; 73 (7), p. 803-811. DOI: <https://doi.org/10.1306/44B4A271-170A-11D7-8645000102C1865D> Acquired: 11.05.2020.
- Alsadi, H.N. (2017). *The Seismic Reflection Signal*. In: Seismic Hydrocarbon Exploration. Advances in Oil and Gas Exploration & Production. Springer, Cham. DOI: [https://doi.org/10.1007/978-3-319-40436-3\\_8](https://doi.org/10.1007/978-3-319-40436-3_8) Acquired: 30.11.2019.
- Aminzadeh, F. & Dasgupta, S.N. (2013). Chapter 3 – *Fundamentals of Petroleum Geophysics*. Development in Petroleum Science. Vol. 60. p. 37-92. DOI: <https://doi.org/10.1016/B978-0-444-50662-7.00003-2> Acquired: 29.09.2019.
- Andreassen, K., Hubbard, A., Winsborrow, M., Patton, H., Vadakkepuliambatta, S., Plaza-Faverola, A., Gudlaugsson, E., Serov, P., Deryabin, A., Mattingsdal, R., Mienert, J. & Bünz, S. (2017). *Massive blow-out craters formed by hydrate-controlled methane expulsion from the Arctic seafloor*. Science. Vol. 356. Issue 6341, p. 948-953. DOI: [10.1126/science.aal4500](https://doi.org/10.1126/science.aal4500). Acquired: 22.01.2020.
- Berndt, C., Feseker, T., Treude, T., Krastel, S., Liebetrau, V., Niemann, H., Bertics, V.J., Dumke, I., Dünnbier, K., Ferré, B., Graves, C., Gross, F., Hissmann, K., Hühnerbach, V., Krause, S., Lieser, K., Schauer, J. & Steinle, L. (2014). *Temporal constraints on hydrate-controlled methane seepage off Svalbard*. Science 343, p. 284-287. DOI: <https://doi.org/10.1126/science.1246298> Acquired: 05.03.2020.
- Brown, A.R. (1992). *Interpretation of three-dimensional seismic data*. Third edition. AAPG Memoir 42. Tulsa, Oklahoma: American Association of Petroleum geologists. ISBN-10: 0891813314.
- Bryant, W.A. (2016). *Fault*. In: Bobrowsky P.T. (eds) Encyclopedia of Natural Hazards. Encyclopedia of Earth Sciences Series. Springer, Dordrecht. DOI: [https://doi.org/10.1007/978-1-4020-4399-4\\_132](https://doi.org/10.1007/978-1-4020-4399-4_132) Acquired: 12.10.2019.
- Chand, S., Thorsnes, T., Rise, L., Brunstad, H., Stoddart, D., Bøe, R., Lågstad, P. & Svolsbru, T. (2012). *Multiple episodes of fluid flow in the SW Barents Sea (Loppa High) evidenced by gas flares, pockmarks and gas hydrate accumulation*. Elsevier. Earth and Planetary Science letters. Vol. 331-332, p. 305-314. DOI: <https://doi.org/10.1016/j.epsl.2012.03.021> Acquired: 24.01.2020.
- Chernov, A.A., Pil'nik, A.A., Elistratov, D.S., Mezentsev, I.V., Meleshkin, A.V., Bartashevich, M.V. & Vlasenko M.G. (2017). *New hydrate formation methods in a liquid-gas medium*. Sci Rep 7, 40809. DOI: <https://doi.org/10.1038/srep40809> Acquired: 08.02.2020.

- Chopra, S., Castagna, J. & Portniaguine, O. (2006). *Seismic resolution and thin-bed reflectivity inversion*. Arcis Corporation, Calgary; Fusion Petroleum Technologies, Inc., Houston. University of Houston. Retrieved from: [http://www.chopraseismic.com/wp-content/uploads/2015/09/THINS.R.thin-bed.hr\\_.pdf](http://www.chopraseismic.com/wp-content/uploads/2015/09/THINS.R.thin-bed.hr_.pdf) Acquired: 29.09.2019.
- Clarke, H. (2006). *Applications of multibeam water column imaging for hydrographic survey*. Hydrogr.J.120. Retrieved from: [https://www.researchgate.net/publication/228650988\\_Applications\\_of\\_multibeam\\_water\\_column\\_imaging\\_for\\_hydrographic\\_survey](https://www.researchgate.net/publication/228650988_Applications_of_multibeam_water_column_imaging_for_hydrographic_survey) Acquired: 22.01.2020.
- Crémière, A., Chand, S., Sahy, D., Thorsnes, T., Martma, T., Noble, S.R., Pedersen, J.H., Brunstad, H. & Lepland, A. (2018). *Structural controls on seepage of thermogenic and microbial methane since the last glacial maximum in the Harstad Basin, southwest Barents Sea*. Vol. 98, p. 569-581. DOI: <https://doi.org/10.1016/j.marpetgeo.2018.07.010> Acquired: 22.01.2020.
- Dalland, A., Worsley, D. & Ofstad, K. (1988). *A lithostratigraphic scheme for the Mesozoic and Cenozoic succession offshore mid- and northern Norway*. NPD-Bulletin No. 4, 65 pp. Retrieved from: <https://www.npd.no/globalassets/1-mpd/publikasjoner/npd-bulletins/npd-bulletin-4-1988.pdf> Acquired: 28.02.2020.
- Dellmour, R., Stueland, E., Lindstrom, S. & Tari, G. (2016). *The Haapet Dome in the Norwegian Barents Sea structural evolution and morphometry of salt basins*. OMV E&P, Vienna, Austria. DOI: 10.3997/2214-4609.201601647. Acquired: 05.09.2019.
- England, W.A., Mackenzie, A.S., Mann, D.M. & Quigley, T.M. (1987). *The movement and entrapment of petroleum fluids in the subsurface*. Journal of the Geological Society, London, Vol. 144, p. 327-347. Retrieved from: <http://citeseerx.ist.psu.edu/viewdoc/download?doi=10.1.1.453.5516&rep=rep1&type=pdf> Acquired: 03.11.2019.
- Fajana, A.O., Ayuk, M.A., Enikanselu, P.A. & Oyebamiji, A.R. (2019). *Seismic interpretation and petrophysical analysis for hydrocarbon resource evaluation of “Pennay” field, Niger Delta*. Journal of Petroleum Exploration and Production Technology 9, p. 1025-1040. DOI: <https://doi.org/10.1007/s13202-018-0579-4> Acquired: 11.05.2020.
- Faleide, J.I., Bjørlykke, K. & Gabrielsen, R.H. (2010). *Geology of the Norwegian Continental Shelf*. Chapter 22. Petroleum of Geosciences, Department of Geosciences, University of Oslo. p. 467-499. DOI: 10.1007/978-3-642-02332-3\_22. Acquired: 29.08.2019.
- Ferré, B., Jansson, P.G., Moser, M., Serov, P., Portnov, A., Graves, C.A., Panieri, G., Gründger, F., Berndt, C., Lehmann, M.F. & Niemann, H. (2020). *Reduced methane seepage from Arctic sediments during cold bottom-water conditions*. Nat. Geosci. DOI: <https://doi.org/10.1038/s41561-019-0515-3> Acquired: 24.01.2020.
- Fossen, H. & Bale, A. (2007). *Deformation bands and their influence on fluid flow*. The American Association of Petroleum Geologists. AAPG Bulletin, V.91, NO.12. p. 1685-1700. Retrieved from: 10.1306/07300706146. Acquired: 12.10.2019.

- Gee, D.G. & Pease, V. (2004). *The Neoproterozoic Timanide Orogen of eastern Baltica*. Uppsala University. Stockholm University. Department of Geosciences. Memoirs, 30, p. 1-3. Retrieved from: <https://mem.lyellcollection.org/content/memoirs/30/1/1.full.pdf> Acquired: 27.08.2019.
- Gentz, T., Damm, E., Schneider von Deimling, J., Mau, S., McGinnis, D.F. & Schlüter, M. (2014). *A water column study of methane around gas flares located at the West Spitsbergen continental margin*. *Continental Shelf Research*. Vol. 72, p. 107-118. DOI: <https://doi.org/10.1016/j.csr.2013.07.013> Acquired: 01.03.2020.
- Gogoi, M. & Ghosh, G.K. (2017). *Interpretation of Seismic data for thrust/fault identification using variance and inverse of variance attribute analysis*. *J.Ind. Geophys. Union*. Vol. 21, no. 6, p 500-509. Retrieved from: [https://www.researchgate.net/publication/320833893\\_Interpretation\\_of\\_Seismic\\_data\\_for\\_thrustfault\\_identification\\_using\\_variance\\_and\\_inverse\\_of\\_variance\\_attribute\\_analysis](https://www.researchgate.net/publication/320833893_Interpretation_of_Seismic_data_for_thrustfault_identification_using_variance_and_inverse_of_variance_attribute_analysis) Acquired: 11.12.2019.
- Hassaan, M., Faleide, J.I., Gabrielsen, R.H. & Tsikalas, F. (2019). *Carboniferous graben structures, evaporite accumulations and tectonic inversion in the southeastern Norwegian Barents Sea*. *Marine and Petroleum geology*. Elsevier Ltd. DOI: <https://doi.org/10.1016/j.marpetgeo.2019.104038> Acquired: 11.09.2019.
- Henriksen, E., Ryseth, A.E., Larssen, G.B., Heide, T., Rønning, K., Sollid, K. & Stoupakova, A.V. (2011a). *Tectonostratigraphy of the greater Barents Sea: implications for petroleum systems*. Chapter 10. *Arctic Petroleum Geology*. Geological Society, London, memoirs, 35, p. 163-195. DOI: 10.1144/M35.10. Acquired: 12.09.2019.
- Henriksen, E., Bjørnseth, H.M., Hals, T.K., Heide, T., Kiryukhina, T., Kløvjan, O.S., Larssen, G.B., Ryseth, A.E., Rønning, K., Sollid, K. & Stoupakova, A. (2011b). *Uplift and erosion of the greater Barents Sea: impact on prospectivity and petroleum systems*. Chapter 17. *Arctic Petroleum Geology*. Geological Society, London, Memoirs, 35, p. 271-281. DOI: 10.1144/M35.17. Acquired: 02.12.2019.
- Hjelstuen, O.B., Haflidason, H., Sejrup, P.H. & Nygård, A. (2010). *Sedimentary and structural control on pockmark development – Evidence from the Nyegga pockmark field, NW European margin*. *Geo-Marine Letters*. 30. p. 221-230. DOI: 10.1007/s00367-009-0172-4. Acquired: 31.01.2020.
- Kearey, P., Brooks, M. & Hill, I. (2002). *An introduction to geophysical exploration*. Third edition. Blackwell science Ltd. p. 1-257. Retrieved from: <https://pdfs.semanticscholar.org/c2aa/cef07bc320ffff2c5f2df807f3a087d5ed3c.pdf> Acquired: 28.09.2019.
- Koson, S., Chenrai, P. & Choowong, M. (2014). *Seismic attributes and their application in seismic geomorphology*. *Seismic attributes and seismic geomorphology*. *Bulletin of earth sciences of Thailand*. Vol. 6, No. 1, p. 1-9. Retrieved from: <https://pdfs.semanticscholar.org/10fb/fac995179338806fe40bd79eb6be25e3cd8f.pdf> Acquired: 24.01.2020.



- Kovacs, Z. & Zilahi-Sebess, L. (2018). *Evaluation of the trends of secondary and tertiary hydrocarbon migration processes based on oil density-reservoir depths relationship in Hungary*. Central European geology. DOI: 10.1556/24.61.2018.02. Acquired: 02.11.2019.
- Larsen, E., Andreassen, K., Nilssen, L.C. & Raunholm, S. (2003). *The prospectivity of the Barents Sea: Ice ages, erosion and tilting of traps*. Geological Survey of Norway, N-7491 Trondheim, Norway. Department of Geology, University of Tromsø. p. 1-57. Retrieved from: [https://www.ngu.no/upload/Publikasjoner/Rapporter/2003/2003\\_102.pdf](https://www.ngu.no/upload/Publikasjoner/Rapporter/2003/2003_102.pdf) Acquired: 23.09.2019.
- Larsen, G.B., Elvebakk, G., Henriksen, L.B., Kristensen, S., Nilsson, I., Samuelsberg, T.J., Svånå, T.A., Stemmerik, L. & Worsley, D. (2002). *Upper Palaeozoic lithostratigraphy of the southern Norwegian Barents Sea*. Geological setting. <http://www.npd.no/Norsk/Produkter+og+tjenester/Publikasjoner/Oversikt+sokkelpublikasjoner/npd+bulletin.htm>. 76 pp., 63 figs., 1 tbl. Retrieved from: <http://www.nhm2.uio.no/norges/litho/Barents/intro/geology.html> Acquired: 27.08.2019.
- Lasabuda, A.P.E. (2018). *Cenozoic tectonosedimentary development and erosion estimates for the Barents Sea continental margin, Norwegian Arctic*. Faculty Science and technology, Department of geosciences. Retrieved from: <https://munin.uit.no/handle/10037/12800> Acquired: 02.12.2019.
- Løvaas, J.S. (2016). *Possible gas hydrates on the Bjarmeland Platform; seismic expression and stability modelling*. Faculty of Science and Technology. Department of Geology. Retrieved from: <https://munin.uit.no/handle/10037/9376> Acquired: 26.01.2020.
- Madrussani, G., Rossi, G. & Camerlenghi, A. (2010). *Gas hydrates, free gas distribution and fault pattern on the west Svalbard continental margin*. Geophysical Journal International, Volume 180, Issue 2, p. 666-684. DOI: <https://doi.org/10.1111/j.1365-246X.2009.04425.x> Acquired: 24.01.2020.
- Magoon, L.B. & Beaumont, E.A. (2003). *Petroleum systems*. Chapter 3. Search and Discovery article #40068. Defining a petroleum system. p. 3-34. Retrieved from: <http://www.searchanddiscovery.com/documents/beamont02/> Acquired: 02.10.2019.
- Magoon, L.B. & Dow, W.G. (1994). *The petroleum system*. In L.B. Magoon and W.G. Dow, eds., *The Petroleum System – From Source to Trap: AAPG Memoir 60*, p. 3-24. DOI: <https://doi.org/10.1306/M60585> Acquired: 02.10.2019.
- Jansson, P. (2018). *Methane bubbles in the Arctic Ocean*. Quantification, variability analysis and modelling of free and dissolved methane from the seafloor to the atmosphere. Faculty of Science and Technology. Retrieved from: <https://munin.uit.no/handle/10037/14485> Acquired: 04.03.2020.

- Jensen, B.K.H., Bjarnadóttir, R.L. & Faust, J. (2015). *Pockmark i Barentshavet*. Mareano. Norges Geologiske Undersøkelser. Retrieved from: [https://mareano.no/nyheter/nyheter\\_2015/pockmark-i-barentshavet](https://mareano.no/nyheter/nyheter_2015/pockmark-i-barentshavet) Acquired: 31.01.2020.
- Mareano. (2014). *MAREANO program*. Water column data (WCD). Acquired by the Kongsberg Maritime Service from January to June 2014.
- Mareano. (2017). *Data sets, products and methods used for map production in Mareano by NGU – Current status*. Water column data. Retrieved from: [https://www.mareano.no/resources/files/om\\_mareano/arbeidsmater/NGU\\_MAREANO\\_map\\_production\\_methods.pdf](https://www.mareano.no/resources/files/om_mareano/arbeidsmater/NGU_MAREANO_map_production_methods.pdf) Acquired: 22.01.2020.
- Martel, S.J. (1990). *Formation of compound strike-slip fault zones, Mount Abbot quadrangle, California*. Earth Sciences Division. University of California. Journal of structural Geology. Vol. 12, No. 7, p.869-882. Retrieved from: [http://www.soest.hawaii.edu/martel/Martel.pubs.pdf/Martel\\_1990.pdf](http://www.soest.hawaii.edu/martel/Martel.pubs.pdf/Martel_1990.pdf) Acquired: 12.10.2019.
- Mattingsdal, R., Høy, T., Simonstad, E. & Brekke, H. (2015). *An updated map of structural elements in the southern Barents Sea*. Haapet Dome. NPD. Geological Winter Meeting, Stavanger. Retrieved from: <https://www.npd.no/globalassets/1-npd/fakta/geologi-norsk/strukturelementer/poster-nye-strukturelementer-bhso.pdf> Acquired: 02.09.2019.
- Mau, S., Römer, M., Torres, M.E., Bussmann, I., Pape, T., Damm, E., Geprägs, P., Wintersteller, P., Hsu, C.-W., Loher, M. & Bohrmann, G. (2017). *Widespread methane seepage along the continental margin off Svalbard – from Bjørnøya to Kongsfjorden*. Sci. Rep. 7, 42997; DOI: 10.1038/srep42997. Acquired: 22.01.2020.
- McKerrow, W.S., Niocaill, C.M. & Dewey, J.F. (2000). *The Caledonian Orogeny redefined*. Department of Earth Sciences, University of Oxford, Vol. 157, p. 1149-1154. Retrieved from: <https://www.earth.ox.ac.uk/~conallm/Caled.pdf> Acquired: 29.08.2019.
- Micallef, A. (2011). *Development in Earth Surface Processes*. Chapter 13 – Marine geomorphology: Geomorphological mapping and the study of submarine landslides. Vol 15, p. 377-395. DOI: <https://doi.org/10.1016/B978-0-444-53446-0.00013-6> Acquired: 26.09.2019
- Nanda, N.C. (2016). *Direct Hydrocarbon Indicators (DHI)*. In: Seismic Data Interpretation and Evaluation for Hydrocarbon Exploration and Production. Springer, Cham. DOI: [https://doi.org/10.1007/978-3-319-26491-2\\_6](https://doi.org/10.1007/978-3-319-26491-2_6) Acquired: 16.11.2019.
- NP. (2019). *Activity per Sea Area*. Norwegian Petroleum. Development and Operations. Barents Sea. Retrieved from: <https://www.norskpetroleum.no/en/developments-and-operations/activity-per-sea-area/> Acquired: 05.11.2019.

- NPD. (2017a). Fact pages. Norwegian Petroleum Directorate. *General information*. Discovery wellbore, 7435/12-1. Operations and results. Retrieved from: [https://factpages.npd.no/ReportServer\\_npdpublic?/FactPages/PageView/discovery&rc:Command=Render&rc:Toolbar=false&rc:Parameters=f&NpdId=29491696&IpAddress=172.16.1.82&CultureCode=en](https://factpages.npd.no/ReportServer_npdpublic?/FactPages/PageView/discovery&rc:Command=Render&rc:Toolbar=false&rc:Parameters=f&NpdId=29491696&IpAddress=172.16.1.82&CultureCode=en) Acquired: 07.10.2019.
- NPD. (2017b). Fact pages. Norwegian Petroleum Directorate. *Lithostratigraphy of the Naust Fm.* Retrieved from: <http://factpages.npd.no/FactPages/Default.aspx?nav1=wellbore&nav2=PageView|Exploration|All&nav3=8228&culture=en> Acquired: 20.09.2019.
- NPD. (2017c). Fact pages. Norwegian Petroleum Directorate. *Geological assessment of petroleum resources in the eastern part of Barents Sea North 2017*. Retrieved from: <https://www.npd.no/globalassets/1-npd/publikasjoner/rapporter-en/geologivurderingbhn-engelsk-lavoppl.pdf/> Acquired: 26.11.2019.
- NPD. (2017d). Fact pages. Norwegian Petroleum Directorate. *Press release well 7435/12-1*. Retrieved from: <https://www.npd.no/en/facts/news/Exploration-drilling-results/2017/743512-1/>. Acquired: 07.05.2020.
- NPD. (2019a). Fact news. Norwegian Petroleum Directorate. Exploration drilling results. *Dry well near the 7435/12-1 (Korpfjell) gas discovery in the Barents Sea – 7335/3-1*. Retrieved from: <https://www.npd.no/en/facts/news/Exploration-drilling-results/2019/dry-well-near-the-743512-1-korpfjell-gas-discovery-in-the-barentssea-73353-1/> Acquired: 07.10.2019.
- NPD. (2019b). Fact pages. Norwegian Petroleum Directorate. *Resource accounts at 31 December 2018*. Retrieved from: <https://www.npd.no/en/facts/resource-accounts-and-analysis/resource-accounts-at-31-december-2018/> Acquired: 05.11.2019.
- NPD. (2019c). Fact pages. Norwegian Petroleum Directorate. Retrieved from: <https://factpages.npd.no/factpages/default.aspx?nav1=survey&nav2=PageView|Finished|2014&nav3=8038&culture=nb-no> Acquired: 28.11.2019.
- Ohm, S.E., Karlsen, D.A. & Austin, T.J.F. (2008). *Geochemically driven exploration models in uplifted areas: Examples from the Norwegian Barents Sea*. AAPG Bulletin. Vol. 92, No. 9, p. 1191-1223. DOI: 10.1306/06180808028. Acquired: 22. 01.2020.
- Onajite, E. (2014). *Understanding Reflection Coefficient. Seismic Data Analysis Techniques in hydrocarbon Exploration – Chapter 14*. p. 213-228. DOI: <https://doi.org/10.1016/B978-0-12-420023-4.00014-9> Acquired: 18.11.2019.
- Ottesen, D., Rise, L., Andersen, E.S., Bugge, T. & Eidvin, T. (2009). *Geological evolution of the Norwegian continental shelf between 61°N and 68°N during last 3 million years*. Norwegian Journal of Geology Vol. 89, p. 251-265. Retrieved from: [https://www.geologi.no/images/NJG\\_articles/NGT\\_4\\_09\\_Ottesen\\_scr.pdf](https://www.geologi.no/images/NJG_articles/NGT_4_09_Ottesen_scr.pdf) Acquired: 23.09.2019.
- Paganoni, M., Cartwright, J.A., Foschi, M., Shipp, R.C. & van Rensbergen, P. (2016). *Structure 2 gas hydrates found below the bottom-simulating reflector*, *Geophys. Res. Lett.*, 43, p. 5696-5706. DOI: [10.1002/2016GL069452](https://doi.org/10.1002/2016GL069452). Acquired: 07.02.2020.

- Pang, X., Jiang, Z., Zuo, S. & Lerche, I. (2006). *Dynamics of Hydrocarbon Expulsion from Shale Source Rocks*. Energy Exploration & Exploitation. Volume 23. Number 5, p. 333-356. DOI: 10.1260/014459805775992735. Acquired: 31.10.2019.
- Plaza-Faverola, A., Vadakkepuliambatta, S., Hong, W.-L., Mienert, J., Bünz, S., Chand, S., Greinert, J. (2017). *Bottom-simulating reflector dynamics at Arctic thermogenic gas provinces: An example from Vestnesa Ridge, offshore west Svalbard*. Journal of Geophysical Research: Solid Earth / Volume 122, Issue 6, p. 4089-4105. DOI: <https://doi.org/10.1002/2016JB013761> Acquired: 14.03.2020.
- Rafaelsen, B., Andreassen, K., Kuilman, W.L., Lebesbye, E., Hogstad, K. & Midtbø, M. (2002). *Geomorphology of buried glacial horizons in the Barents Sea from three-dimensional seismic data*. In dowdeswell, J.A. and O’Cofaigh, C., (eds): Glacier-influenced sedimentation on high-latitude continental margins. Geological Society of London. Special Publication 203, p. 259-276. DOI: <https://doi.org/10.1144/GSL.SP.2002.203.01.14> Acquired: 28.09.2019.
- Rajput, S. & Naresh, T.K. (2016). *Geological controls for gas hydrates and unconventional*. Chapter 2: Generation of Methane in Earth. Elsevier. ISBN: 978-0-12-802020-3, p. 1-384. DOI: <https://doi.org/10.1016/C2014-0-00998-7> Acquired: 24.01.2020.
- Rey, P.F. (2016). *Introduction to Structural Geology*. Edition 1.1, Isbn: BSIAC. The University of Sidney. Retrieved from: <https://www.researchgate.net/publication/299135987> Introduction to Structural Geology Acquired: 12.10.2019.
- Rise, L., Bellec, K.V., Chand, S. & Bøe, R. (2015). *Pockmarks in the southwestern Barents Sea and Finnmark fjords*. Norwegian Journal of Geology, Vol. 94, p. 263-282. ISSN 029-196X. Retrieved from: [http://njg.geologi.no/images/NJG\\_articles/NJG4\\_Vol94\\_4\\_Rise\\_Scr.pdf](http://njg.geologi.no/images/NJG_articles/NJG4_Vol94_4_Rise_Scr.pdf) Acquired: 31.01.2020.
- Roden, R., Smith, T.A., Santogrossi, P., Sacrey, D. & Jones, G. (2017). *Seismic interpretation below tuning with multiattribute analysis*. The Leading Edge, 36 (4), p. 330-339. DOI: [10.1190/tle36040330.1](https://doi.org/10.1190/tle36040330.1). Acquired: 04.04.2020.
- Schowalter, T.T. (1979). *Mechanics of Secondary Hydrocarbon Migration and Entrapment*. AAPG Bulletin, Volume 63, Issue 5, p. 723-760. DOI: <https://doi.org/10.1306/2F9182CA-16CE-11D7-8645000102C1865D> Acquired: 31.10.2019.
- Selley, R.C. & Sonnenberg, S.A. (2015). *Elements of petroleum geology*. 3rd edition. San Diego, Calif: Academic Press. ISBN: 9780123860323.
- Semb, P.H. (2009). *Possible seismic hydrocarbon indicators in offshore Cyprus and Lebanon*. GeoArabia; 14 (2). p. 49-66. Retrieved from: <https://pubs.geoscienceworld.org/geoarabia/article/14/2/49/566936/possible-seismic-hydrocarbon-indicators-in> Acquired: 16.11.2019.



- Serov, P., Vadakkepuliambatta, S., Mienert, J., Patton, H., Portnov, A., Silyakova, A., Panieri, G., Carroll, M.L., Carroll, J., Andreassen, K. & Hubbard, A. (2017). *Postglacial response of Arctic Ocean gas hydrates to climatic amelioration*. Proceedings of the National Academy of Sciences, 114 (24) 6215-6220; DOI: <https://doi.org/10.1073/pnas.1619288114> Acquired: 22.01.2020.
- Sheriff, R.E. (2002). *Encyclopedia Dictionary of Applied Geophysics*. Society of Exploration Geophysicists. Fourth edition. Series 13. ISBN: 9781560802969.
- Singh, J. (2019). *Bulk Modulus of Gases*. Inspired by Dr.H.C.Verma. Retrieved from: <https://www.concepts-of-physics.com/thermodynamics/bulk-modulus-of-gases.php> Acquired: 17.11.2019.
- Sloan, E.D. (1998). *Hydrate prediction program: HYDOFF*. Accompanying the hydrate engineering handbook. Department of chemical and petroleum-refining engineering.
- Smelror, M., Petrov, O.V., Larssen, G.B. & Werner, S. (2009). ATLAS. *Geological history of the Barents Sea*. Geological Survey of Norway. p. 9-125. ISBN 978-82-7385-137-6.
- Stone, P. (2012). *The demise of the Iapetus Ocean as recorded in the rocks of southern Scotland*. University geological society journal. Vol. 33, p. 29-36. Retrieved from: <http://nora.nerc.ac.uk/id/eprint/21239/1/OU-SU-2011-Text2.pdf>. Acquired: 02.05.2020.
- Tasianas, A., Martens, I., Bünz, S. & Mienert, J. (2016). *Mechanisms initiating fluid migration at Snøhvit and Albatross fields, Barents Sea*. Arktos 2, 26. DOI: <https://doi.org/10.1007/s41063-016-0026-z> Acquired: 05.02.2020.
- Terry, R.E. & Rogers, B.J. (2014). *Applied Petroleum Reservoir Engineering*. Third edition. Chapter 1. Introduction to Petroleum Reservoir and Reservoir Engineering. Prentice hall. Retrieved from: <http://www.informit.com/articles/article.aspx?p=2241145> Acquired: 31.10.2019.
- Urban, P., Köser, K. & Greinert, J. (2017). *Processing of multibeam water column image data for automated bubble/seep detection and repeated mapping*. Limnol. Oceanogr. Methods, 15. p. 1-21. DOI: <https://doi.org/10.1002/lom3.10138> Acquired: 22.01.2020.
- Veeken, P.C.H. (2007). *Seismic stratigraphy, basin analysis and reservoir characterisation*. First edition. Vol. 37, Elsevier. ISBN-13: 978-0-08-045311-8.
- Veloso, M., Greinert J., Mienert, J. & De Batist, M. (2015). *A new methodology for quantifying bubble flow rates in deep water using splitbeam echosounders: Examples from the Arctic offshore NW-Svalbard*. Limnology and oceanography. Methods, 13. Association for the Sciences of Limnology and Oceanography. p. 267-287. DOI: <https://doi.org/10.1002/lom3.10024> Acquired: 04.03.2020.
- Vorren, T.O., Landvik, J.Y., Andreassen, K. & Laberg, J.S. (2011). *Quaternary glaciations – Extent and chronology*. Development in Quaternary sciences. Vol. 15, p. 361-372. ISBN: 9780444535375. Acquired: 23.09.2019.

- Vrolijk, P.J., Urai, J.L. & Kettermann, M. (2016). *Clay smear: Review of mechanisms and applications*. Elsevier. Journal of structural geology. Vol. 86, p. 95-152. DOI: <https://doi.org/10.1016/j.jsg.2015.09.006>. Acquired: 28.04.2020.
- Walters, C.C. (2007). *The Origin of Petroleum*. Chapter 2. Kerogen Formation and the generative potential of source rock. ExxonMobil research & Engineering Co. Annandale, p. 79-101. DOI: 10.1007/978-0-387-25789-1\_2. Acquired: 07.10.2019.
- Wiley, J. & Sons. (2011). *Seismic reflection*. Chapter 12. Fourth edition. Field Geophysics. ISBN: 978-0-470-74984-5. Retrieved from: <https://onlinelibrary.wiley.com/doi/pdf/10.1002/9780470972311.ch12> Acquired: 28.09.2019.
- Worden, R.H., Armitage, P.J., Butcher, A.R., Churchill, J.M., Csoma, A.E., Hollis, C., Lander, R.H. & Omma, J.E. (2018). *Petroleum reservoir quality prediction: overview and contrasting approaches from sandstone and carbonate communities*. Geological Society, London, Special Publications. 435. DOI: 10.1144/SP435.21. Acquired: 31.10.2019.
- Yang, D. & Xu, W. (2007). *Effects of salinity on methane gas hydrate system*. Sci China Ser D-Earth Sci. Volume 50, No. 11, p. 1733-1745. DOI: [10.1007/s11430-007-0126-5](https://doi.org/10.1007/s11430-007-0126-5) Acquired: 24.01.2020.
- Zhao, J-Z., Li, J., Wu, W-T., Cao, Q., Bai, Y-B. & Er, C. (2018). *The petroleum system: a new classification scheme based on reservoir qualities*. Petroleum Science. 16. DOI: 10.1007/s12182-018-0286-2. Acquired: 02.11.2019.
- Zhao, J., Meng, J., Zhang, H. & Wang, S. (2017). *Comprehensive Detection of Gas plumes from Multibeam Water Column Images with Minimization of Noise Interferences*. Sensors 2017, 17, 2755. DOI: <https://doi.org/10.3390/s17122755> Acquired: 21.11.2019.

# 10 Appendices

## 10.1 Appendix 1 – Equations

### Equation 4.1 – Acoustic impedance

$$Z = \rho v$$

Where  $\rho$  = density ( $\text{kg/m}^3$ ) and  $v$  = velocity.

### Equation 4.2 – Reflection coefficient

$$R = \frac{(Z_2 - Z_1)}{(Z_2 + Z_1)} = \frac{(\rho_2 v_2 - \rho_1 v_1)}{(\rho_2 v_2 + \rho_1 v_1)}$$

Where  $Z_1$  (acoustic impedance),  $\rho_1$  (density) and  $v_1$  (velocity) display the overlying layer, while  $Z_2$  (acoustic impedance),  $\rho_2$  (density) and  $v_2$  (velocity) display the underlying layer.

### Equation 4.3 – Seismic wavelength

$$\lambda = \frac{v}{f}$$

Where  $\lambda$  = seismic wavelength (m),  $v$  = seismic velocity (m/s) and  $f$  = frequency (Hz).

### Equation 4.4 – Vertical resolution

$$V_r = \frac{\lambda}{4}$$

Where  $V_r$  = vertical resolution (m) and  $\lambda$  = wavelength (m).

### Equation 4.5 – Unmigrated horizontal resolution

$$R_f = \frac{v}{2} \sqrt{\frac{t}{f}}$$

$R_f$  = the radius of the Fresnel zone (m),  $v$  = average seismic velocity (m/s),  $t$  = two-way travel time (s) and  $f$  = dominant frequency (Hz).

## 10.2 Appendix 2 – Processed water column data

Folders	Processed WCD cells	Amount of processed WCD lines	Date gathered	Size (GB)	Sensor model
1	D04	4163 – 4440 4444 – 4501 4522 – 4629  Total WCD lines: 441	January– Mars 2014	1007.69	Kongsberg 2040
2	D05	6626 – 6696 6700 – 6932  Total WCD lines: 302	June 2014	667.3	Kongsberg 2040
3	D06	4630 – 4946  Total WCD lines: 316	Mars – April 2014	743	Kongsberg 2040
4	D07	6242 – 6625  Total WCD lines: 383	May – June 2014	871	Kongsberg 2040
5	D08	4947 – 5288  Total WCD lines: 341	April 2014	794	Kongsberg 2040
6	D09	5832 – 6241  Total WCD lines: 409	April – May 2014	876	Kongsberg 2040

### 10.3 Appendix 3 – WCI above shallow amplitude anomalies

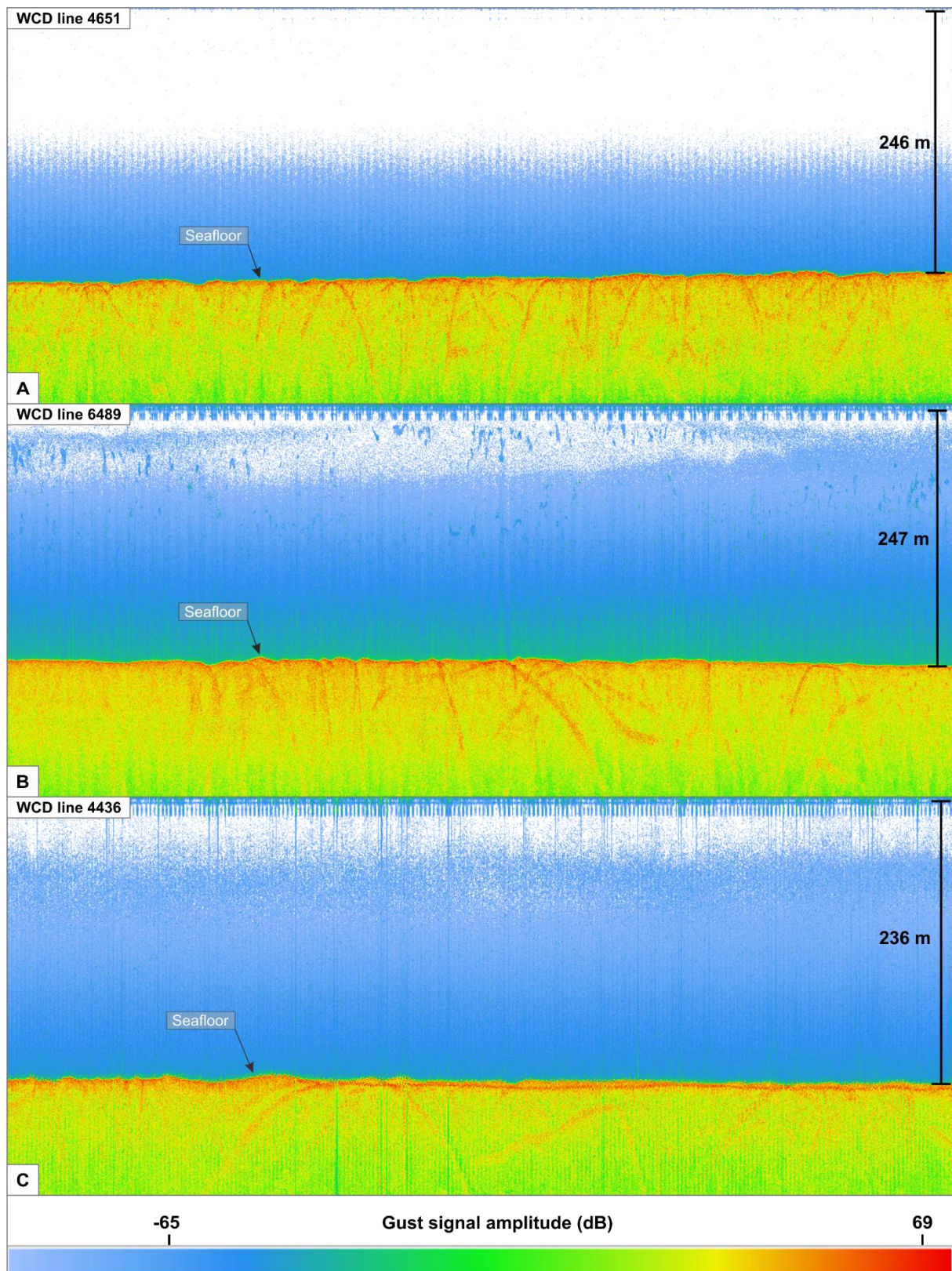


Figure 10.1: Water column data (WCD) shown in an R-stack view for (A), (B) and (C). Notice that no hydroacoustic signatures were observed. Data from Mareano (2014).



